PHYSICAL REVIEW D VOLUME 54, NUMBER 5 1 SEPTEMBER 1996

Proton and deuteron structure functions in muon scattering at 470 GeV

M. R. Adams,[6] S. Aïd,[10,a] P. L. Anthony,[9,b] D. A. Averill,[6] M. D. Baker,[11] B. R. Baller,[4] A. Banerjee,[15,c]
A. A. Bhatti,[16,d] U. Bratzler,[16] H. M. Braun,[17] T. J. Carroll,[12] H. L. Clark,[14,e] J. M. Conrad,[5,f] R. Davisson,[16] I. Derado,[12]
F. S. Dietrich,[9] W. Dougherty,[16] T. Dreyer,[1] V. Eckardt,[12] U. Ecker,[17,g] M. Erdmann,[1,h] G. Y. Fang,[5,i] J. Figiel,[8]
R. W. Finlay,[14] H. J. Gebauer,[12] D. F. Geesaman,[2] K. A. Griffioen,[15,j] R. S. Guo,[6,k] J. Haas,[1] C. Halliwell,[6]
D. Hantke,[12,l] K. H. Hicks,[14] H. E. Jackson,[2] D. E. Jaffe,[6,m] G. Jancso,[7] D.M. Jansen,[16,h] Z. Jin,[16] S. Kaufman,[2]
R. D. Kennedy,[3,n] E. R. Kinney,[2,o] H. G. E. Kobrak,[3] A. V. Kotwal,[5,f] S. Kunori,[10] J. J. Lord,[16] H. J. Lubatti,[16]
D. McLeod,[6] P. Madden,[3] S. Magill,[6,p] A. Manz,[12] H. Melanson,[4] D. G. Michael,[5,q] H. E. Montgomery,[4] J. G. Morfin,[4]
R. B. Nickerson,[5,r] J. Novak,[13,s] S. O'Day,[10,t] K. Olkiewicz,[8] L. Osborne,[11] R. Otten,[17] V. Papavassiliou,[2,u]
B. Pawlik,[8] F. M. Pipkin,[5,v] D. H. Potterveld,[2] E. J. Ramberg,[10,t] A. Röser,[17,w] J. J. Ryan,[11] C. W. Salgado,[4,x]
A. Salvarani,[3,y] H. Schellman,[13] M. Schmitt,[5,z] N. Schmitz,[12] G. Siegert,[1,aa] A. Skuja,[10] G. A. Snow,[10]
S. Söldner-Rembold,[12,bb] P. Spentzouris,[13,f] H. E. Stier,[1,v] P. Stopa,[8] R. A. Swanson,[3] H. Venkataramania,[13]
M. Wilhelm,[1,cc] Richard Wilson,[5] W. Wittek,[12] S. A. Wolbers,[4] A. Zghiche,[2] and T. Zhao[16]
(Fermilab E665 Collaboration)

[1] *Albert-Ludwigs-Universität Freiburg, D-79104, Freiburg, Germany*
[2] *Argonne National Laboratory, Argonne, Illinois 60439*
[3] *University of California, San Diego, California 92093*
[4] *Fermi National Accelerator Laboratory, Batavia, Illinois 60510*
[5] *Harvard University, Cambridge, Massachusetts 02138*
[6] *University of Illinois, Chicago, Illinois 60680*
[7] *KFKI Research Institute for Particle and Nuclear Physics of the Hungarian Academy of Sciences, H-1525 Budapest, Hungary*
[8] *Institute for Nuclear Physics, Krakow, Poland*
[9] *Lawrence Livermore National Laboratory, Livermore, California 94551*
[10] *University of Maryland, College Park, Maryland 20742*
[11] *Massachusetts Institute of Technology, Cambridge, Massachusetts 02139*
[12] *Max-Planck-Institut für Physik, Munich, Germany*
[13] *Northwestern University, Evanston, Illinois 60208*
[14] *Ohio University, Athens, Ohio 45701*
[15] *University of Pennsylvania, Philadelphia, Pennsylvania 19104*
[16] *University of Washington, Seattle, Washington 98195*
[17] *University of Wuppertal, Wuppertal, Germany*
(Received 9 February 1996)

The proton and deuteron structure functions F_2^p and F_2^d are measured in inelastic muon scattering with an average beam energy of 470 GeV. The data were taken at Fermilab experiment E665 during 1991 and 1992 using liquid hydrogen and deuterium targets. The F_2 measurements are reported in the range $0.0008<x<0.6$ and $0.2<Q^2<75$ GeV^2. These are the first precise measurements of F_2 in the low x and Q^2 range of the data. In the high x range of the data where they overlap in x and Q^2 with the measurements from NMC, the two measurements are in agreement. The E665 data also overlap in x with the DESY HERA data, and there is a smooth connection in Q^2 between the two data sets. At high Q^2 the E665 measurements are consistent with QCD-evolved leading twist structure function models. The data are qualitatively described by structure function models incorporating the hadronic nature of the photon at low Q^2. The Q^2 and the W dependence of the data measure the transition in the nature of the photon between a pointlike probe at high Q^2 and a hadronic object at low Q^2. [S0556-2821(96)05517-8]

PACS number(s): 13.60.Hb, 12.38.Qk, 12.40.Nn, 14.20.Dh

0556-2821/96/54(5)/3006(51)/$10.00

I. INTRODUCTION

In the single-photon-exchange approximation, the double differential cross section for charged lepton-nucleon scattering can be written as

$$\frac{d^2\sigma_{1\gamma}}{d(-Q^{-2})d(\ln x)} = 4\pi\alpha_{\rm em}^2 F_2(x,Q^2)\left[1-y-\frac{Mxy}{2E} + \frac{y^2(1+4M^2x^2/Q^2)}{2[1+R(x,Q^2)]}\right], \tag{1.1}$$

where E is the incoming lepton energy in the laboratory frame and $-Q^2$ is the square of the four-momentum transferred from the lepton. ν is the lepton energy loss in the laboratory frame, $x=Q^2/2M\nu$ is the Bjorken scaling variable, and $y=\nu/E$. $\alpha_{\rm em}$ is the electromagnetic coupling constant and M is the nucleon mass. $F_2(x,Q^2)$ is the structure function of the target nucleon and $R(x,Q^2)$ is the ratio of the longitudinal to the transverse virtual-photon cross sections.

Charged lepton scattering is an effective technique for probing the internal structure of nuclear matter, since the interaction of the probe is purely electroweak. In the 1950s, after some early experiments in Illinois, electron scattering experiments were performed at Stanford [1], followed later by experiments at Darmstadt, Daresbury, Orsay, Yale, DESY, and the CEA, to measure the charge distributions of various nuclei. At the energies available, the experiments were restricted to elastic scattering or excitation of the low-lying resonances. The measured elastic form factors fall rapidly with increasing four-momentum transferred, indicating that the charge distribution in nuclei is spatially extended and smoothly varying (i.e., there is no hard core in the nucleus). As higher energy electron beams became available at SLAC and DESY in the late 1960s, inelastic scattering experiments could be performed. These experiments [2] showed that, at large four-momentum transfers, the inelastic nucleon structure functions were (approximately) independent of any dimensioned quantity, a phenomenon known as scaling. Scaling had been predicted on the basis of current algebra [3], and the experimental result was interpreted as evidence for the existence of pointlike constituents in the nucleons [4]. These ‘‘partons’’ are now associated with quarks [5], which were first introduced to describe hadron spectroscopy [6,7].

Higher energy electron beams became difficult to produce as electrons, being light, are prone to losing energy through synchrotron radiation. Muons became a natural choice as high energy charged lepton probes. The 1970s and 1980s saw the development of the E26, CHIO, European Muon Collaboration (EMC), BCDMS, New Muon Collaboration (NMC), and E665 muon scattering experiments at Fermilab and CERN and the *ep* collider HERA at DESY [8–15]. These muon scattering experiments were augmented by a series of high energy neutrino scattering experiments [16–18] also at Fermilab and CERN. Neutrino interactions sample a different admixture of partons and thus complement muon scattering experiments. However, neutrino experiments have not yet measured structure functions below x of 0.01.

In the meantime, the quark-parton model developed into a dynamic gauge field theory of interactions called quantum chromodynamics (QCD). This theory has been quite effective in making perturbative calculations of the short distance behavior of quark interactions. In particular, QCD predicted a pattern of scaling violations of the inelastic structure functions at large four-momentum transfers, which has been confirmed by the high energy muon and electron experiments.

However, at low values of four-momentum transfers, the perturbative expansion of QCD breaks down. Real photoproduction measurements at high energy reveal the hadronic nature of the photon. This behavior is different from the pointlike photon-parton interactions manifest at large four-momentum transfers. The transition from the regime of per-

---

[a] Present address: University of Hamburg, D-22603 Hamburg, Germany.

[b] Present address: SLAC, Stanford, CA 94309.

[c] Present address: University of Michigan, Ann Arbor, MI 48109.

[d] Present address: The Rockefeller University, New York, NY 10021.

[e] Present address: Texas A&M University, College Station, TX 77843.

[f] Present address: Columbia University, New York, NY 10027.

[g] Present address: Jenfelderstr. 147, D-22045 Hamburg, Germany.

[h] Present address: Heidelberg University, D-69120, Heidelberg, Germany.

[i] Present address: Dept. of Medical Physics, University of Wisconsin, Madison, WI 53706.

[j] Present address: College of William and Mary, Williamsburg, VA 23187.

[k] Present address: Institute of Physics, Academia Sinica, Nankang, Taipei, Taiwan.

[l] Present address: GSF, Forschungszentrum fuer Umwelt und Gesundheit GmbH, D-85764 Oberschleissheim, Germany.

[m] Present address: SCRI, Florida State University, Tallahassee, FL 32606.

[n] Present address: Rutgers University, Piscataway, NJ 08855.

[o] Present address: University of Colorado, Boulder, CO 80309.

[p] Present address: Argonne National Laboratory, Argonne, IL 60439.

[q] Present address: California Institute of Technology, Pasadena, CA 91125.

[r] Present address: Oxford University, Oxford OX1 3RH, United Kingdom.

[s] Present address: Yale University, New Haven, CT 06511.

[t] Present address: Fermi National Accelerator Laboratory, Batavia, IL 60510.

[u] Present address: New Mexico State University, Las Cruces, NM 88003.

[v] Deceased.

[w] Present address: Klinikum Barmen, Abt. Radiologie, D-42283 Wuppertal, Germany.

[x] Present address: CEBAF, Newport News, VA 23606.

[y] Present address: AT&T Bell Labs, 2000 North Naperville Road, Naperville, IL 60540.

[z] Present address: Dept. of Physics, University of Wisconsin, Madison, WI 53706.

[aa] Present address: University of Wuppertal, D-42119 Wuppertal, Germany.

[bb] Present address: Albert-Ludwigs-Universität Freiburg, D-79104 Freiburg, Germany.

[cc] Present address: Hoffmann-LaRoche, CH-4002 Basel, Switzerland.

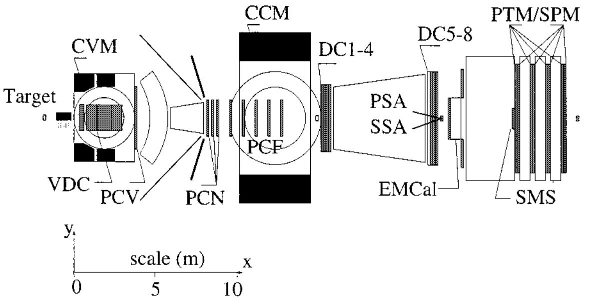

FIG. 1. The E665 forward spectrometer and muon detector.

turbative QCD to the domain of the hadronic photon should involve some change in the nature of photon-hadron interactions as a function of four-momentum transfer. The experiment E665 provides a wide range of energy and four-momentum transfer and thus an opportunity to understand the nature of this transition.

This paper presents the measurement of the proton and deuteron structure functions at E665, using the data taken during 1991–1992. In Sec. II, a brief description of the experimental apparatus will be given. In Sec. III, the structure function measurement technique will be described. In Secs. IV – VIII, detailed discussions will be provided of the analysis. The analysis issues are the estimation of the muon reconstruction and triggering efficiencies, the detector calibration and resolution, the radiative corrections, and the luminosity measurement. In Sec. IX, the results and the systematic uncertainties will be presented. The results will be compared with measurements from other experiments and with theoretical models in Sec. X.

II. E665 EXPERIMENTAL APPARATUS

A. Introduction

The Fermilab Experiment 665 (E665) was a fixed-target muon scattering experiment, with the highest energy (470 GeV) muon beam to date. The experiment was located in the New Muon Laboratory which is situated at the end of the NM beam line at Fermilab. The goal of the experiment was to measure structure functions and their ratios, and to study the hadronic final states produced in the muon interaction. Data were taken on hydrogen and deuterium, as well as heavy targets, to study the nuclear dependence of the above. The experiment took data in 1987–1988, 1990, and 1991–1992. The emphasis was on the identification and reconstruction of the incoming beam muon and the scattered muon in every event with high precision, and the measurement of the charged and neutral particles in the final state.

These considerations dictated the construction of the experiment. The apparatus consisted of a beam spectrometer, followed by an open-geometry forward spectrometer, followed by a muon detector. The apparatus has been described in detail in [13], and the upgrades to the detector made for the 1990 and 1991–92 runs are described in [19–21]. It is shown in Fig. 1. In the following we will provide a summary of the beam line and those parts of the detector relevant for the structure function measurement.

Throughout this paper, we use a right-handed coordinate system, where the x axis points along the nominal beam direction (north). The y axis points to the west and the z axis points upwards. The origin is defined as the center of the main momentum-analyzing magnet (CCM).

B. New muon beam line

The muon beam delivered to E665 was a tertiary beam, obtained from the decay of charged pions and kaons, which in turn were obtained from the interaction of primary protons of 800 GeV energy extracted from the Fermilab Tevatron synchrotron. The typical yield of muons per proton was 10^{-6}. The muon beam that was finally used was about 4 cm wide in the vertical direction and about 6 cm wide in the horizontal direction. The mean beam energy for the data collected during 1991–1992 was 470 GeV, with a spread of about 50 GeV.

The muon beam maintained the 53.1 MHz radio-frequency (rf) structure of the Tevatron accelerating rf field. The muons were localized in time to within 1 ns in the rf ''buckets,'' which occurred at 18.8 ns intervals. This time structure proved very useful in the construction of the electronic trigger signals, in that the rf could be used to provide time synchronization for all the electronic pulses. The final intensity of the muon beam was about 1 MHz, and 1–2 % of the buckets were occupied by a muon. A small fraction of the buckets contained multiple muons. The trigger hodoscopes and electronics provided almost single-bucket resolution. Events with multiple occupancy in a bucket could be identified both at the trigger level and using off-line reconstruction.

C. Beam spectrometer

The beam line was followed by the E665 beam spectrometer, which served a number of purposes. First, the hodoscopes in the beam spectrometer provided a fast electronic signal, indicating the passage of a beam muon. This was an essential component for all the beam-related triggers. The transverse segmentation of the beam hodoscopes (SBT's) enabled us to define the accepted beam phase space at the trigger level and to detect multiple occupancy in the bucket. The beam trigger signal produced by the hodoscopes was counted by scalers to provide a total beam count. The hodoscope hits were latched and this information was used to identify in-time and out-of-time beam tracks off line.

Second, the beam spectrometer contained 24 planes of multiwire proportional chambers with 1 mm wire spacing (which we refer to as PBT's) and a dipole magnet (which we call NMRE). These were used to provide precise reconstruction and momentum measurement of the beam muon. The spectrometer consisted of two arms with the NMRE magnet in the middle. The NMRE magnet provided a transverse momentum kick of (1.515 ± 0.004) GeV. The length of the beam spectrometer helped to provide a resolution on the curvature of $\delta(p^{-1})\sim 8\times10^{-6}$ GeV^{-1}, corresponding to a 2 GeV momentum uncertainty for a 500 GeV muon.

D. Target assembly

The target assembly was placed in the path of those beam muons which could be tagged and reconstructed by the beam spectrometer. All the targets and an empty liquid target vessel were mounted on a precision table that moves the targets laterally. The different targets were moved into the beam every 1–4 min in a specified cycle. The empty target data were used to subtract out the off-target scatters on a statistical basis.

The targets were placed in the nominally field-free region in front of the vertex magnet [called the CERN Vertex Magnet (CVM)]. By having the muon scattering vertex in the field-free region, the correlations between the errors on reconstructed kinematics were greatly reduced, simplifying the analysis of the data. The three target vessels were identical and two contain liquid hydrogen (H_2) and deuterium (D_2) respectively. The target positions and pressures were monitored during the course of data taking. The length of the active target material was nominally 1 m for the liquid targets. This is discussed in more detail in Sec. VIII B.

E. Muon spectrometer

1. Tracking detectors

The purpose of the forward spectrometer was to provide the trigger for muon scattering events and to record the information necessary to reconstruct the scattered muon and the other final state particles. Charged particle measurements were provided by proportional and drift chambers which formed part of a double-dipole, open-geometry spectrometer. Photon detection and energy measurement were provided by an electromagnetic calorimeter, which also served to identify electrons in conjunction with the spectrometer. Downstream of the spectrometer and a 3 m thick iron absorber which stopped all particles but muons, there was a muon detector. The muon detector provided information for on-line muon triggering and off-line muon reconstruction.

The relevant parts of the muon spectrometer for this structure function analysis were the tracking and muon detectors. A plan view of the muon spectrometer is shown in Fig. 1, in which various detector elements are labeled. Immediately downstream of the target assembly was placed a set of vertex drift chambers (VDC's) inside the CERN Vertex Magnet (CVM). The VDC consisted of 72 planes of chambers with 200 μm resolution. At the downstream end of the CVM, a set of six multiwire proportional chambers called PCV (2 mm wire spacing) were installed. The PCV-VDC combination formed an anchor for track finding and served to increase the length of the lever arm upstream of the Chicago Cyclotron Magnet (CCM), thus providing good resolution. The VDC contain Y,Z,U, and V views. The PCV contained two Y, two U, and two V planes, with stereo angles $\pm 18°$ and $\pm 45°$.

The muon track-finding process hinged on the multiwire proportional chambers and drift chambers placed on either side of and inside the aperture of the CCM. Twelve multiwire proportional chambers (PC's) were placed upstream of the CCM. An additional 15 multiwire proportional chambers (called PCF) were arranged in five groups (stations) of three chambers each inside the CCM. The wire spacing in these chambers was 3 mm and 2 mm, respectively. The PC chambers contained three planes in each of four views Y,Z,U and V with $\pm 28°$ stereo angles. Each PCF station contained one Z, one U, and one V plane with $\pm 15°$ stereo angles. Downstream of the CCM were two stations of drift chambers, labeled DCA (DC1-4) and DCB (DC5-8) for the upstream and downstream sets respectively. These drift chambers are collectively referred to as the DC. Each DC station contained two pairs of Z chambers and a pair each of U and V chambers. The wire spacing was 5 cm, and the chambers in a pair were staggered by half a wire spacing to resolve left-right ambiguities. The stereo angles were $\pm 5°$. The spatial resolution was about 300 μm. Since drift chambers cannot operate at high rate, they were deadened by construction in the region where the beam passed. In this region a small multiwire proportional chamber called a PSA was placed, near the DCB. The PSA contained eight planes with 1 mm wire spacing, two in each of the Y,Z,U, and V views. The stereo angles are $\pm 45°$.

Tracks that spanned the length of the forward spectrometer were able to achieve a curvature resolution of $\delta(p^{-1}) \sim 2\times 10^{-5}$ GeV^{-1}. The resolution on x_{Bj} was about 5% at low x_{Bj}, and the resolution on Q^2 was about 4%. The CVM field strength was 1.5131 T with a transverse momentum kick of 1.293 GeV. The CCM provided a transverse momentum kick of 2.019 GeV. The polarities of the two magnets were reversed with respect to each other. The two magnets were positioned such that the position of the scattered muon at a ‘‘focusing’’ plane was independent of momentum and depended only on the scattering angle. The muon detector was placed at the focusing plane, thereby allowing the construction of muon triggers that can select on scattering angle.

2. Muon identification detectors

The muon detectors were arranged in four sets or stations behind a 3 m hadron absorber made of iron ($\sim$ 18 interaction lengths and $\sim$ 170 radiation lengths). The four stations were separated by 1 m thick concrete absorbers that stopped shower particles from propagating from one station to another. Each station contained proportional tube planes (called PTM's) and large and small hodoscopes (called SPM's and SMS's respectively). The PTM's and SMS's were arranged in Y and Z views, the PTM's covering the wide angles and the SMS's covering the central dead regions in the PTM's where the rates were high. The SPM's provided wide-angle hodoscope coverage. All three detectors provided information for various muon triggers. Additional wide-aperture hodoscopes (called SUM) were installed between the DCB drift chambers and the electromagnetic calorimeter. They were used in conjunction with the SPM hodoscopes to improve the speed of the large-angle muon trigger signals. The PTM and SMS information is also used for off-line muon tagging. The PTM and SMS detector elements had 1.27 cm and 1.32 cm widths, respectively. The SMS hodoscopes were covered in front by a lead sheet 12–13 mm thick, which served to absorb soft shower particles and reduce the SMS hit multiplicity.

A hodoscope called SSA was installed upstream of the hadron absorber and immediately downstream of the DCB drift chambers. It was a small hodoscope with good position resolution placed in the beam, to provide a veto signal for the small-angle trigger (SAT). The SVS was also another small hodoscope, placed in the beam region inside a hole bored into the iron absorber at the downstream end. It provided a fast beam veto signal that was used to construct the ‘‘SVS’’ large angle trigger. It was placed as close to the iron as possible so that shower particles accompanying the muon are localized when they hit the hodoscope.

3. Electromagnetic calorimeter

The calorimeter was placed immediately upstream of the hadron absorber. It was a lead-gas sampling calorimeter, [22–24] consisting of 20 planes of ~5 mm thick lead sheets (one radiation length each) separated by Iarocci proportional tube planes. The wire spacing was 1 cm. Copper pads were placed on both sides of the Iarocci planes, which picked up signals through capacitive coupling. Pads in the successive planes were placed to overlap each other to form ''towers,'' and the signals from all pads in a tower were summed before readout. The pad size used was 4 cm × 4 cm in the inner 1 m × 1 m region, 8 cm × 8 cm in the central 2 m × 2 m region outside the inner region, and 16 cm × 16 cm in the outer region.

The electromagnetic calorimeter was very useful in identifying muon-electron elastic scatters and hard muon bremsstrahlung, as the topology of electromagnetic energy flow in these events is quite distinct from that in ordinary inelastic scatters. During the investigation of various systematic effects, the calorimeter was used to tag such electromagnetic events. These investigations will be discussed later.

F. Triggers

E665 operated with a number of triggers. These can be classified into three categories.

(1) Physics triggers looked for events in which the muon interacts.

(2) Normalization triggers. These are also called random beam triggers. Every physics trigger included in its definition the requirement that a valid beam muon signal exist. The beam signal by itself was also randomly sampled to create a random beam trigger. The count of these triggers is used to obtain the count of the total number of beams available to the physics trigger and, hence, the luminosity. Some physics triggers used the same beam definition while others were different; a separate random beam trigger was created for each beam definition.

(3) Monitoring triggers provided data to study the detector performance.

The physics triggers can be classified into three subcategories.

(a) Small-angle trigger (SAT). This trigger only used veto hodoscopes to indicate the absence of an unscattered muon. This trigger is discussed in more detail below. The structure function measurement is performed with the SAT data, because the SAT was able to trigger on smaller-angle scatters than was possible with the large-angle triggers.

(b) Large-angle triggers (LAT). These triggers used the wide-angle muon detectors and the SUM hodoscope to indicate a scattered muon, in conjunction with the absence of a signal in a fixed veto hodoscope placed at small angle. The idea was to ensure that there was no signal in the beam region that was consistent with an unscattered muon and at the same time see a signal at large angles that was consistent with a scattered muon. The three large-angle triggers were called the SVS, SVSWAM2, and CVT. They used different combinations of veto elements and wide-angle detectors. A description of the LAT's is provided in [19]. The data from the LAT's are not used directly in the structure function measurement, but they are used to study an aspect of the small-angle trigger efficiency.

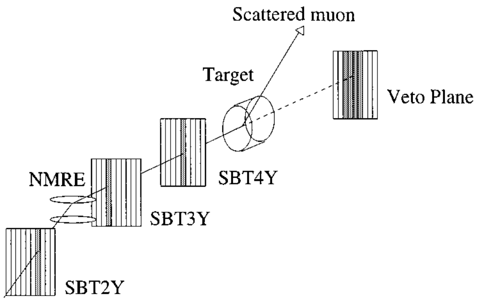

FIG. 2. Schematic diagram of the SAT.

(c) Calorimeter trigger (CAL) used signals from the electromagnetic calorimeter to select muon interaction events. It did not incorporate a muon veto detector behind the hadron absorber. In fact, the trigger included no veto at all and no information from any muon detector behind the absorber. Because of this feature, the calorimeter trigger provided the data to measure the rate of self-vetoes induced in all the muon triggers by the muon showering in the absorber.

Each category used a different beam definition for reasons specific to each type of trigger. Three random beam triggers (called RLAT, RSAT, and RCAL, respectively) were constructed in association with the corresponding sets of physics triggers.

The SAT is described in [21]. A schematic of the SAT construction is shown in Fig. 2. The SAT was a pure veto trigger that sensed the absence of the unscattered muon in coincidence with an incoming beam muon. The beam muon was defined by the appropriate coincidence (i.e., roads) of hits in the beam hodoscopes. These signals were provided to a fast preprogrammed memory module which predicted the position of the unscattered muon at the muon detectors downstream of the forward spectrometer. At this position additional hodoscopes were located. If these hodoscopes signaled hits in the predicted muon position, then no scatter was expected and the event was vetoed. On the other hand, the beam signal and the absence of the corresponding unscattered muon signal indicated a scatter and the trigger fired.

The special feature of this construction was that the veto window for any detected beam muon moved according to the position and slope of the incoming muon. This allowed the veto window to be smaller than the beam profile, permitting the detection of interactions where the scattered muon remained within the beam phase space. This means that the trigger could fire on small-angle scatters (down to ~ 1 mrad.).

The first two stations of the SMS hodoscopes placed downstream of the hadron absorber were used to produce the veto signal. It was recognized that this arrangement produces a large number of fake triggers due to scatters in the absorber.

To alleviate this problem, a small hodoscope (called SSA) was placed upstream of the absorber and its signal was incorporated into the veto. The muon position at this hodoscope was of course not affected by any subsequent scatter.

While this solved the problem of fake triggers due to absorber scatters, it made the trigger sensitive to vetoes caused by other particles produced in an inelastic muon interaction.

A monitoring trigger called the SATPS was constructed to be the same as the SAT except that the SSA veto was not included. This allowed the SSA veto to be studied. This trigger was prescaled by a factor of 32 due to the large fake trigger rate.

Individual scintillation counters in the SSA hodoscope were 1.10 cm wide. The SSA hodoscope was placed 25 m downstream of the target, while the two SMS hodoscopes used in the SAT were placed 30.7 m and 32.3 m downstream of the target, respectively.

G. Spill local rate monitor

The spill local rate monitor recorded the beam muon occupancy of a number of contiguous buckets in the vicinity of the trigger time. This record was read out with every event. The beam muon signal was constructed by taking the sevenfold coincidence of the SBT hodoscope signals from the beam spectrometer. The local rate monitor had a large circulating memory into which it wrote the presence or absence of the muon signal at the rf edge. Following the occurrence of a trigger, the local rate monitor continued to record for a preset number of buckets and stopped. The data acquisition system read out a preset number of words from the memory stack. Consequently, the occupancy of every bucket starting about 2.4 μs before the trigger and ending about 50 μs after the trigger was recorded.

III. STRUCTURE FUNCTION ANALYSIS

The structure function F_2 is related to the single-photon-exchange cross section as shown in Eq. (1.1). The relation between the single-photon-exchange cross section and the total (radiative) muon cross section is given in Eq. (3.2). The number of muon scattering events observed in a bin of measured kinematics, in the absence of background, is related to the total muon cross section σ_{tot} in the following manner:

$$N_{\text{obs}}^{\text{data}} = \int_{\vec{\xi}'_1}^{\vec{\xi}'_2} d\vec{\xi}' \int d\vec{\xi}\,\mathcal{L}(\vec{\xi})\mathcal{A}(\vec{\xi}',\vec{\xi})\sigma_{\text{tot}}(\vec{\xi}), \qquad (3.1)$$

where $\mathcal{A}$ is the kernel describing the acceptance and resolution of the detector and $\mathcal{L}$ is the luminosity. $\vec{\xi}$ is the vector of true kinematic variables and $\vec{\xi}'$ is the vector of observed variables. The relation between the single-photon-exchange cross section and the total (radiative) muon cross section is

$$\sigma_{\text{tot}}(\vec{\xi}'') = \int d\vec{\xi}\,\mathcal{R}(\vec{\xi}'',\vec{\xi})\sigma_{1\gamma}(\vec{\xi}), \qquad (3.2)$$

where $\mathcal{R}$ is the kernel of radiative corrections. Therefore, the fully expanded relation between the number of observed events in a bin and the single-photon-exchange cross section is

$$N_{\text{obs}}^{\text{data}} = \int_{\vec{\xi}'_1}^{\vec{\xi}'_2} d\vec{\xi}' \int d\vec{\xi}\,\mathcal{L}(\vec{\xi})\mathcal{K}(\vec{\xi}',\vec{\xi})\sigma_{1\gamma}(\vec{\xi}). \qquad (3.3)$$

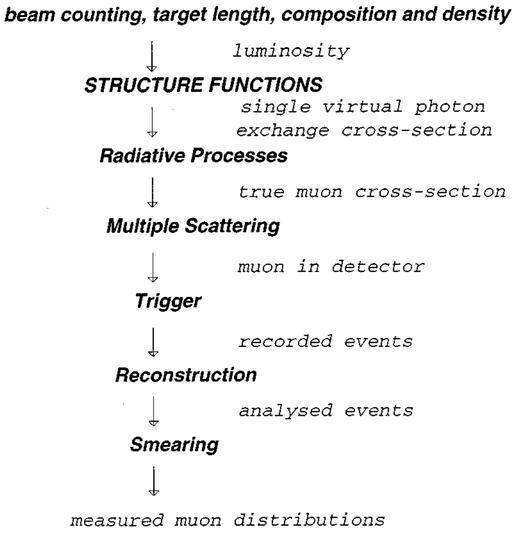

FIG. 3. A flow chart indicating the connection between the structure functions and the measured muon distributions.

$\vec{\xi}$ are the variables describing the kinematics of the muon-nucleon interaction. In the measurement of inclusive muon scattering, the events are binned in the kinematics which are determined from the measured four-momenta of the incoming and the scattered muon, denoted by $\vec{\xi}'$. $\vec{\xi}'_1$ and $\vec{\xi}'_2$ denote, respectively, the lower and upper edges of the bin. The integrand contains the single-photon-exchange cross section $\sigma_{1\gamma}$, the luminosity $\mathcal{L}$, and the overall response kernel $\mathcal{K}$. The complete set of variables includes the following.

(1) The five parameters associated with the beam whose distribution is described by $\mathcal{L}$. These are the transverse positions, the direction of motion (slopes), and the energy. We integrate over the beam distribution when the observed events are binned in the scattering kinematics.

(2) The longitudinal position of the scattering point. Since the muon beam suffers negligible attenuation in the target, the true distribution of this variable is uniform in the target. We integrate over the longitudinal position of the scatter.

(3) The variables describing the muon scatter, which we have chosen as x and Q^2, and the azimuthal angle ϕ of the scatter. The ϕ distribution is expected to be uniform for an unpolarized target; hence, we integrate over it. The observed events are binned in two-dimensional x and Q^2 bins.

(4) All the variables needed to describe the final state produced in the muon-nucleon scatter (excluding the scattered muon). In this inclusive measurement, we integrate over all the final states.

The process by which a hypothetical ‘‘single-photon-exchange’’ event appears as a scattered muon in the detector is indicated by the flow chart in Fig. 3.

The response kernel $\mathcal{K}(\vec{\xi}',\vec{\xi})$ gives the probability distribution of a single photon event with kinematics $\vec{\xi}$ appearing in the detector with kinematics $\vec{\xi}'$. It contains contributions from processes that change the probability of the muon scatter to occur or be detected and processes that cause the measured muon vertex kinematics to be different from those of the exchanged virtual photon. These processes can be enumerated as follows.

(1) Radiative corrections to the single-photon-exchange Born diagram. These processes change both the cross section and the kinematics.

(2) Multiple scattering and energy loss of the muons in the detector, before and after the hard scatter of interest. These processes change the apparent kinematics of the event.

(3) Efficiency of triggering on a scattered muon event. Triggering inefficiency reduces the measured rate and results in a reduction in the observed cross section.

(4) Efficiency of reconstructing the scattered muon trajectory. The efficiency of reconstructing incoming beam muons is subsumed into the measurement of the usable luminosity. Reconstruction inefficiency for the scattered muon reduces the measured rate because the kinematics of the event cannot be determined unless both the incoming and outgoing muons have been measured.

(5) Smearing in the muon kinematics due to the finite spatial resolution of the tracking chambers.

(6) Systematic errors in the measured muon kinematics due to miscalibration of the detector.

When all these processes are understood, the response kernel $\mathcal{K}$ can be constructed. As discussed in the following sections, these processes are studied and incorporated into a Monte Carlo model of muon scattering and the detector. The simulated and reconstructed events are then subjected to the same exercise of counting muon scatters in a bin of reconstructed kinematics. Thus, we count $N_{\text{obs}}^{\text{MC}}$ (where MC denotes Monte Carlo data) analogous to Eq. (3.3). We also count the number of generated events in a bin; thus,

$$N_{\text{gen}}^{\text{MC}}=\int_{\vec{\xi}_1'}^{\vec{\xi}_2'} d\vec{\xi}' \int d\vec{\xi}\,\mathcal{L}(\vec{\xi})\sigma_{\text{tot}}(\vec{\xi}). \tag{3.4}$$

The ratio $\epsilon = N_{\text{obs}}^{\text{MC}}/N_{\text{gen}}^{\text{MC}}$ is computed in each bin. The product

$$N_{\text{obs}}^{\text{data}}\frac{N_{\text{gen}}^{\text{MC}}}{N_{\text{obs}}^{\text{MC}}}=\frac{N_{\text{obs}}^{\text{data}}}{\epsilon} \tag{3.5}$$

would be the estimate for $N_{\text{true}}^{\text{data}}$, the true number of data events occurring in the bin. In order to extract the total cross section σ_{tot} in the bin, we must also correct for the bin width and the luminosity. The bin width Δ, the integrated luminosity L, and an overall correction factor for the data, ω_σ, are computed as

$$\Delta=\int_{\vec{\xi}_1'}^{\vec{\xi}_2'} d\vec{\xi}',$$

$$L=\int d\vec{\xi}\,\mathcal{L}(\vec{\xi}),$$

$$\omega_\sigma=\epsilon\times L\times\Delta \tag{3.6}$$

$N_{\text{obs}}^{\text{data}}$ can be corrected in each bin by weighting each data event by $1/\omega_\sigma$. This gives us the total muon cross section $\sigma_{\text{tot}}(\vec{\xi})$ in the bin; thus,

$$\sigma_{\text{tot}}=\sum_{i=1}^{N}\frac{1}{\omega_\sigma}, \tag{3.7}$$

where $N=N_{\text{obs}}^{\text{data}}$

To extract the structure function F_2, we must correct σ_{tot} for radiative effects and then extract F_2 from the resulting $\sigma_{1\gamma}$ using Eq. (1.1). The radiative kernel $\mathcal{R}$ can be collapsed into a radiative correction factor K, by using Eq. (3.2) making the definition

$$\sigma_{\text{tot}}(\vec{\xi}'')=\int d\vec{\xi}\,\mathcal{R}(\vec{\xi}'',\vec{\xi})\sigma_{1\gamma}(\vec{\xi})\equiv K(\vec{\xi}'')\sigma_{1\gamma}(\vec{\xi}''). \tag{3.8}$$

The calculation of K is done by the computer program FERRAD35 [30], which was kindly provided to us by the NMC. Also, a kinematic factor λ is defined as

$$\lambda=4\pi\alpha_{\text{em}}^2\left[1-y-\frac{Mxy}{2E}+\frac{y^2(1+4M^2x^2/Q^2)}{2[1+R(x,Q^2)]}\right]. \tag{3.9}$$

Defining

$$\omega_{F2}=\omega_\sigma\times K\times\lambda, \tag{3.10}$$

where ω_σ is defined in Eq. (3.6), F_2 is extracted by weighing each data event by $1/\omega_{F2}$ as follows:

$$F_2=\sum_{i=1}^{N}\frac{1}{\omega_{F2}}. \tag{3.11}$$

So far we have neglected the possibility that there are background events occurring in the data which should not be included in the measurement. Muon scatters originating from material outside the target constitute such background. Therefore,

$$N_{\text{obs}}^{\text{data}}=N_{\text{target}}+N_{\text{out of target}}. \tag{3.12}$$

Consequently, F_2 extracted by Eq. (3.11) actually contains two contributions:

$$F_2^{\text{full target}}=\sum_{i=1}^{N_{\text{target}}}\frac{1}{\omega_{F2}}+\sum_{i=1}^{N_{\text{out of target}}}\frac{1}{\omega_{F2}}. \tag{3.13}$$

We are interested only in the first component produced by the in-target scatters. The second component is measured by taking data on an identical target vessel which is empty. The structure function measured from the empty target is

$$F_2^{\text{empty target}}=\sum_{i=1}^{N_{\text{out of target}}}\frac{1}{\omega_{F2}}. \tag{3.14}$$

The number of beam muons to which the empty target is exposed is used to normalize the empty target measurement. Since all the running conditions are the same for the full target and the empty target data, the contribution to $F_2^{\text{full target}}$ coming from the out-of-target scatters is statistically equal to $F_2^{\text{empty target}}$. This allows us to statistically subtract the background as follows:

$$F_2^{\text{target}}=F_2^{\text{full target}}-F_2^{\text{empty target}}. \tag{3.15}$$

A. E665 Monte Carlo simulation

We note from the discussion in the previous section that the corrections applied to the data involve integrations over kernels and underlying distributions. In order to make the corrections properly, we must have the right simulation of the three components of the integrand in Eq. (3.3). These are the beam phase space distributions $\mathcal{L}$, the cross section and the final state distributions $\sigma_{1\gamma}$, and the detector simulation which contains the kernel $\mathcal{K}$. These three components are incorporated in a Monte Carlo model of the experiment.

Reconstructed random beam triggers are used to produce files containing the five parameters (the momentum, the transverse Y and Z positions, and Y and Z slopes, at a fixed longitudinal X position) needed to specify beam tracks. Each file typically contains a list of parameters describing approximately 10 000 beam tracks. Separate files are created for different periods of the run in order to track any changes in the phase space occupied by the beam [26]. Therefore the beam phase space is introduced in the Monte Carlo calculation on an event-by-event basis as it is in the data, not by a simulation.

The event generation begins with the generation of a beam track whose parameters have been read in from a beam file. The beam is tracked from the beam spectrometer into the target by the GEANT 3.15 program [27]. The longitudinal position of the scattering vertex is picked within the target according to a flat distribution. The azimuthal angle of the scatter is also picked according to a flat distribution. The kinematics of the scatter are generated following the total cross section. The inelastic structure functions are constructed from various parametrizations of data and a model due to Donnachie and Landshoff [28]. Parametrizations of the proton elastic form factors due to Gari and Kruempelmann [29] are used for the calculation of the radiative corrections. For calculating the radiative corrections for deuterium, the nuclear form factor due to Locher and Svarc [30] (using 1990 fit solution 1, including meson exchanges), and the quasielastic suppression factor due to Bernabeu [31] is used. The electromagnetic radiative effects are simulated in the Monte Carlo using the GAMRAD program, [32] which is based on the calculation of Mo and Tsai [33,34].

The LUND programs LEPTO 5.2 and JETSET 6.3 [35] are used to generate all the particles in the hadronic final state. The GRV HO [36] set of parton distributions are used to calculate the relative cross sections for the quark, quark-antiquark, and quark-gluon events, because they are specified down to Q^2 of 0.3 GeV^2. The parton distributions are not used for the calculation of the total muon-nucleon cross section. The GAMRAD program generates photons that are radiated by the muon.

The scattered muon, radiative photons, and all the hadronic final state particles are tracked through the detector by the GEANT program. The detector simulation specifies all the materials present and their locations. This information is used by GEANT to calculate the multiple scattering, energy loss, and reinteractions of all the primary particles as well as any generated secondaries and decay products. The following physics processes are simulated by GEANT in the E665 Monte Carlo model: Deflection of charged particle trajectories in a magnetic field; multiple scattering using the Gaussian approximation; particle decay; energy loss as particles traverse material; Compton scattering; e^+e^- pair production; bremsstrahlung; δ-ray production; e^+e^- annihilation; hadronic interactions (simulated using the GHEISHA program [35]).

GEANT tracks each particle (photons, electrons, muons, and charged and neutral hadrons) until the energy of the particle falls below 500 MeV, for particles upstream of the electromagnetic calorimeter. Muons are tracked through the calorimeter and hadron absorber using the Gaussian approximation for multiple scattering (instead of GEANT in order to reduce computing time). In addition, the catastrophic interactions of the scattered muon in the calorimeter and the hadron absorber are simulated by using special parametrizations derived from our data (described in Sec. V A 4).

The second stage Monte Carlo simulation MC2 [37] simulates hits made by charged particles in the hodoscopes and the proportional and drift chambers. The measured resolutions of the chambers are used to smear the hits. The drift chamber simulation includes the inefficiencies induced by the presence of multiple hits. The position and time dependence of the chamber efficiencies are measured from the data and incorporated into the MC2 program.

B. Input structure functions

For the Monte Carlo generation and the initial calculation of the radiative corrections, we use a parametrization of the structure function obtained from existing data. We use published parametrizations of SLAC and DESY electroproduction data and Daresbury photoproduction data, as well as NMC and BCDMS muoproduction data [38–40]. In the kinematic domain of high W and low Q^2, the structure functions have not been previously measured. In this regime we use the model of Donnachie and Landshoff [28], which the authors have constrained to match the photoproduction data and the NMC data.

The BCDMS and NMC analyses of F_2 were performed using the radiative corrections formulated by Akhundov, Bardin, and Shumeiko [11,12]. The SLAC analyses were performed using the radiative corrections formulated by Mo-Tsai [33]. The analysis presented here uses the Mo-Tsai formulation, including τ and quark loops in the vacuum polarization diagrams, and the electroweak γ-Z interference effects. The results obtained using these schemes have been compared [41,42] and they are in agreement over most of the kinematic range. The maximum difference between the calculations, which occurs at low x and high y, is less than 2% of F_2.

The single-photon-exchange cross section is weakly dependent on R. BCDMS used the theoretical form of R motivated by QCD, which is probably valid in the Q^2 range of the BCDMS measurement ($Q^2 > 10$ GeV^2). The E665 and NMC analyses both use the parametrization of R obtained from a global analysis of SLAC data [43]. This parametrization includes QCD-motivated terms as well as terms motivated by higher twist effects, since the SLAC, E665, and NMC data extend to low values of Q^2 ($Q^2 > 0.3$ GeV^2). Prior SLAC measurements of F_2 have often used fixed values of R, such as $R = 0.18$. This value is consistent with the value of the SLAC parametrization (henceforth referred to as R_{SLAC}) at the typical value of Q^2 for the SLAC data. Finally, since $R=0$ for $Q^2=0$, the real photoproduction cross section can be related simply to F_2 as follows:

$$\lim_{Q^2\to 0}\frac{F_2}{Q^2}=\frac{\sigma_{\gamma N}(\nu)}{4\pi^2\alpha_{\rm em}}. \tag{3.16}$$

Thus, there has been a fairly self-consistent treatment of leptoproduction and photoproduction cross sections to extract F_2. These F_2 parametrizations can therefore be used as initial input for the calculation of corrections in this analysis.

IV. MUON RECONSTRUCTION EFFICIENCY

A. Detector and algorithm

One of the important corrections that one needs to make in the extraction of structure functions is the loss of muons due to reconstruction inefficiency. Briefly, to discover whether a muon-nucleon scatter occurred, we have to reconstruct the trajectories of the beam muon and of the scattered muon to enable the event kinematics to be calculated. Some of the scattered muon events cannot be used in the measurement because the muon tracks have not been properly identified. We have to understand this loss and correct for it.

The event reconstruction begins with the identification of hit lists that are produced by the beam tracks, the muon spectrometer tracks, and the muon identification detector segments. This step is called pattern recognition.

Each hit list in the beam and forward spectrometers is then fitted with a quintic spline model of the track trajectory, taking into account multiple Coulomb scattering. Knowledge of the magnetic fields is then used to find the track parameters. This step is called track fitting.

The next step, muon match, attempts to use the segments behind the absorber to identify one or more spectrometer tracks as muons.

The final step is the vertex-finding program. It identifies one of the spectrometer muon tracks as the scattered muon and attempts to find the intersection point of the beam and the scattered muon tracks. This vertex is used as the primary interaction vertex. Other tracks are then attached to the primary vertex if they are consistent with the hypothesis that they originate from the primary vertex. The vertex position is refitted iteratively with all such tracks contributing to the fit.[1] Finally, the beam and scattered muon track parameters at the vertex are used to calculate the event kinematics.

Understanding the performance of the pattern recognition program is very important in the determination of the overall reconstruction efficiency. If the pattern of chamber and hodoscope hits produced by a track cannot be seen, then one can go no further in the process of track reconstruction. The pattern recognition algorithm tries to find tracks in a number of different ways. Each method uses a set of software codes called processors. In the first method, it looks for straight line segments in the PC chambers upstream of the CCM and the DC chambers downstream of the CCM. The upstream (PC) and downstream (DC) segments are associated with each other using PCF hits inside the CCM magnet to constrain the match.

In the second method, tracks are recognized using only the upstream PC and PCF chambers inside the CCM. These tracks are then projected downstream into the DC or the small-aperture PSA chamber to pick up hits. In fact this is the only method that is used to pick up the PSA contribution to the track. The PC-PCF tracks needed for this can be found in two ways: PC segments can be projected forward into the PCF's, and PCF segments can be projected backwards into the PC's. Both ways are attempted and the ambiguities are resolved at a later stage in the pattern recognition algorithm.

Even if no downstream contribution is obtained from the DC or PSA, the PC-PCF track is declared ''valid'' since the curvature can be measured with the PCF's alone. The momentum resolution on such tracks is rather poor. Therefore, in this analysis, a downstream contribution is required in order to ensure good resolution: The loss in efficiency due to this requirement is studied using the PC-PCF tracks.

Later, the tracks are projected back from the PC into the PCV to pick up PCV hits. This increases the length of the upstream lever arm of the track and improves the resolution significantly.

Finally, the forward spectrometer tracks are linked to the vertex spectrometer tracks found by the VDC's. First, the forward spectrometer tracks are projected back into the VDC's to pick up hits directly. Then, the VDC algorithm reconstructs tracks independently using the remaining hits. These tracks are extrapolated into the forward spectrometer again to attach any remaining hits.

This technique of pattern recognition builds in certain redundancies. This enables us to perform many cross-checks on detector efficiencies and finely tune the Monte Carlo simulation to the data.

B. Pattern recognition efficiency

Efficiency loss at the stage of pattern recognition can result from two effects: chamber inefficiencies or inefficiencies of the pattern recognition algorithm. The general approach is to simulate chamber efficiencies in a Monte Carlo program, the output of which is in the same format as real data. The Monte Carlo simulation output is reconstructed in the same way as data. Then, after verification of the simulation in many different ways, the Monte Carlo simulation can be used to calculate the pattern recognition efficiency as a function of true muon kinematics.

1. Uncorrelated chamber efficiencies

We will first discuss the measurement of individual chamber efficiencies and then address the issue of correlated chamber inefficiencies. We can enumerate the following issues concerning the simulation of efficiencies of individual chambers: geometrical aperture; regions deadened by construction, due to spacers, support wires or due to high-flux regions; dead regions due to bad electronics; dead regions due to radiation damage; time dependence of overall efficiency due to high voltage or gas composition variations, radiation damage and electronics variations.

A fairly elaborate chamber simulation program has been developed that allows all of these effects to be modeled. In

---

[1] However, the fitted vertex position is not used to constrain the tracks. This avoids correlated biases in the final parameters reported for different tracks.

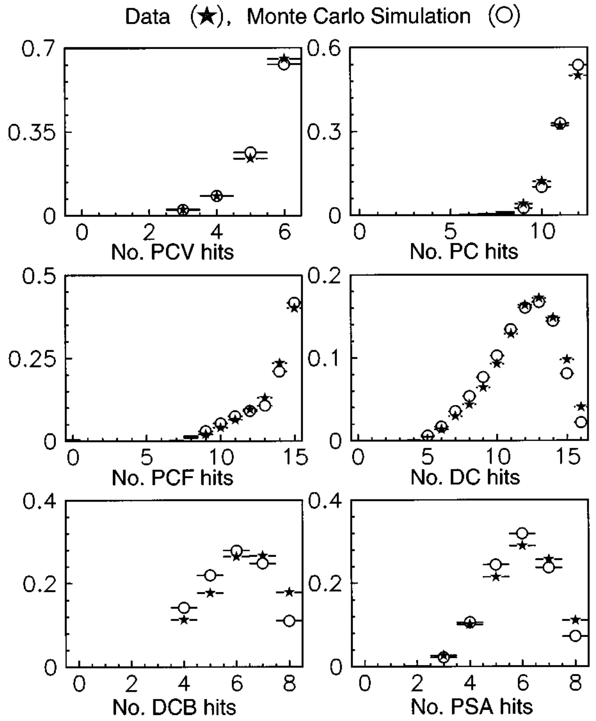

FIG. 4. Probability distribution of the number of detector hits on a track, for the data and the Monte Carlo simulation. The sample consists of scattered muons and hadrons in inelastic scatters.

order to test the chamber models, many detailed comparisons between the data and the Monte Carlo simulation are made. The entire data run is split into nine run periods, and each run period is sampled uniformly to produce a data set that can be used to study the chambers.

2. Correlated chamber inefficiencies

Per-event correlations in chamber efficiencies can arise due to dead time in the readout electronics at high rates, readout errors, hit loss due to overlapping tracks, and effects of the tracking algorithm.

A quantity sensitive to correlated effects is the number of hits from a given detector group that contribute to a track. This tests for correlations within a detector group. Figure 4 shows the comparison between the data and the Monte Carlo simulation of the probability distribution of the number of hits from each chamber group. We find that there is good agreement for all detectors except the drift chambers, where the Monte Carlo simulation shows slightly fewer drift chamber hits than the data.

Another quantity sensitive to correlations is the probability that a detector group as a whole contributes to a track. The detector groups mentioned earlier are PCV, PC, PCF1-5, DCA, DCB, and PSA. The PC chambers are required for forward spectrometer tracks; however, none of the others are absolutely essential for the track to exist. Detailed plots are provided in [44–47]. We conclude that there is sufficient redundancy in the upstream chambers (PCV and VDC) that the probability of having a long upstream lever arm is 100%. Individual PCF stations contribute to the track with efficiency above 98%, where the efficiency is defined as the contribution of at least two out of three expected hits at a station. This is the efficiency outside the beam regions and the location of the support wires, which also happen to be in the central region.

The section of the spectrometer downstream of the CCM magnet, consisting of the upstream and downstream (DCA and DCB, respectively) drift chamber stations and the PSA chamber, suffers from lack of acceptance in the overlap region of the PSA-DC. This is because the drift chambers have developed enlarged central dead regions, probably due to radiation damage, that are not covered by the PSA. Outside of the dead regions, the overall efficiency of the DCA-DCB-PSA combination is about 90%. This is discussed in more detail in Sec. IV D 3.

C. Muon identification efficiency

The probability that muon tracks in the forward spectrometer are matched to segments in the muon detectors is measured to be about (96.5 ± 1)%, using noninteracting beam and halo muons. The inefficiency of (3.5 ± 1)% in muon tagging can be due either to (i) inefficiency in reconstructing segments in the muon detectors or (ii) inefficiency in the criteria for matching valid forward spectrometer muon tracks to muon segments behind the hadron absorber. These probabilities can be disentangled by obtaining a sample of true muons, requiring a reconstructed forward spectrometer track and the associated segments behind the absorber, and studying the match criteria (see Sec. 5.3 of [48]). These studies show that a matching inefficiency of 2% (efficiency of 98%) can be expected independent of momentum. Thus there are no significant inefficiencies in the muon detectors.

D. Global efficiencies

We perform some additional checks on the muon reconstruction efficiency between the data and the Monte Carlo simulation.

1. Checks using noninteracting beams

The noninteracting beams can be reconstructed by the beam spectrometer independently of the forward spectrometer, and the efficiency of finding the track in the forward spectrometer can be measured.

Figure 5 shows the probability distribution of the number of hits from the various detectors contributing to the forward spectrometer track, in the beam region. The Monte Carlo simulation gives good agreement with the data. Figure 6 shows the dependence of the muon-finding efficiency on the time to the nearest beam muon, as measured by the spill local rate monitor (such multiple beams are not modeled in the Monte Carlo simulation). Negative numbers indicate buckets preceding the trigger muon and positive numbers indicate buckets following the trigger muon. We notice a sharp drop in efficiency when there is a beam muon in the preceding ten buckets or in the following five buckets. Since each rf bucket is approximately 19 ns, this corresponds to 200 ns and 100 ns, respectively. This corresponds to the amplifier dead times which cause an inefficiency in detecting the signal from the wire. A loss induced by a muon following the trigger muon is consistent with the hypothesis that such a muon could pass closer to the wire and induce a

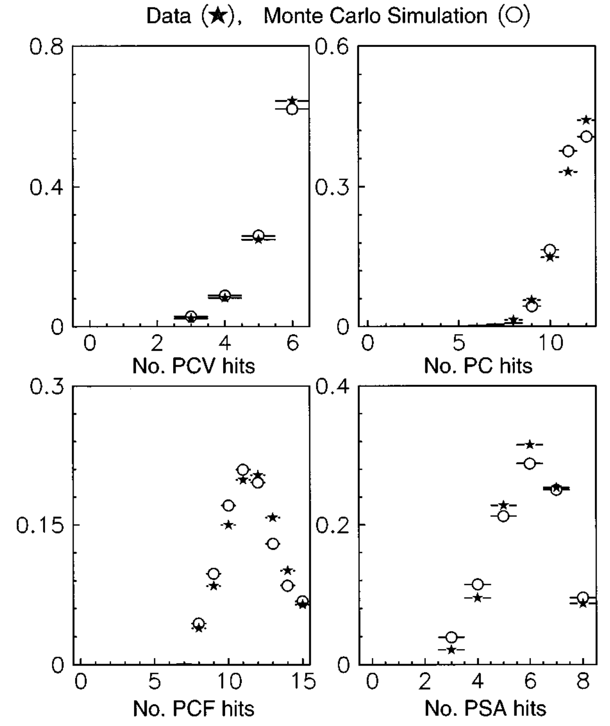

FIG. 5. Probability distribution of the number of detector hits on a track, for the data and the Monte Carlo simulation. The sample consists of noninteracting beams.

signal first. Since the PC and PCF chambers have 3 mm and 2 mm wire spacing, respectively, and the charge drift time close to the wires is about 50 ns/mm, the time scale for this source of efficiency loss is consistent with the hypothesis. We use the spill local rate monitor to eliminate from the structure function analysis all events in which there is a beam muon in the preceding ten buckets or the succeeding five buckets.

As additional confirmation of efficiency loss due to instantaneous rate, we look at events with two beams coming through the detector in the same bucket. We find an inefficiency of ~60% in reconstructing both muons (see Sec. 5.4.1 of [48]), which is consistent with our expectation of a large efficiency loss in such cases.

To summarize the results of the checks using the noninteracting beams, we conclude that the entire efficiency loss in reconstructing these tracks in the forward spectrometer is due to correlated effects. The inefficiency is about 9% before making any requirements, and can be decomposed into three components. The first component of this inefficiency, which is about 5%, is caused by out-of-time muons arriving within 100–200 ns of the in-time muon which we are interested in reconstructing. This inefficiency is probably caused by the induced dead time in the chamber electronics, and is eliminated by removing such beam muons using the spill local rate monitor information. The remaining 4% inefficiency is explained as follows. The second component of the inefficiency, which in size is about 2%, is due to a longer-lived effect induced by the intensity. We expect this to be the space charge accumulated in the beam region of the chambers, causing a reduction in the gas amplification factor and hence an inefficiency. The positive ions causing the space charge effect typically require hundreds of microseconds to be cleared. Finally, the third component of the inefficiency, another 2% effect, is produced in the muon-match procedure due to the large-angle scatters in the steel absorber. These ‘‘kinks’’ prevent the link between the forward spectrometer track and the muon segments behind the absorber.

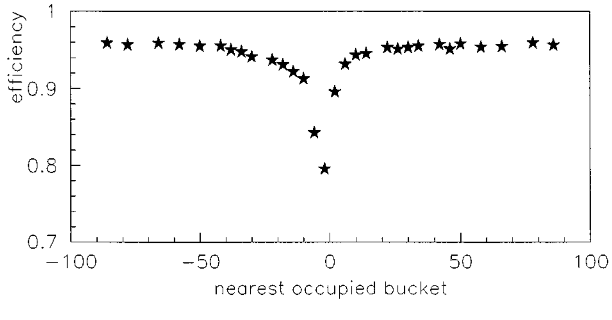

FIG. 6. Forward spectrometer muon finding efficiency for data. The efficiency is shown as a function of the nearest occupied bucket in time. The time interval per bucket is 18.8 ns. There are no ‘‘out-of-time’’ beams in the Monte Carlo simulation.

We suspect that the intensity-induced losses will be confined to the beam region of the chambers; hence, we will not use their measurements to apply overall corrections to all the data. Rather, the purpose of this study is to understand why not every noninteracting beam is reconstructed. Since the entire inefficiency is accounted for, we expect no unforseen efficiency losses that will affect the data. The one remaining issue, which is the dependence of the muon reconstruction efficiency on the final state multiplicity, is discussed in the following section.

2. Multiplicity dependence of reconstruction efficiency

While the checks with the noninteracting beams give confidence that the global forward spectrometer muon-finding efficiency can be understood, there is an aspect that cannot be addressed by this monitoring sample. This is the multiplicity dependence of the muon reconstruction efficiency. Typically, one expects the event-related multiplicity of hits to be a source of confusion and inefficiency in the pattern recognition process.

Figure 7 shows the Q^2 dependence of the average charged multiplicity in bins of W, for the events with reconstructed muons. The multiplicity is defined as the total number of tracks with defined momentum found in the event, excluding the beam and the scattered muon tracks. The data show that there is little variation of the average multiplicity with Q^2, for fixed W. This trend is reproduced by the Monte Carlo simulation over a substantial range of Q^2 and W.

We notice that the average multiplicity in the data is systematically higher than in the Monte Carlo simulation. We use the property that multiplicity is nearly independent of Q^2, to combine all Q^2 bins, and study the W dependence of the multiplicity alone. This dependence is compared between the data and the Monte Carlo simulation in Fig. 8 Measurements ([49] and references therein) have shown that in lepton scattering the multiplicity depends logarithmically on the hadronic center-of-mass energy. This behavior has also been motivated by fragmentation models such as the Feynman-Field model [50] and the LUND string model [35]. The linear

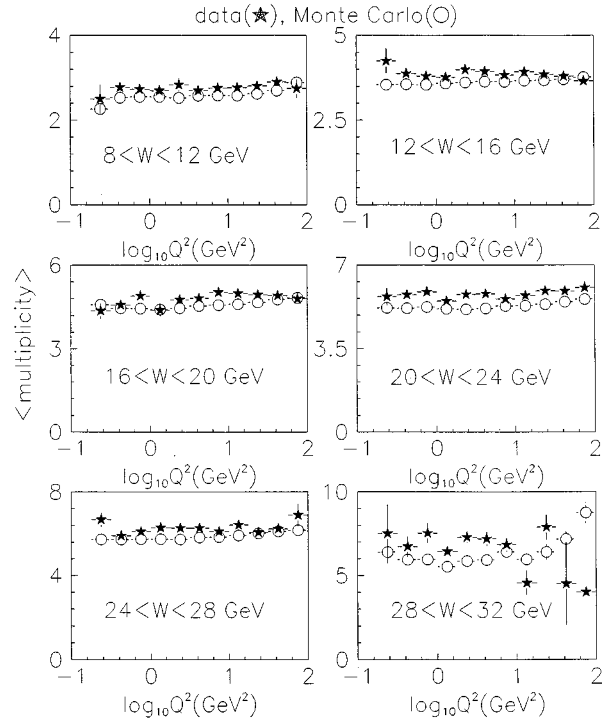

FIG. 7. Average charged multiplicity vs $\log_{10}Q^2$ in W bins, for the data and the Monte Carlo simulation (without acceptance corrections). Hadronic scatters, selected by using the calorimeter to remove μe events, are used. Only SATPS and SVS triggers are included.

dependence on $\log_{10}W$ is confirmed by the plots in Fig. 8. The Monte Carlo simulation reproduces the trend very well. We find that the average multiplicity in the data is higher by 8% than in the Monte Carlo, for any W. In order to tune the Monte Carlo simulation to match the data, we multiply the found multiplicity in a simulated event by 1.08. The tuned Monte Carlo simulation agrees well with the data, as shown in Figs. 8 and 9.

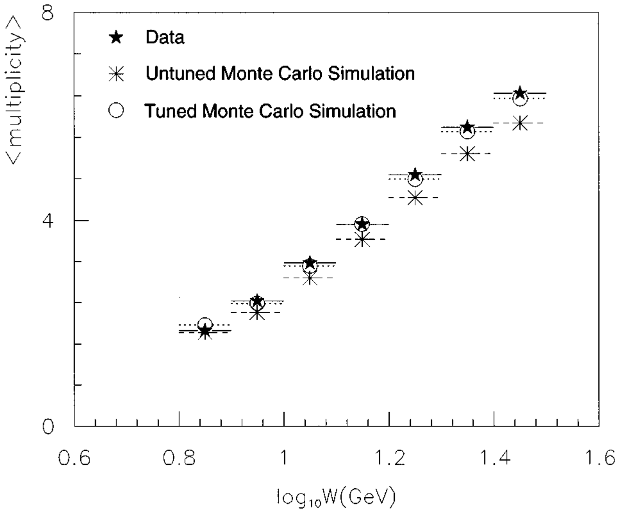

FIG. 8. Average charged multiplicity vs $\log_{10}Q^2$ in W bins, for the data and the Monte Carlo simulation. Hadronic scatters selected using the calorimeter are used. Only SATPS and SVS triggers are included. The average multiplicity in the data is higher by 8% than in the Monte Carlo simulation, for any W. The Monte Carlo simulation is tuned by scaling multiplicity by 1.08.

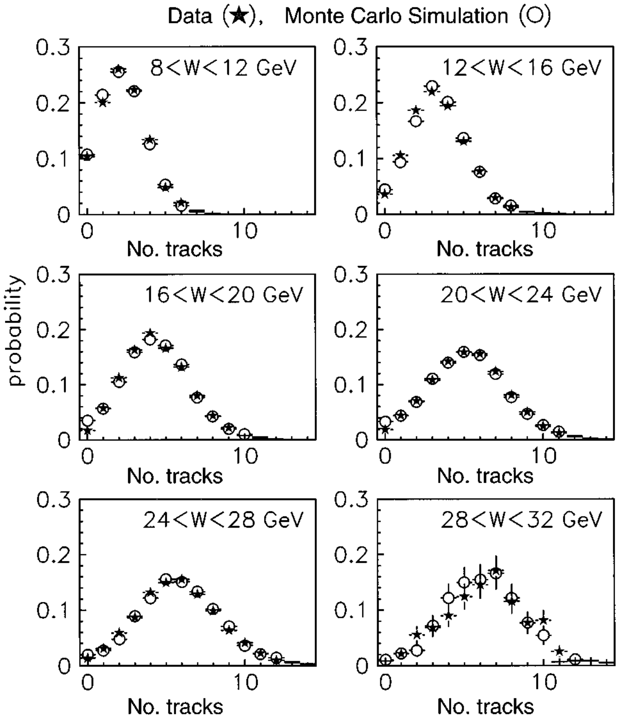

FIG. 9. Normalized multiplicity distributions in W bins, for the data and Monte Carlo simulation. Each distribution has been normalized to integrate to unity. Hadronic scatters selected using the calorimeter are used. Only SATPS and SVS triggers are included. The multiplicity in the Monte Carlo simulation has been multiplied by 1.08, giving a good match with the data.

We identify inelastic muon scattering events by using a special version of the vertex algorithm, which finds the vertex between the beam track and any forward spectrometer track, regardless of the reconstruction of the scattered muon track. By selecting events with a vertex between the beam track and at least one negative forward spectrometer track, we obtain a sample of events which is almost independent of the reconstruction of the scattered muon (which is positively charged). We require the vertex to be in the target and eliminate elastic μe scatters by using the information from the calorimeter.

Using the Monte Carlo simulation, we confirm that the sample obtained in this way consists almost entirely of muon-nucleon scatters (see Sec. 5.4.2 and Fig. 5.14 of [48]). Using this sample, we ask how often a beam muon-scattered muon vertex is reconstructed in an event of a given multiplicity. The multiplicity dependence of the muon reconstruction efficiency is measured for the different triggers on data and on the Monte Carlo. Each of the dependences is fitted with a second order polynomial in the multiplicity m, of the form

$$\varepsilon(m,\overline{\theta})=A_0+A_1m+A_2m^2, \tag{4.1}$$

where $\overline{\theta}$ is the representative scattering angle for a given trigger sample. The results are shown in Fig. 10. The effi-

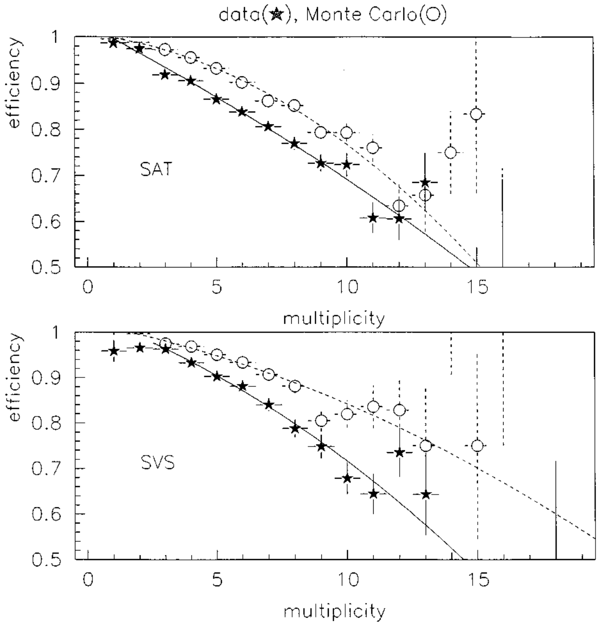

FIG. 10. Charged multiplicity dependence of the muon reconstruction efficiency measured from the data, compared with the corresponding Monte Carlo prediction. SAT and SVS trigger samples are shown here. The curves are the second order polynomial fits described in the text.

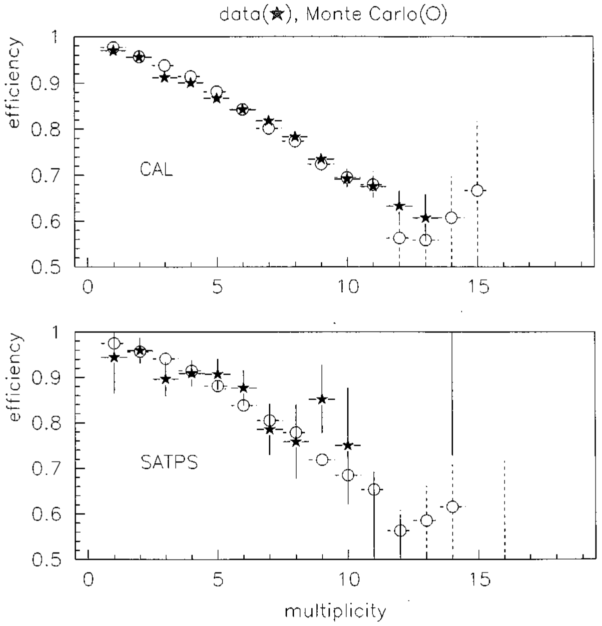

FIG. 11. Charged multiplicity dependence of the muon reconstruction efficiency measured from the data, compared with the prediction of the final tuned Monte Carlo. CAL and SATPS trigger samples are shown here.

ciencies approach unity for null multiplicity for the CAL, SATPS, SAT, and SVS triggers which were studied. This is just what we would expect based on the studies with the noninteracting beams. Apart from a 2% loss due to muon-matching inefficiency in the data, the scattered muons are always found in the absence of additional multiplicity. The inefficiencies caused by the intensity-related effects in the beam region do not affect the muons scattering through an angle of at least 1 mrad.

As the multiplicity increases, we find a significant reduction in muon-finding efficiency due to increasing event complexity. In E665, it is conceivable that this effect is enhanced due to the reversed-polarity, double-dipole magnet geometry. This magnetic field configuration refocuses the hadron tracks towards the central region of the spectrometer, thereby increasing the local density of tracks. We find that the Monte Carlo simulation is able to reproduce the bulk of this inefficiency. The comparisons show that the difference between the data measurement and the Monte Carlo predictions is typically 5%. The difference is larger for high multiplicities in the large-angle SVS trigger.

We can detect the variation of the multiplicity dependence of the efficiency with the muon scattering angle by comparing the CAL, SATPS, and SVS trigger samples. The typical values of Q^2 and scattering angle for the CAL and SVS triggers span the range of the same quantities for the SAT trigger. The mean scattering angles for CAL and SAT are about 1 mrad and 2.5 mrad, respectively, while the same for the SVS is about 8 mrad. We find that CAL and SAT measurements differ by at most a few percent, while the SVS and SAT measurements differ by less than 10%. We use a linear interpolation in scattering angle between the CAL and SVS efficiency parametrizations as an approximation for the θ^{scat} dependence.

We use these measurements to correct the Monte Carlo simulation for the residual differences between its predictions and the data measurements. For a given Monte Carlo event, we use the reconstructed multiplicity and the scattering angle to evaluate the reconstruction efficiency using the Monte Carlo parametrizations discussed above. This is the efficiency with which the Monte Carlo event would be reconstructed on average. The same event in the real data would have a slightly different efficiency, as our measurements show. To evaluate the corresponding efficiency for a similar data event, we first scale the multiplicity in the Monte Carlo event by 1.08, as discussed in the preceding section. This makes the multiplicity in the Monte Carlo match the data. Then we use the scaled multiplicity and the scattering angle to evaluate the reconstruction efficiency using the data parametrizations shown above. This gives the reconstruction efficiency, on average, that the Monte Carlo event would have if it had occurred in the real data.

We have seen that the reconstruction efficiency in the Monte Carlo is always higher than in the data. Using the evaluated data and Monte Carlo efficiencies, a given Monte Carlo event is randomly declared unreconstructed with the appropriate probability. This gives us a Monte Carlo sample that incorporates the correct muon reconstruction efficiency.

As a test of the tuned Monte Carlo simulation in this respect, the multiplicity dependence of the reconstruction efficiency is extracted from the ''corrected'' Monte Carlo and compared with the data again in Figs. 11 and 12. There is now fair agreement between the data and the final Monte Carlo simulation.

3. Downstream chamber efficiency

Up to this point we have dealt with the efficiency of finding the muon track and fitting it to the beam track in order to

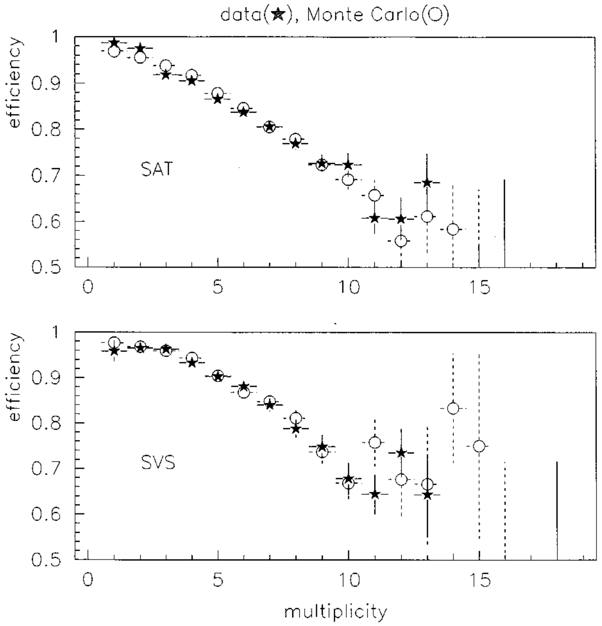

FIG. 12. Charged multiplicity dependence of the muon reconstruction efficiency measured from the data, compared with the prediction of the final tuned Monte Carlo simulation. SAT and SVS trigger samples are shown here.

obtain the muon-muon vertex. In the structure function analysis we also require high resolution. This implies that one wants muon tracks with long arm lengths on either side of the main momentum analyzing magnet CCM. As mentioned before, the upstream arm length is always long because the PCV's contribute to the track about 98% of the time, and the combined PCV-VDC contribution is 100% efficient. But the efficiency of the downstream chamber combination DCA-DCB-PSA is not so high, and so it must be studied carefully.

The track-finding program is able to find forward spectrometer tracks using the PC-PCF chambers alone. These tracks can be projected to the drift chambers and the PSA with an accuracy of a few millimeters. We use these tracks to study the position dependence of the downstream chamber efficiencies. For the scattered muon, such tracks have a poor resolution on the energy loss ν of 30–40 GeV; hence, we do not use such tracks in the final structure function analysis.

Figure 13 shows the two-dimensional position dependence of the efficiency for DCA, DCB, or PSA to contribute to a PC-PCF muon track, as measured from the data. The efficiency is shown as a function of the extrapolated position of the track at DCB. The minimum and maximum is set at 0.8 and 1.0, respectively, and the size of the boxes is proportional to the level of the efficiency above 0.8. The small circular chamber at the center is the PSA, with the drift chambers covering the wider aperture. We notice that over most of the area of the drift chambers and the PSA, the efficiencies are high and fairly independent of position. Between the left and right halves of the Z view drift chambers, there are vertical septa that cause reductions in the overall efficiency. We also note an oval-shaped region at the center of the drift chambers where there is a large efficiency loss. This is due to the fact that all the drift chambers are radiation damaged in this region, as mentioned earlier in this section.

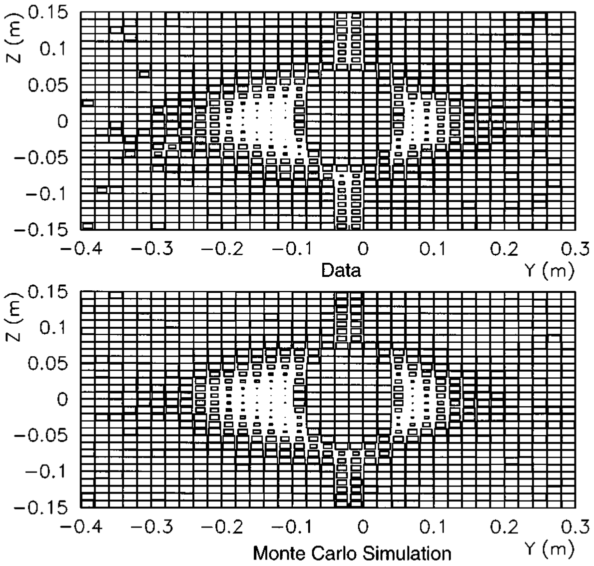

FIG. 13. DCA-DCB-PSA efficiency of contributing to the scattered muon track, measured from the data (upper) and Monte Carlo simulation (lower) using PC-PCF tracks. The efficiency is plotted vs the track coordinates at DCB.

All these effects have been incorporated into the Monte Carlo simulation. Figure 13 also shows the DC-PSA efficiency measured from the Monte Carlo simulation output the same way as it was measured from the data. Qualitatively, the Monte Carlo simulation agrees with the data. The various geometrical effects, apertures, and the drift chamber dead regions are reproduced reasonably well by the simulation. One-dimensional projections of the efficiency outside the dead regions are shown in Figs. 14 and 15 for the data and the Monte Carlo simulation, respectively.

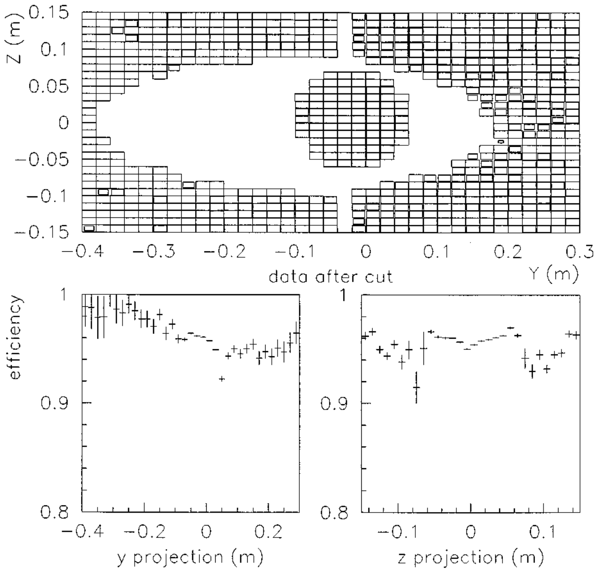

FIG. 14. DCA-DCB-PSA efficiency of contributing to the scattered muon track, measured from the data following cuts to eliminate dead regions. The efficiency is plotted vs the track coordinate at DCB.

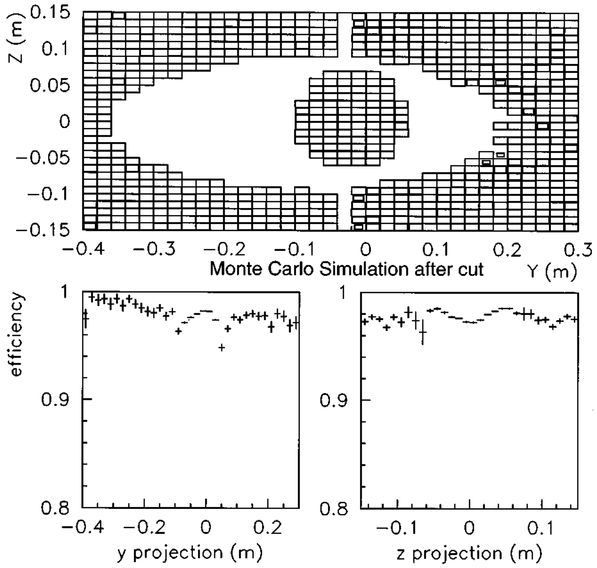

FIG. 15. DCA-DCB-PSA efficiency of contributing to the scattered muon track, measured from the Monte Carlo simulation following cuts to eliminate dead regions. The efficiency is plotted vs the track coordinate at DCB.

As a final adjustment to the Monte Carlo simulation, the histograms in Fig. 13 are used as lookup tables for the efficiency of the DC-PSA chambers. Each Monte Carlo event is reweighted by the ratio of the efficiencies for the data and the original Monte Carlo simulation, as a function of position. This technique corrects the Monte Carlo simulation for any residual difference between its DC-PSA model and the actual chambers. The final corrections for inefficiency in the data are extracted from the reweighted Monte Carlo data. The systematic uncertainty in the DC-PSA efficiency is estimated as the full size of this final adjustment to the Monte Carlo data.

Note that this correction is uncorrelated with the multiplicity correction since that correction corrects for track loss, while this correction corrects for loss of hits on a detected track.

4. Effects of field nonuniformity at large displacements

At large displacements from the center of the CCM magnet, the magnetic field becomes nonuniform. In particular, the field does not point in the vertical direction. This causes the track to bend even in the nominally ''nonbend'' view. However, the track-finding program does not take this into account, causing loss of efficiency when the muon makes a large excursion from the center of the magnet. We expect this to influence the reconstruction of scattered muons at large scattering angles.

The large scattering angle regime corresponds to the high Q^2, high x part of kinematic space, where the structure function is constrained by measurements from SLAC, BCDMS, and NMC experiments. Therefore it is fair to use the parametrization (described in Appendix XII) of F_2 fitted to these data to generate events in the Monte Carlo. In Fig. 16 we show the comparisons between self-normalized (integrating to unity) distributions of $\log_{10}\theta$ (scattering angle). The comparison shows that the Monte Carlo simulation is able to reproduce the data at small scattering angles. But at large angles, corresponding to large displacements from the center of the CCM magnet (roughly at $Y=Z=0$), the rate of reconstructed muons is significantly lower in the data than in the Monte Carlo simulation. Furthermore, the discrepancy becomes worse as the displacement and scattering angle increase. We therefore avoid those regions in this measurement. In the final analysis we will impose the cuts $-0.3\ \text{m}<Y_\mu<0.3\ \text{m}$ and $-0.2\ \text{m}<Z_\mu<0.2\ \text{m}$, where these scattered muon coordinates are measured at $X=4$ m, and $\theta_{\text{scat}}<20$ mrad.

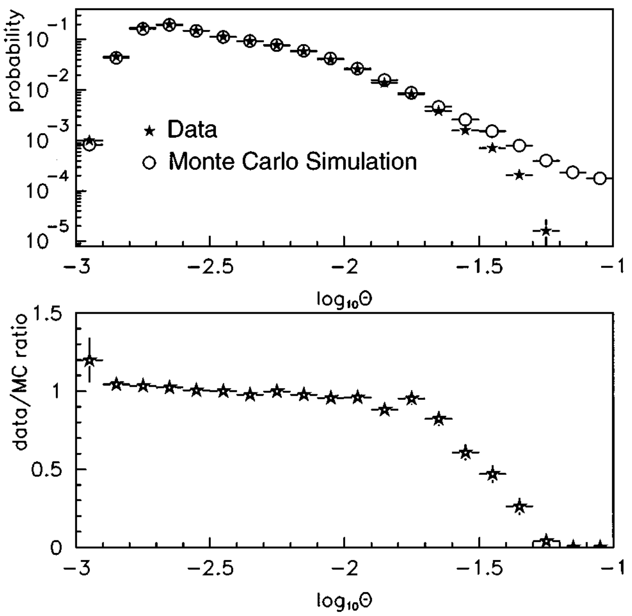

FIG. 16. Comparison between data and Monte Carlo distributions for $\log_{10}\theta$ (scattering angle). The individual distributions are normalized to integrate to unity and superposed (upper plot). The data/Monte Carlo ratio is also shown (lower plot).

E. Reconstruction efficiency predicted by Monte Carlo simulation

We now show the muon reconstruction efficiency predicted by the Monte Carlo simulation. The efficiency is shown as a function of individual kinematic variables in Fig. 17 and in two-dimensional ''box'' format vs various combinations of kinematic variables in Fig. 18. The efficiency is proportional to the area of the boxes.

We show the efficiency defined in two different ways. In Fig. 17, the curves in open circles show the efficiency defined as the probability of finding the beam muon-scattered muon vertex. The curves in solid stars show the efficiency when the following additional requirements are made on the scattered muon. The drift chamber or PSA contribution to the muon track is required, and the geometrical cuts to exclude the muon from the poorly understood regions of the DC-PSA are made. Also, the X_{vtx} cut is made (see Sec. IX B for the explanation of these requirements). Thus the latter definition of efficiency is the one ultimately relevant for the correction applied to the data. As we saw in Sec. IV D 3, the

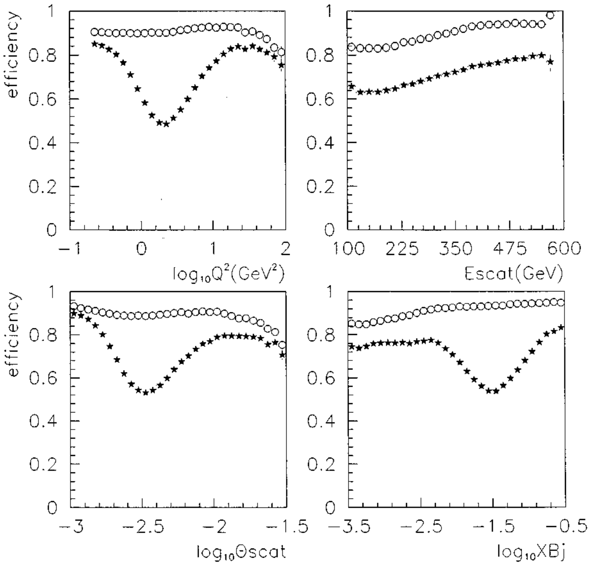

FIG. 17. Muon reconstruction efficiency predicted by the Monte Carlo simulation. The curves in solid stars show the efficiency including the DC-PSA acceptance.

low efficiency regions of the drift chambers which do not overlap the PSA are largely responsible for the loss of acceptance seen in Figs. 17 and 18.

V. TRIGGER EFFICIENCY

A. SAT efficiency

The SAT efficiency is computed using a Monte Carlo simulation of muon scatters in the detector. We can identify the following issues that need to be understood in order to calculate the trigger efficiency correctly: efficiencies of the trigger hodoscopes; the trigger logic that was implemented in the hardware; the geometry of the trigger system, i.e., the positions and sizes of the trigger hodoscopes; the magnetic fields and materials that affect the muon trajectory; the effects on the SMS veto of other particles which emerge from the absorber due to muon interactions in the absorber; and the effects on the SSA veto due to all other particles that are produced in the forward spectrometer in addition to the scattered muon. These include the particles produced in the primary muon interaction in the target and the particles produced by their subsequent reinteractions or decays.

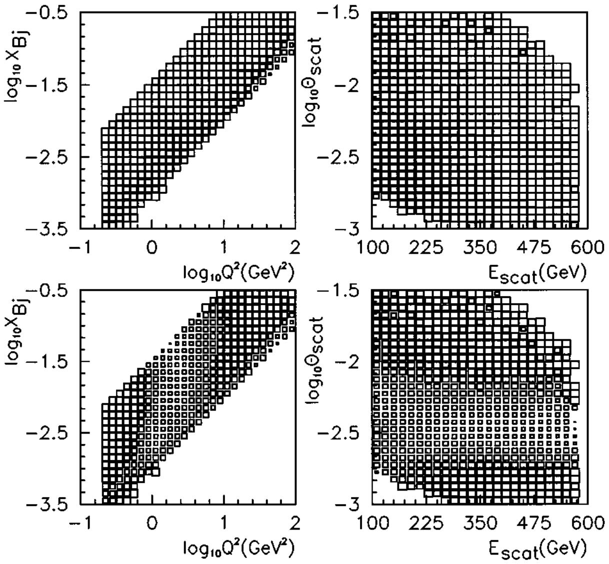

FIG. 18. Muon reconstruction efficiency predicted by the Monte Carlo simulation. The efficiency is shown in two dimensions. The lower plots show the efficiency including the DC-PSA acceptance. The minimum efficiency shown is zero and the maximum is unity.

1. Trigger hodoscope efficiencies

As mentioned above, the trigger can be decomposed into the beam requirement and the veto requirement. It is not necessary to know the absolute efficiency of the beam hodoscopes. This is because the same beam signal is randomly prescaled by a measured factor to form a random beam trigger called the RSAT. The number of RSAT's recorded gives the measure of flux that is used to normalize the number of SAT events. Hence the efficiency of the beam hodoscopes cancels in the cross-section measurement.

2. Trigger logic simulation

All individual counter signals from the trigger hodoscopes are latched and read out with any recorded event. The SAT hardware logic has been emulated in software [51] using latched counter bits in lieu of electronic pulses. Using the software and the latched bits, we can compare the predictions with the actual hardware trigger bits for RSAT, SAT, and non-SAT events. This allows us to estimate the latching efficiencies of the hodoscopes and test the software logic simulation. We find that both RSAT and SAT triggers satisfy the RSAT simulation requirements with an efficiency in excess of 98% over the entire run. The difference in the efficiencies for the two triggers is about 0.2%, which contributes a small uncertainty to the normalization of the SAT trigger. We conclude that the beam definition of the SAT trigger is well understood.

We test our understanding of the SAT trigger hardware in the following manner. We take good scatters from the SAT and non-SAT event sample, require the beam simulation to be valid, and predict whether the SAT should or should not have fired according to the latched counter signals. This should always agree with the presence or absence of the SAT hardware bit. Any disagreements are an indication of (i) latching inefficiencies or (ii) a mistake in the logic simulation. They represent systematic uncertainties in our ability to fully understand the hardware as it was when the event occurred.

The underlying distributions provided by the large-angle triggers (SVS, CVT, and SVSWAM2), the SATPS, and the CAL have different biases in scattering angle and scattered muon energy. This leads to different overlaps between these triggers and the SAT. We measure from the data that the discrepancies between the SAT hardware and software simulation are all at the level of 1.3% or less for the different samples. This suggests that the discrepancies are independent of the scattering kinematics and are instead due to a steady rate of timing or latching inefficiency or spurious pulses or latches. These conditions are fairly stable over the entire run. We assign a systematic uncertainty of 1.3% in the trigger acceptance calculation, due to lack of complete knowledge of the trigger hardware.

3. Geometry of the trigger system

In order to simulate the trigger in the Monte Carlo simulation program from first principles, we have to know the positions of all the trigger elements. The longitudinal positions are determined by survey. In the transverse direction, reconstructed tracks from the data are used to determine the positions of the veto window edges to within 1 mm.

4. Absolute probability of SMS veto

The SMS veto is constructed in the two views separately. The two upstream stations of the SMS hodoscopes in the Y view are ORed to produce the SMSY veto. Similarly the Z view hodoscopes are used to construct the SMSZ veto signal. The SMS veto signal is then constructed by taking the coincidence of the SMSY and SMSZ veto signals. In other words,

$$\mathrm{SMSV} = (\mathrm{SMS1Y} + \mathrm{SMS2Y})(\mathrm{SMS1Z} + \mathrm{SMS2Z}).$$

In order to understand the probability that an SMS veto pulse is produced, we need to consider the scenarios that lead to a particle hitting these counters. These are enumerated below.

(1) In the simplest situation, the scattered muon travels in a straight line through the absorber and hits the veto counters. The knowledge of the geometry of the veto counters enables this process to be simulated trivially.

(2) If there is more than one incoming muon in the same rf bucket, the SAT beam logic is unable to make an unambiguous prediction for the position of the unscattered muon. To guard against this situation, when there are hits in multiple beam counters, the SAT beam signal is vetoed by an electronic device called the cluster module. This feature protects the SAT trigger against events with multiple muon in the same bucket. The effect of the cluster module has been simulated using the latched hits and included in the simulation of the SAT beam. Therefore the requirement of the SAT beam in software provides an additional level of protection against multiple beams. The probability of multiple occupancy depends on instantaneous intensity, and is typically 1–2 %.

The presence of beam muons in preceding or succeeding buckets is a somewhat different issue. Muons in preceding buckets have the possibility of creating veto pulses that overflow into the bucket containing the scattered muon. The SAT beam definition includes a no-neighbor requirement for the preceding bucket; in addition, the requirement of a single reconstructed beam track removes some of these cases to the extent that the out-of-time muon can also be reconstructed in the beam spectrometer chambers.

We can actually detect and measure the timing of the out-of-time beam muons. The spill local rate monitor [52] records the beam muon occupancy of every bucket in the vicinity of the trigger time. As discussed in the section on reconstruction efficiency, events are eliminated in which there is a beam muon in the preceding ten buckets or the succeeding five buckets with respect to the trigger time. This corresponds to about 200 ns before and 100 ns after the trigger time. This is much longer than the timing resolution of the trigger veto hodoscopes, so that we expect the deleterious effects of the out-of-time beams to be completely eliminated by making this requirement.

(3) The scattered muon is deflected in the absorber through multiple Coulomb scattering or otherwise. This means that a muon that would have projected into the veto window can avoid it and vice versa. While multiple Coulomb scattering can be calculated using a simple formula, single large-angle scatters are harder to calculate. Empirically, it is found that this is not a severe problem for muons above 80 GeV, for which the deflection of the muon is less than 1 cm at the veto counters. This is one of the reasons that a cut of 100 GeV is made on the momentum of the reconstructed scattered muon in the entire analysis.

(4) The muon may emerge from the absorber accompanied by other particles. This may be due to δ ray emission or a hard electromagnetic or hadronic interaction. While the muon may not hit the veto counters, one of the other particles might do so and veto the event. It is difficult to calculate these processes reliably, and it is necessary to measure the effects and apply a correction.

The absolute probability of a SMS veto can be measured from the data by using a sample of events obtained with the Calorimeter (CAL) trigger. The CAL trigger is described in Sec. 3.6.1 of [37]. There are two salient features of this trigger that make it ideal for this measurement. First, the CAL trigger uses only the calorimeter signals to trigger on the event. In particular, no detector downstream of the hadron absorber is used. This makes the trigger completely insensitive to any muon activity in the absorber. Second, the CAL trigger is completely positive with no veto components. Therefore we obtain a sample of events unbiased with respect to muon vetos behind the absorber, which can be used to measure the veto probability in the muon veto hodoscopes.

The muon activity in the absorber can only depend on the five muon parameters measured just before it enters the absorber. These are the vertical and horizontal positions and slopes, and the energy. The longitudinal position of the SMS veto hodoscope is the most natural plane at which to report the extrapolated position of the scattered muon, assuming no deflection in the absorber.

We simplify the five muon parameters as shown in Fig. 19. The probability that a particle will hit the veto counter depends on two coordinates. One is the distance between the projected muon position and the point on the veto hodoscope that is closest to the muon. The closer the muon is to the veto counter, the larger is the overlap of the ring with the hodoscope. This distance is labeled in Fig. 19 as d. Thus one expects the veto probability to increase as d decreases. However, this probability cannot depend on d alone. For any given d, the hodoscope subtends an angle ψ at the center of the ring. As ψ increases, a larger fraction of the ring overlaps with the hodoscope, therefore again we expect the veto probability to increase.

Hence we choose d and ψ as our variables in terms of which we will parametrize the veto probability. Figure 20 shows contours of equal d and equal ψ. The measurements of the veto probability as a function of d and ψ obtained from the CAL trigger data are shown in Fig. 21.

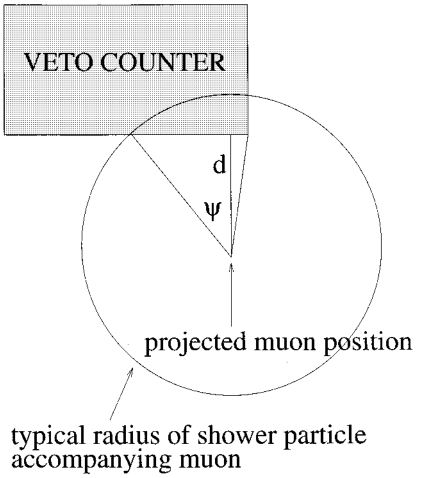

FIG. 19. Model of the muon as its extrapolated trajectory intersects the plane of the SMS veto hodoscope.

Using the regression technique, we obtain the following parametrization of the SMS veto probability:

$$\begin{aligned} P(\text{SMS veto}) &= af(d)+bg(\psi)+c \\ &= 0.19\exp(-28.6d) \\ &\quad +0.235\exp[1.63(\psi-\pi)]+0.0009. \end{aligned} \tag{5.1}$$

It is reassuring that the constant term is small as expected.

This parametric function for the SMS veto probability is used to generate hits in the SMS veto in the Monte Carlo simulation. In order to test this simulation, we ‘‘measure’’ the veto probability from the tuned Monte Carlo simulation in the same way that the measurement is made from the data. Figure 21 shows the results of the SMS veto probability ‘‘measurement’’ on the Monte Carlo simulation. We note that the Monte Carlo simulation reproduces the dependence on d and ψ, including the subtle variations with ψ which were not forced in Eq. (5.1). They are really the manifestations of the d dependence integrated over the underlying distribution.

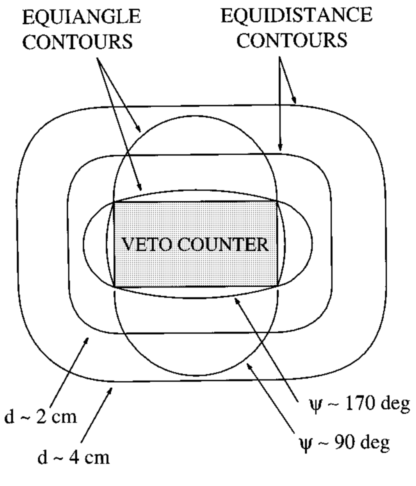

FIG. 20. Contours of equal d and ψ, which are the distance from the hodoscope and the angle subtended by the hodoscope.

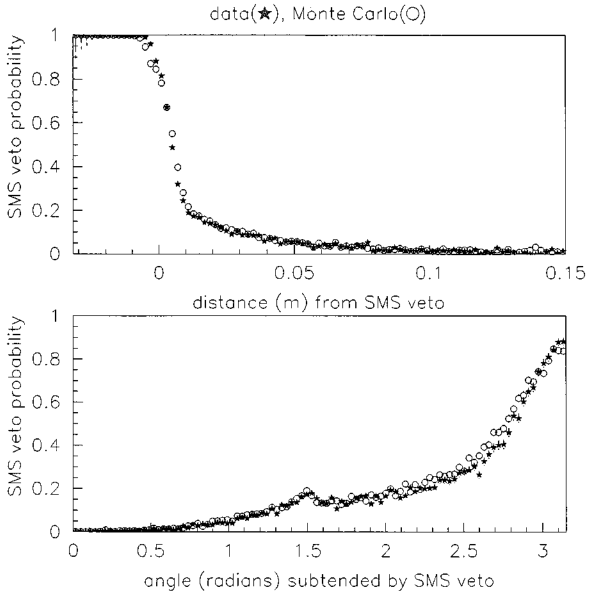

FIG. 21. SMS veto probability measured using Calorimeter trigger data and compared with the Monte Carlo simulation of the same.

The agreement between the data and the Monte Carlo simulation is quite good except in the region $|d| < 1$ cm, where the veto probability is changing rapidly. In order to be insensitive to the exact understanding of the veto probability close to the counter, we will impose a requirement $d > 0.015$ m in all the analyses. This also makes us insensitive to the 1 mm uncertainty in the position of the veto hodoscope.

We have added more terms in expression (5.1) to incorporate correlations between the d and ψ dependences. The regression analysis was repeated to find the contribution of such terms. In all cases the extra terms are found to contribute less than 1% to the veto probability. We also examined the possibility that the veto probability depends on the muon energy. We have added terms in the expression that are energy dependent, and we try linear, logarithmic, and inverse energy dependences. Again, in all cases, such terms are found to contribute less than 1% to the veto probability. We conclude that the parametrization for the SMS veto probability as a linear combination of $f(d)$ and $g(\psi)$ is adequate.

5. Absolute probability of SSA veto

We now turn our attention to the other component of the SAT veto, the SSA hodoscope. Since this hodoscope is in front of the absorber, it is sensitive to hits from the scattered muon as well as any other particle produced in the event final state. The final state includes all the other particles produced from the muon interaction in the spectrometer, upstream of the absorber.

We isolate the events in which the scattered muon does not hit the SSA veto counter, in order to study the dependence of the veto rate on final state quantities. Since the final state is produced by the collision of the nucleon and the apparent virtual photon emitted by the muon, the kinematics of the apparent virtual photon would be the natural variables

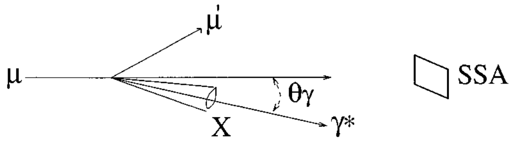

FIG. 22. A diagram depicting the final state particles produced by the apparent virtual photon, in relation to the SSA veto hodoscope.

in terms of which to parametrize the final state activity. The muon radiates the apparent virtual photon γ^*, carrying energy ν and emerging at an angle θ_γ with respect to the incoming muon direction. The apparent virtual photon is absorbed by the nucleon at rest and some final state X emerges, which on average can be represented by a cone about the direction of γ^*, as shown in Fig. 22. The probability that one of the final state particles hits the SSA veto depends on two things: (i) the number of final state particles, which depends on ν, and (ii) the angle with which they emerge, which on average is θ_γ. For small θ_γ the particles are directed towards the SSA and are more likely to hit it, while for large θ_γ they are directed away from the SSA and are likely to miss it.

For a given beam muon, the γ^* energy ν and angle θ_γ characterize the event. Hence we choose to parametrize the SSA veto probability in terms of these variables in the following manner:

$$\begin{aligned}P(\text{SSA veto}) = {} & a + b(\nu/100\ \text{GeV}) + c(\log_{10}\theta_\gamma) \\ & + d(\nu/100\ \text{GeV})^2 + e(\nu/100\ \text{GeV})(\log_{10}\theta_\gamma) \\ & + f(\log_{10}\theta_\gamma)^2, \qquad (5.2)\end{aligned}$$

where ν is in GeV and θ_γ is in radians. We use the SATPS and the large-angle triggers to provide a data sample that is unbiased with respect to the final state, because these triggers do not include any veto component upstream of the absorber. We also impose the requirement that the muon scatter in the target region, i.e., the longitudinal position of the reconstructed muon vertex (X_{vtx}) satisfy the condition -13.5 m $< X_{\text{vtx}} < -11.5$ m, because these are the events of interest, and the veto probability may depend on the point of origin of the final state particles. We also require $x_{\text{Bj}} > 0.0008$ which removes the μe scatters appearing at $x_{\text{Bj}} \sim 0.000\,545$. A regression analysis is performed on the data to calculate the coefficients a,b,c,d,e, and f. The results obtained are as follows:

$$a = 0.022\,41, \quad b = -0.069\,24,$$

$$c = -0.017\,92, \quad d = -0.002\,800,$$

$$e = -0.049\,80, \quad f = -0.008\,484.$$

.

This parametrization is then used to simulate SSA hits in the Monte Carlo simulation.

We test the accuracy of the parametrization by comparing the Monte Carlo results with the data. We compare the SSA veto probability measured from the data, using separate SATPS and LAT trigger samples, to the same ''measurements'' made from the Monte Carlo simulation. We compare the dependence of the SSA veto probability on the apparent virtual photon kinematics ν and θ_γ, the scattered muon variables θ_{scat} and ϕ_{scat}, and Q^2. These comparisons are shown in Fig. 23, and in Figs. 6.12 – 6.16 of [48]. We find that the Monte Carlo simulation reproduces the data measurements very well, for both the SATPS and LAT samples. We examine the differences between the data measurements and the Monte Carlo predictions, and find that the level differences are less than 1%. Point-to-point systematic differences are less than 2%. No adjustments are made to the Monte Carlo simulation for these differences. We take 2% as the estimate of the systematic uncertainty in the measurement of the SSA veto probability.

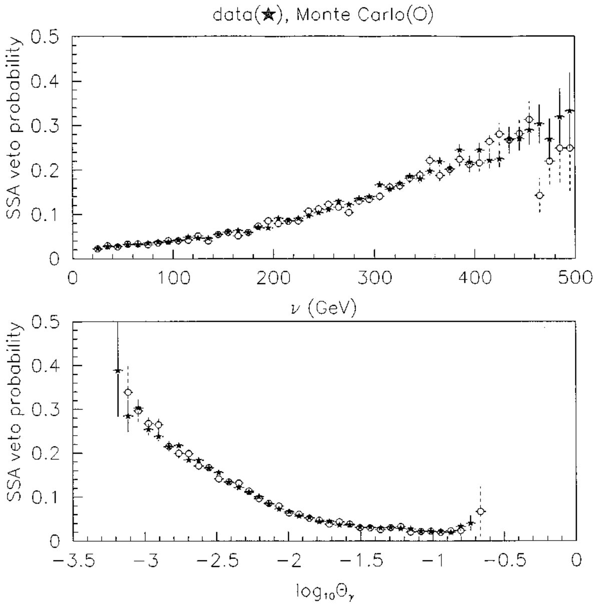

FIG. 23. SSA veto probability measured using LAT data and compared with the Monte Carlo simulation of the same.

B. SAT efficiency predicted by Monte Carlo simulation

Having incorporated all the detector-related effects into the Monte Carlo simulation, we can now use the Monte Carlo simulation to predict the SAT efficiency as a function of kinematic variables. The one-dimensional plots are shown in Fig. 24. The efficiency is shown in two-dimensional ''box'' format in Figs. 25 and 26, where the efficiency is proportional to the area of the boxes.

The SAT efficiency is computed twice with two different underlying distributions. In the first case, the underlying muon distributions are selected after all the analysis cuts described in Sec. IX, except the geometrical cuts on the muon position with respect to the SSA and SMS edges. This sample gives the absolute efficiency of the SAT, shown in Fig. 24 using open circles and in Fig. 25. The bulk of the efficiency loss at small θ and Q^2 is due to loss of geometrical acceptance (i.e., the muon hits one of the veto hodoscopes).

In the second case, we include the geometrical cut on the muon position to be outside the SSA and SMS edges (see

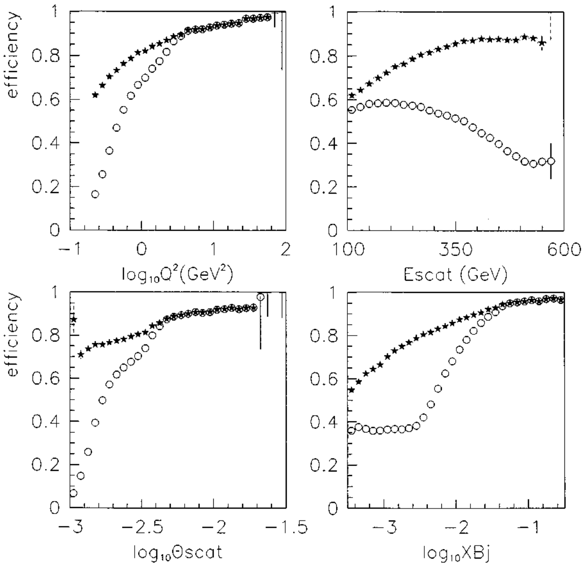

FIG. 24. SAT efficiency vs kinematic variables, predicted by the Monte Carlo simulation, shown using open circles. For the curves shown using solid stars, a geometrical cut has been made around the SMS and SSA edges on the underlying muon distribution before the efficiency is computed.

Sec. IX) in the selection of the underlying distribution. This selection absorbs the geometrical acceptance loss into the underlying distribution. The SAT efficiency recomputed with this selection is shown in Fig. 24 using solid stars and in Fig. 26. Here we see the inefficiency due to the combined effects of the vetoes induced in the SMS by the muon shower in the absorber and the vetoes induced in the SSA by the final state particles.

VI. DETECTOR CALIBRATION AND RESOLUTION

Having understood the trigger and reconstruction efficiencies, we know the fraction of muon scatters that we are able to study off line. Since we are trying to measure the double differential cross section for muon-nucleon scattering, we need to measure the kinematics of each muon-nucleon scatter. As with any measurement, there can be errors in this measurement on an event-by-event basis. These errors can be classified into two categories: (i) systematic biases and (ii) errors due to the finite resolution of the detector.

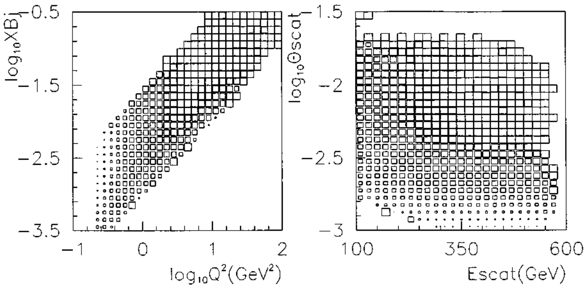

FIG. 25. SAT efficiency vs kinematic variables, predicted by the Monte Carlo simulation. The minimum efficiency shown is zero and the maximum is unity.

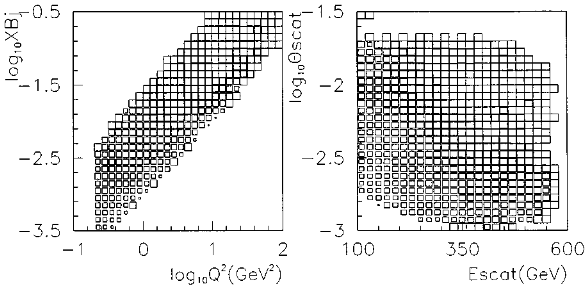

FIG. 26. SAT efficiency vs kinematic variables, predicted by the Monte Carlo simulation. A geometrical cut has been made around the SMS and SSA edges on the underlying muon distribution before the efficiency is computed. The minimum efficiency shown is zero and the maximum is unity.

A. Detector calibration

A magnetic tracking spectrometer works on the principle that the trajectory of a charged particle in a magnetic field can be calculated. The detector measures the position of the charged particle at various points along the trajectory as it passes through a region of known magnetic field. The position measurements were made in E665 using multiwire proportional chambers and drift chambers. The particle position and direction information is derived from the reconstructed trajectory, while the momentum information is induced from the measured curvature in the magnetic field and the knowledge of the field.

1. Chamber alignment and calibration

The first step in the calibration of the detector is to determine the relative positions of all the chambers in the detector. The details of this procedure can be found in [53]. First, the longitudinal positions of all the detectors, i.e., positions along the direction of the muon beam, were determined by optical survey. In order to measure the relative transverse positions, straight-line tracks were used as reference. In E665, the noninteracting beam and halo muons provided an abundant supply of particles that illuminate a large number of chambers simultaneously. Special triggers, using scintillation hodoscopes, were designed to trigger on the passage of beam and halo muons. Dedicated runs were performed periodically with these triggers and a large number of these noninteracting muons was recorded. The various magnets in the spectrometers were turned off so that the particles traveled in straight lines in the field-free regions.

2. Magnetic field measurements

There were three magnets in the E665 detector. These were the beam spectrometer dipole magnet NMRE and the two forward spectrometer dipoles CVM and CCM. Since the beam was confined to a small central region of the NMRE magnet and the magnet length was large compared to its aperture, it suffices to characterize the magnet with the transverse momentum kick it imparted to a typical beam muon. On the other hand, complete three-dimensional field maps are maintained for the CVM and CCM magnets, since particles traverse them over different regions of their large apertures.

B. Checks of the detector calibration

There are various physics measurements that can be made in order to test the calibration of the spectrometer. We will discuss each one of these in turn.

1. Primary protons from the Tevatron

The Tevatron provides a very stable beam of protons that are almost monoenergetic. Using a modified beam line, E665 took data where the primary protons were brought into the muon laboratory. The momentum measurements of the protons in the beam spectrometer and the forward spectrometer provide the absolute energy calibration for the E665 detector.

Using the values of the Tevatron magnet current settings, the momentum of the primary protons was independently determined to be (800.6 ± 2) GeV [54]. The error in the proton momentum comes mainly from the inaccuracy in the current readback of the Tevatron magnets. The transverse momentum kick of the beam spectrometer NMRE magnet was tuned such that the beam spectrometer measurement agreed with the measurement from the Tevatron. The transverse momentum kick was determined to be (1.515 ± 0.004) GeV. This gives an error estimate of 0.3% on the absolute momentum calibration using this method. The error comes mainly from the uncertainty in the primary proton momentum. The primary protons can also be used to check the measurement obtained from the forward spectrometer. The forward spectrometer measurement is (800.5 ± 0.14) GeV, where the error is statistical only [53]. This is consistent with the primary proton momentum measurement.

2. Relative momentum calibration of beam and forward spectrometers

The relative momentum calibration of the beam and forward spectrometers can also be checked using the noninteracting muons triggered by a beam trigger. The difference ν in the momentum measurements from the two spectrometers should be zero. The average of this quantity ν for noninteracting beams varies rather randomly between 0.5 GeV and 2 GeV over the entire run. The ν distribution for noninteracting beams integrating over all runs is shown in the top half of Fig. 27.

A Gaussian fit is performed, yielding a good description of the distribution. We see that the beam spectrometer measurement is systematically larger than the forward spectrometer measurement by about 1.2 GeV. We repeat the same procedure on the Monte Carlo simulation, where the detector alignment and calibration is perfect. The reconstructed Monte Carlo simulation yields a positive ν offset of about 0.6 GeV, indicating a bias in the track-fitting procedure (see lower plot in Fig. 27). We take the difference of 0.6 GeV (corresponding to 0.13% at the mean beam energy of 470 GeV), between the data and the Monte Carlo measurements as a systematic uncertainty in the relative calibration of the beam and forward spectrometers. Since we use the Monte Carlo simulation to make the final corrections to the data in order to extract the cross section, the track-fitting bias is automatically compensated for.

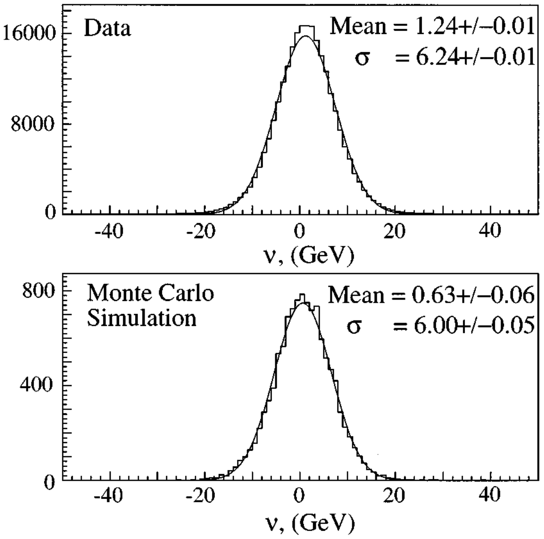

FIG. 27. Difference (ν) between momenta of noninteracting beams as measured by the beam and forward spectrometers. The upper plot is obtained from the data and the lower from the Monte Carlo simulation. The curves are Gaussian fits to the distributions, with the parameters as indicated.

3. Calibration check using muon-electron scatters

The muon-electron elastic scatters detected by the experiment offer another way to check the calibration of the spectrometer. Because of the elasticity of the event, the kinematics are constrained to give $x_{\rm Bj}=m_e/m_p$ (up to radiative corrections).

Cuts are applied to select clean μe events using their characteristic topology (described in Sec. 7.2.3 of [44]). The $\log_{10}x_{\rm Bj}$ distribution of events surviving these cuts is shown in Fig. 28. The characteristic μe peak is observed with little background. There is a tail extending to lower values of $x_{\rm Bj}$, which may be due to radiative corrections to the elastic μe peak or μN scatters not rejected by the cuts. The histogram is fitted with a sum of two Gaussians, one for the main μe peak and one to accommodate the tail. Using the main peak, we find that the mean is -3.2643 ± 0.0003 and the rms is 0.0241 ± 0.0003. This can be compared with the value calculated using the elastic μe scattering condition, $\log_{10}x_{\rm Bj} = \log_{10}(m_e/m_p) = -3.2639$. The measured $x_{\rm Bj}$ differs from the calculated value by $(0.1 \pm 0.1)\%$.

4. Calibration check using the K_S^0 mass measurement

The neutral kaon can be used to check the calibration of the forward spectrometer. The K_S^0 is detected by reconstruct-

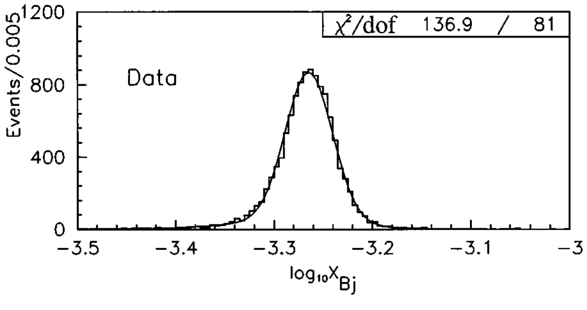

FIG. 28. $\log_{10}x_{\rm Bj}$ for data events passing the μe selection. The curve is a sum of two Gaussians fitted to the data. The mean of the main peak is -3.2643 ± 0.0003 and the rms is 0.0241 ± 0.0003.

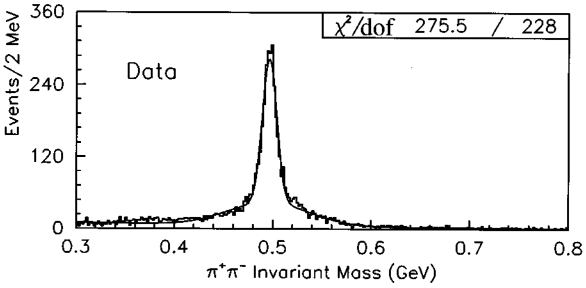

FIG. 29. The $\pi\pi$ invariant mass distribution for V^0 vertices that pass the K_s^0 selection. The curve is the sum of two Gaussians and a polynomial fitted to the data. The fitted mean of the narrow peak is (496.6±0.2) MeV and its rms is (7.4±0.3) MeV.

ing a vertex of two oppositely charged tracks, which is detached from the primary muon-muon vertex. Such a vertex has a V^0 topology, i.e., the topology of a neutral particle decaying into two charged particles of opposite sign. The sample of reconstructed V^0 candidates contains true V^0's such as K_S^0, Λ^0, and $\bar{\Lambda}^0$ decays and photon conversions $\gamma \rightarrow e^+e^-$ and also backgrounds due to small errors in the reconstructed track parameters.

We isolate a clean K_S^0 sample for the mass measurement, using cuts described in Sec. 7.2.4 of [48]. Following these cuts, we compute the invariant mass of the V^0 assigning charged pion masses to the two tracks. The resulting invariant mass distribution is shown in Fig. 29. The distribution shows a sharp peak and a broad peak, both centered near the K_S^0 mass, and a fairly flat combinatorial background. Superposed on the distribution is a fit to the sum of two Gaussians and a second order polynomial used to describe the background. The narrow peak is clearly due to the K_S^0 signal, and we take its fitted mean of (496.6±0.2) MeV to be the measured K_S^0 mass. The rms of the narrow peak is (7.4±0.3) MeV.

The measured value is about (1±0.2) MeV lower than the value published by the PDG [55] of (497.67±0.03) MeV. To use the measurement as a calibration check, we make the conservative assumption that the entire difference is due to a momentum scale error in the forward spectrometer. We scale up the momenta of both tracks by a factor of 1.003, and repeat the analysis of the K_S^0 mass measurement. This yields a value of (497.5±0.2) MeV, in good agreement with the Particle Data Group (PDG) value. Finally, we repeat the analysis once more with a scale factor of 1.005, yielding a K_S^0 mass of (498.1±0.2) MeV which overshoots the PDG value. Hence we estimate an uncertainty of 0.35% in the momentum calibration of the forward spectrometer.

C. Detector resolution

The resolution of a tracking device in free space is governed by three factors, the positions of the hits on the track, the position resolution of the individual hits contributing to the track, and the number of hits. With a good knowledge of these quantities, the expected resolution on the track parameters can be calculated. In a realistic detector, the particle traverses some amount of material and this degrades the resolution due to multiple Coulomb scattering and energy loss. In practice, the Monte Carlo simulation of the tracking spectrometer is used to calculate the resolution.

The smearing of the muon variables due to the resolution is in general dependent on the kinematics. At some specific kinematic points, we can check the calculated smearing in the Monte Carlo simulation against the data. We will use two such points, provided by the noninteracting beams and the muon-electron scatters.

1. Resolution checks using noninteracting beams

For a noninteracting muon passing through the beam and forward spectrometers, we expect the measured energy loss ν, scattering angle θ_{scat}, and the squared four-momentum transfer Q^2 to all be zero. However, a finite value will be measured due to the chamber resolution and multiple scattering. In Fig. 27, we see that the ν resolution at 470 GeV is about 6 GeV. The Monte Carlo simulation reproduces the resolution measured from the data quite well.

We have studied the Q^2 and scattering angle distributions for noninteracting beams obtained from the data and Monte Carlo simulation, respectively. The typical reconstructed values are similar for the data and Monte Carlo simulation (see Sec. 7.3.1 and Fig. 7.6 of [48]). In the range $Q^2 > 0.2$ GeV^2 in which we make the structure function measurements, the Q^2 resolution is a few percent or better. Hence we expect the smearing correction due to the angular resolution to be quite small.

2. Resolution check using muon-electron scatters

The muon-electron scatters mentioned earlier can also be used to check the resolution of the spectrometer. The width of the μe peak in the $\log_{10} x_{\mathrm{Bj}}$ distribution can be used for this purpose. As shown in Fig. 28, the width is $\delta \log_{10} x_{\mathrm{Bj}} = 0.0241 \pm 0.0003$. This corresponds to $\delta \ln x_{\mathrm{Bj}} = \delta x_{\mathrm{Bj}} / x_{\mathrm{Bj}} = 0.055$, i.e., a fractional resolution on x_{Bj} of 5.5%.

3. Estimating the resolution smearing corrections using Monte Carlo simulation

Using simulated Monte Carlo events, one can study the differences between the generated and reconstructed kinematic variables as a function of the kinematic variables. We select the muon scattering angle θ and the muon energy loss ν as the two variables whose errors on average are uncorrelated with each other. We find that the ν resolution is about 6 GeV at low ν, which is consistent with the noninteracting beam studies, and improves to about 3 GeV at high ν, where it is dominated by the error on the beam momentum. The fractional resolution on θ is about 2.5% and is only weakly dependent on θ.

This dependence is used to extract a smearing kernel for the variables $\ln\theta$ and ν. The smearing kernel is parametrized as follows:

$$\sigma_{\ln\theta} = 0.03, \quad \log_{10}\theta < -2.4,$$

$$\sigma_{\ln\theta} = 0.015 - (\log_{10}\theta + 2.0)/100.0,$$

$$\log_{10}\theta > -2.4, \tag{6.1}$$

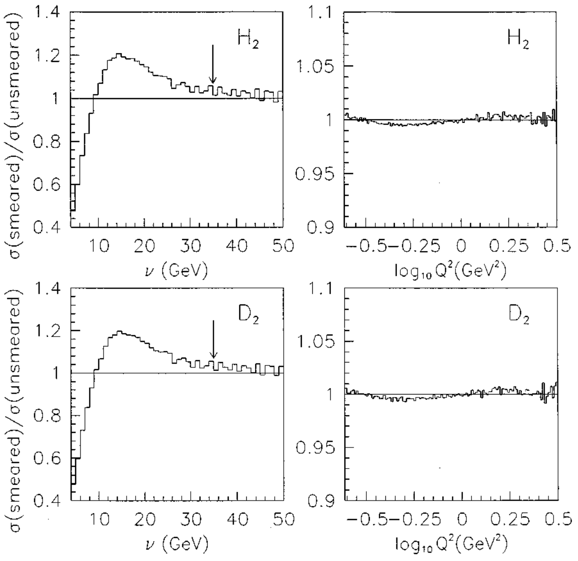

FIG. 30. Smearing correction for hydrogen and deuterium. The arrows show the position of the cut $\nu > 35$ GeV made in the structure function measurement.

and

$$\sigma_\nu = \sqrt{9.0 + (0.000\,025 E'^2)^2}, \qquad (6.2)$$

where E' is the scattered muon energy in GeV for a given ν in GeV and θ is in radians. $\sigma_{\ln\theta}$ and σ_ν (in GeV) are used as the rms of independent Gaussian random number generators.

In order to estimate the smearing correction, a fast Monte Carlo technique is used to generate about 200×10^6 events. The parametrizations of the F_2 and R structure functions and the calculated radiative corrections are used to compute the total muon cross section. This cross section is modified by the computed detector acceptance so that events can be generated according to the distribution of the triggered and reconstructed events. The kinematic variables of the generated event are randomly smeared in ν and $\ln\theta$, according to the parametrized smearing kernel.

The smearing correction is defined as the ratio of the number of smeared events to the number of generated events in a bin. The smearing corrections for hydrogen and deuterium are shown in Fig. 30. At low ν there is a significant smearing correction, but it falls below 10% for $\nu > 25$ GeV. The angular resolution is good enough that the true and smeared $\log_{10} Q^2$ distributions are very similar, and the smearing correction in Q^2 is less than 1%.

This fast Monte Carlo technique gives us an estimate of the correction to the measured cross section due to resolution smearing. In the structure function analysis, the full GEANT-based Monte Carlo simulation is used to combine all the corrections due to the detector, including the resolution smearing [see Eq. (3.5)].

VII. RADIATIVE CORRECTIONS

In this analysis, the measurement is made of the differential muon-nucleon cross section. However, the structure functions are related to the calculated cross section in the Born approximation. In this sense, the structure functions are not directly measurable quantities in a cross-section experiment. They must be extracted from the measurement by using the calculated Born cross section and the higher order QED effects, which are called radiative corrections.

A. Formulation

We refer to the formulation of Mo and Tsai [33] and Tsai [34] of the radiative corrections to lepton-nucleon scattering. According to Appendix B of [33], the radiative tails from an unpolarized target to inclusive lepton scattering can be calculated exactly to order α_{em} if (1) the single-virtual-photon-exchange mechanism is assumed, (2) the interference terms between real photon emission from the lepton and the hadron are ignored, and (3) the measurement is sensitive only to the scattered lepton.

The virtue of the diagrams where there is only one virtual photon exchanged between the hadron and the lepton is that these diagrams can be factorized into a lepton tensor and a hadron tensor. The hadron vertex has the same form as in the Born diagram, and therefore can be expressed in terms of the same structure functions. Therefore, this subset of diagrams can be calculated using the known physics for the lepton and the hadron structure functions. While the structure functions are *a priori* unknown, they can be extracted using an iterative procedure.

This factorization property does not hold for diagrams where two or more virtual photons are exchanged between the lepton and the hadron [Fig. 8.3(c) in [48]]. The effect of the double virtual photon exchange can be confirmed by comparing e^+p and e^-p scattering, because the interference of this diagram with the Born diagram is odd in the sign of the lepton charge. The difference between e^+p and e^-p scattering indicates that the effect of double virtual photon exchange is small [56]. Model-dependent calculations (see discussion in [57]) show that the double-photon-exchange terms are typically logarithms or dilogarithms with argument Q^2/xW^2. At low x the argument is of order unity, giving small values for the logarithm. The further suppression by a power of α_{em} justifies the neglect of these terms.

Henceforth we will make the assumption that the single-virtual-photon-exchange mechanism is dominant. Furthermore, in the formulation of Mo and Tsai, all electromagnetic corrections to the hadron vertex are absorbed into the definitions of the nucleon structure functions. Hence we are left with the following subset of diagrams: real photon emission off the incoming and outgoing leptons, virtual Z^0 exchange and interference between virtual photon and virtual Z^0 exchange, virtual photon correction to the lepton vertex, and loop correction to the photon propagator, including e, μ, τ, and quark loops.

Since there is an infrared catastrophe, in the sense that the cross section for the emission of very low energy (soft) photons diverges, second order effects are infinite. Some way must be found of handling this. In the method of Mo and Tsai, an energy cutoff parameter Δ is introduced to define a soft photon. At lowest order, the cancellation of the infrared divergence in the real photon emission and virtual photon vertex diagrams gives a finite remainder δ, which is a function of the cutoff parameter Δ. It has been shown [58] that δ can be calculated using the kinematics of an assumed single real photon emitted, and the emission of an infinite number of soft photons can be incorporated into the calculation by replacing $1+\delta \rightarrow e^{\delta}$. For the emission of hard photons more energetic than Δ, the lowest order calculation is used. This piece is finite and higher order contributions should be suppressed by powers of α_{em}.

In a robust calculation, the sum of the infrared piece and the hard photon piece should be independent of Δ. Studies [42] show this to be true to a very good approximation when $\Delta \sim 0.001 E_{\mathrm{beam}}$. Hence, in this analysis, Δ is chosen to be 465 MeV.

B. Results

The radiative correction is calculated by the FERRAD program [25] using the Mo and Tsai scheme. The inputs to the program are described in Sec. III B. The internal integrations in FERRAD are performed using 280 steps in hadronic W and 8 unequal intervals in the radiated photon angle optimized for speed and accuracy. Each of the 8 intervals are integrated using 35 equal steps. Further increase in the number of integration steps produced a negligible change in the result.

The radiative correction is defined by $\sigma_{\mathrm{tot}}/\sigma_{1\gamma}$, where σ_{tot} is the differential muon cross section and $\sigma_{1\gamma}$ is the Born cross section. The measured σ_{tot} is divided by this ratio to extract the Born cross section, which is then related to the structure function F_2. The correction is calculated on a 30×30 grid in x_{Bj} and y_{Bj}. The correction at any kinematic point is obtained by interpolating in a local 3×3 grid around the point of interest.

The total cross section is given by

$$\sigma_{\mathrm{tot}}=\sigma_{1\gamma}\times K(1+\mathrm{vacpol}+\mathrm{vertex}+\mathrm{weak}+\mathrm{small})+\sigma_{\mathrm{coher}} + \sigma_{\mathrm{quasi}}+\sigma_{\mathrm{inel}}, \tag{7.1}$$

where we note the following.

$K=e^{\delta}$ is the soft photon part of the radiative correction mentioned earlier. It varies between 0.9 at the low x range of the data to 0.8 at the high x range. Being less than unity indicates that in this range of x, soft photon radiation is causing more events to leak out of a bin of width Δ than leak in. It is similar for protons and deuterons because the inelastic structure functions for protons and deuterons have similar shapes over the x range of the E665 data.

''vacpol'' is the correction due to vacuum polarization effects. It varies between 2% and 7% from the low to high Q^2 range of the data. Again it is similar for protons and deuterons.

''vertex'' is the correction due to the lepton vertex loop. It varies between 0.5% at low Q^2 and 3% at high Q^2.

''weak'' is the effect of the Z^0 exchange. It increases with Q^2 but is typically smaller than 1% for $Q^2<100\ \mathrm{GeV}^2$. It is negative.

''small'' contains small corrections to the infrared nondivergent part and the soft photon part. It is negative and less than 1%.

The bulk of the radiative correction comes from real photon emission. σ_{coher}, σ_{quasi}, and σ_{inel} are the radiative tails due to hard photon radiation from other kinematic points.

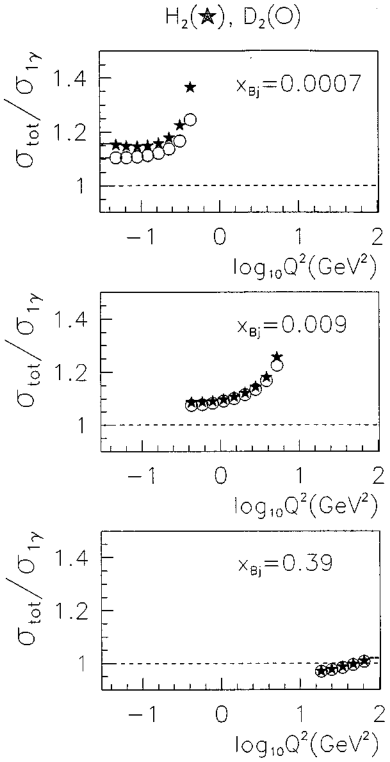

FIG. 31. Calculated radiative correction $\sigma_{\mathrm{tot}}/\sigma_{1\gamma}$ for proton and deuteron, shown as a function of $\log_{10}(Q^2/\mathrm{GeV}^2)$ in bins of x_{Bj}.

σ_{coher} is the tail from coherent nuclear scattering (zero for proton), σ_{quasi} is the tail from quasielastic muon-nucleon scattering, and σ_{inel} is the tail from inelastic scattering outside of the bin width Δ. At low x and high y, there is a large radiative correction from σ_{coher} and σ_{quasi}. This is because for elastic scattering there is no minimum energy transfer at small Q^2. There is a divergence in the muon propagator when it radiates away all its energy as a collinear high energy photon and scatters elastically as a low energy muon. This divergence is regulated only by the muon mass. In contrast, inelastic scattering always involves some energy transfer, which serves to cut off the divergence in the cross section. At low x, the sum of σ_{coher} and σ_{quasi} increases up to 30% of $\sigma_{1\gamma}$ at the highest y of the data, while at high x it is small. Since the coherent tail is missing for a proton target, and since the elastic form factors are different for protons and deuterons, the difference between the coherent and quasielastic tails for the two targets accounts for the bulk of the difference between the radiative corrections. σ_{inel} varies between about 15% and 25% of $\sigma_{1\gamma}$ from low to high x. σ_{inel} corresponds to events migrating into the bin from adjacent inelastic scattering bins. The positive contribution from σ_{inel} and the negative contribution from the K factor cancel each other to some extent.

The total radiative correction applied to the data, as a function of x_{Bj} and Q^2, is shown in Fig. 31. The correction is plotted for $y_{\mathrm{Bj}}<0.8$ because a similar cut is applied to the data sample used in this analysis. The correction is larger for the proton than the deuteron mainly because the radiative tail from elastic μp scattering is larger than the tail from quasielastic μn scattering. This radiative tail increases with y, causing the radiative correction to reach a maximum at low x and high Q^2. There it is about 40% of $\sigma_{1\gamma}$ for the proton and about 25% of $\sigma_{1\gamma}$ for the deuteron.

C. Uncertainties

The calculated radiative corrections depend on the input $\sigma_{1\gamma}$ and the approximations made in the calculation. The dependence on the input $\sigma_{1\gamma}$ is investigated by varying the inputs by their respective measurement errors. The results of this investigation are discussed in Sec. IX C 5. The accuracy of the Mo-Tsai formulation is estimated by comparing with the formulation of Bardin *et al.* This comparison [41,42] shows that, when the radiative correction is as large as 50% at low x and high y, the difference between the two calculations is less than 2%. We therefore assign the systematic uncertainty on the radiative correction to be 4% of itself, originating from calculational inaccuracy.

VIII. LUMINOSITY

The absolute normalization for the muon scattering events is provided by the luminosity. As indicated in Sec. II, the luminosity measurement requires the understanding of the beam and the target. In addition, the response kernel of the detector can depend on the beam profile. For this reason, understanding the beam implies that the total number of usable beam muons and the beam distributions be known. We shall first discuss the beam and then the target.

A. Understanding the beam

At E665 the luminosity is measured by using a variant of the technique discussed in [59]. The normalization procedure involves the following strategy. Individual beam muons are tagged and reconstructed in the beam spectrometer. The hodoscopes in the beam spectrometer are used to provide a fast electronic signal to indicate the incoming beam muon. This signal serves three purposes. First, it is used in coincidence with other signals, indicating a muon scatter to form the trigger. Second, a randomly prescaled version of this beam signal is used to form a random beam trigger. Third, the total number of beam pulses is counted by using two different scaler schemes that provide a cross-check on each other.

If the beam spectrometer response is the same for the random beam trigger and the physics trigger, then the number of usable beam muons can be accurately determined by counting the number of usable random beam triggers and multiplying this number by the prescale factor. The prescale factor is determined independently by comparing the number of random beam triggers with the number of actual beam signals counted by the scalers. This method has the advantage that the absolute beam spectrometer tagging efficiency need not be known. This efficiency includes the hodoscope and beam track reconstruction efficiencies as well as the experimental dead times and loss of events during off-line processing. In addition, it includes the loss of beam muons due to off-line cuts that are used to define the usable beam muons. As long as the beam muons in the physics triggers are subjected to the same requirements as the beams in the random beam triggers, the effect cancels in the ratio of physics triggers and random beam triggers.

1. Beam spectrometer response

As mentioned above, the experiment is designed so that the beam spectrometer response will be the same for all triggers. The only reason for the response to be different is differences in the trigger timing. This can cause changes in the latching efficiencies of electronic signals and hence change the efficiencies of various on-line and off-line requirements. A detailed study of the trigger timing [60,61] showed that all the triggers have similar timing to better than 0.5 ns. The jitter in the trigger time is about 1 ns, and the trigger time for all triggers is stable within 2 ns over the entire run.

In order to test the sensitivity of hodoscope latching efficiencies to variations in trigger time, we study the probability that the simulation of various elements of the trigger logic is satisfied. We find practically no run dependence in the probability that the SSA and SMS hodoscopes record a hit (the efficiencies are in excess of 99.7%), and in particular no correlation of their efficiencies with any trigger time variations. Therefore we conclude that the detector efficiencies are not very sensitive to any timing difference between triggers.

2. Beam counting

The issue of counting the total number of beam muons is now reduced to measuring the prescale factor for the random beam trigger. The function of prescaling the electronic beam signal is performed by special hardware circuits that provide pseudorandom prescaling [62]. These modules are programmed to provide a prescale factor of 2^{19}. To guard against small deviations from the preset value, the prescale factor is also measured using beam scalers.

Details of the scaler schemes and the prescale factor measurement are provided in [53]. Two sets of scalers are used, one being read out and reset after each spill, and the other being read out and reset after each event. The run dependence of the prescale factor is examined, and no significant deviation from the average value is found. The measurement is performed separately with the hydrogen and deuterium targets in place, and with the event scalers and spill scalers. All measurements are consistent with each other within the statistical uncertainty. The prescale factor used in this analysis for RSAT triggers is 526718 ± 800, corresponding to 0.15% uncertainty in the beam counting. The base 2 logarithm of the measured prescale factor is 19.007.

3. Beam distributions

The final aspect of understanding the beam muons is the correct reproduction of the beam distributions in the Monte Carlo simulation. This ensures that the acceptance corrections extracted from the Monte Carlo simulation have used the correct underlying distributions to average over [Eq. 3.3)]. Detailed studies of the beam distributions are provided in [26], and the procedure used to include them in the Monte Carlo generation is discussed in Sec. III. Here we provide comparisons between the beam distributions measured from the data and the Monte Carlo simulation (Fig. 32). The Monte Carlo simulation is able to reproduce the distributions.

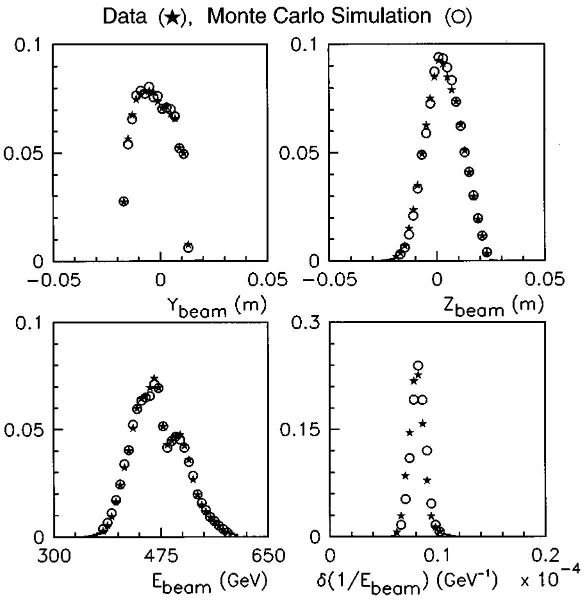

FIG. 32. Position and energy distributions of RSAT beam tracks, compared for the data and Monte Carlo simulation.

B. Understanding the target

The relevant properties of the target are the length, composition, and density. These will be discussed in turn.

1. Target length

The cryogenic liquid target vessels were cylindrical and made of Mylar, surrounded by an insulating Rohacell jacket. A vacuum was maintained between the Mylar vessel and the Rohacell jacket for insulation purposes. The lengths of the targets were measured [63] under three sets of conditions: room temperature at normal pressure, room temperature at 15 psi, and liquid nitrogen temperature at 15 psi. Using these measurements, the following lengths are inferred for the targets at 20 K:

$$\text{hydrogen: length} = (99.1 \pm 0.035)\ \text{cm},$$

$$\text{deuterium: length} = (98.9 \pm 0.035)\ \text{cm}. \tag{8.1}$$

The uncertainty includes the error in the temperature coefficient and the accuracy of the length scale. Additional small corrections are made for the semicircular vessel end caps, due to which the length of target material traversed by each beam depends on the transverse position of the beam with respect to the target axis. The uncertainty in the transverse position of the target contributes an uncertainty of 0.5% to the luminosity.

2. Target density

The saturated vapor pressures in the targets are continuously monitored and used to calculate the target temperatures and therefore the densities [53]. The density of the liquid target is fairly insensitive to the pressure. The molar density of molecular hydrogen is measured to be 0.035 022 mol/cm^3. Because of changes in the hydrogen deuteride (HD) contamination in the D_2 between different running periods, the molar density of D_2 is measured to be 0.040 346 mol/cm^3 for the early period of the run and 0.040 487 mol/cm^3 in the latter period.

3. Target composition

The chemical composition of the targets were measured using a boil-off test [53]. The deuterium target was found to be contaminated with hydrogen deuteride (HD). The HD contamination has two effects on the molar density of nucleons. First, the physical properties of HD are slightly different from D_2; therefore, at the same temperature and pressure the molecular density of the target changes due to the contamination. This is a relatively small effect. The main effect is that in a molecule of HD there is one nucleon (neutron) fewer than in a molecule of D_2. Therefore, even though the molecular density does not change very much, the nucleon density changes substantially when D_2 is replaced by HD. Furthermore, the change in the scattering rate depends on the neutron-to-proton cross-section ratio.

In order to correct the deuterium scattering rate for the HD contamination, we proceed as follows. The measured scattering rate on the deuterium target is

$$R_{\text{measured}} \propto (\alpha\sigma_d + \beta\sigma_p), \tag{8.2}$$

while the ‘‘true’’ scattering rate in the absence of HD contamination would be

$$R_{\text{true}} \propto \sigma_d, \tag{8.3}$$

where we have defined the cross sections per nucleus. $\beta+\alpha$ differs from unity because of the change in the molecular density (each molecule of HD contains the same number of protons as a molecule of D_2). α differs from unity due to the change in the molecular density as well as the absence of one neutron in an HD molecule. The α and β values are extracted using the measured HD contamination [53] and are quoted here as

$$\text{early runs:}\ \alpha = 0.983\,72, \quad \beta = 0.015\,72,$$

$$\text{later runs:}\ \alpha = 0.952\,19, \quad \beta = 0.046\,19. \tag{8.4}$$

Each scatter on the deuteron target is reweighted by the ratio $R_{\text{true}}/R_{\text{measured}}$ in order to estimate the scattering rate that would occur if the target had been pure deuterium. The correction requires the knowledge of σ_d/σ_p, for which we use the E665 measurement [53] at low x and Q^2 and the parametrization of data from previous measurements over the rest of the kinematic range. The correction is about 2.2% at low x, where σ_d/σ_p is close to 2, and is smaller at larger x.

The uncertainty in the density measurement amounts to 0.05% for hydrogen and 0.6% for deuterium. The uncertainty in the density for hydrogen comes from the uncertainty in the pressure readout accuracy and the pressure-to-density relationship. The uncertainty in the deuterium density includes this and the uncertainty in the correction for the HD contamination.

IX. STRUCTURE FUNCTION RESULTS

All of the information obtained and discussed in the previous sections is used in the extraction of the structure function. The flow of the analysis program used to obtain the results is now discussed. This will include the cuts made on the data to define the final sample. The motivation and the efficiency of the various selection criteria have already been described in the preceding sections. The results and the determination of the systematic uncertainties will be discussed.

A. Beam selection

The first step in the structure function measurement procedure is the selection of the usable beam muons. The measurement is performed by counting the scattered muon events selected by the small-angle trigger (SAT), and the luminosity is measured by counting the random beam triggers (RSAT) defined in conjunction with the SAT. The same selection is applied to the RSAT and the SAT events, which are randomly mixed with each other in the data stream. This ensures that the efficiency of the beam selection cuts cancels in the normalization of SAT to RSAT events.

The following criteria are imposed on the beam muons in the SAT and RSAT events.

(1) The very early running period shows some loss of efficiency in the drift chambers, and the very late running period shows loss of efficiency in many of the forward spectrometer chambers. Hence data from these runs are left out of the analysis.

(2) One and only one beam track should be reconstructed in the beam spectrometer. This simplifies the counting of usable beam muons and also removes any ambiguities in the reconstruction of the beam-scattered muon vertex. Approximately 10% of the events contain multiple beam tracks, most of which are out-of-time tracks.

(3) The latched hits in the beam hodoscopes are required to satisfy the SAT beam logic. This ensures that the beam track occurred in the proper time window of the trigger.

(4) The spill local rate monitor is used to identify events where a second beam muon traversed the spectrometer within the time window specified by eleven radio-frequency (rf) buckets preceding and six rf buckets succeeding the trigger bucket. These events are removed from the sample. This cut eliminates the trigger vetoes due to the out-of-time beam muons and improves the reconstruction efficiency in the forward spectrometer in the beam region.

(5) The beam track is extrapolated in a straight line from the most downstream beam station (PBT4) to the upstream and downstream face of the target (-13 m and -12 m, respectively). At each face a cut is made on the transverse coordinate of the beam, to ensure that the beam traverses the full length of the target material. The transverse position of the beam is required to be within 4.6 cm of the longitudinal axis of the target. Approximately 30% of the beam muons are removed by this cut, because the beam was hitting the edge of the target.

(6) The reconstructed beam momentum is required to be within the range of 350 and 600 GeV. A very small fraction of the events lies in the tails of the beam momentum distribution outside this range.

Following this selection, the surviving RSAT events are used to measure the luminosity, while the SAT events are subjected to further selection as discussed below. The RSAT events are weighted to correct for target length effects as discussed in Sec. VIII B 1. For nominal 1 m targets, the final number of weighted RSAT events is 159 853 for hydrogen, 100 648 for deuterium, and 31 796 for the empty target.

B. Scattered muon selection

The following cuts are made on the reconstructed parameters and the scattered muon track:

(1) The scattered muon momentum must be greater than 100 GeV. This makes the muon mismatch probability negligible, reduces the radiative corrections and the correction due to R, and also reduces the muon multiple scattering in the hadron absorber, making the trigger easier to understand.

(2) The muon energy loss ν must be greater than 35 GeV. This eliminates the contamination from noninteracting beam muons and restricts the data to the region where the smearing corrections are small.

(3) The calculated fractional error on the reconstructed ν must be less than 0.5, i.e., $\delta\nu/\nu < 0.5$. This cut was embedded in the output filter during data reconstruction. It has a minimal effect given the cut on ν.

(4) The transverse position of the scattered muon, when projected to the SMS hodoscopes defining the SAT veto window, must be at least 1.5 cm outside the edge of the window.

(5) Similarly, the transverse position of the scattered muon, when projected to the SSA hodoscope, must be at least 2.5 mm outside the edge of the SSA veto window.

(6) The longitudinal position of the reconstructed vertex must be within the range $-13.5\text{ m} < X_{\text{vtx}} < -11.5$ m. The nominal target position is between -13 m and -12 m. Because of resolution smearing in X_{vtx}, in-target scatters can be reconstructed outside this range. About 3% of the in-target scatters are lost by the requirement $-13.5\text{ m} < X_{\text{vtx}} < -11.5$ m. This loss is corrected by using Monte Carlo simulation. The off-target scatters included by the cut are statistically subtracted using empty target data.

(7) The scattered muon track is required to receive a contribution from the PSA or drift chambers. This ensures good resolution on the scattered muon.

(8) Reconstructed scattered muons extrapolating into certain regions of the drift chambers or PSA are excluded from the sample. These are in certain low efficiency regions which are straightforward to define geometrically. For the PSA, the acceptable region is defined as

$$(Y_{\text{PSA}} + 0.024)^2 + (Z_{\text{PSA}} - 0.005)^2 < 0.065^2,$$

where the coordinates are defined at the PSA in meters. This defines a circular region where all PSA chambers overlap and the efficiency is high. For the drift chambers, the muons passing through the septum region of either drift chamber station are removed. The septum regions are defined as

$$-0.005\text{ m} < Y_{\text{DCA}} < 0.035\text{ m}$$

$$-0.045\text{ m} < Y_{\text{DCB}} < -0.005\text{ m}.$$

$-0.3\ \mathrm{m} < Y_\mu < 0.3\ \mathrm{m}$ and $-0.2\ \mathrm{m} < Z_\mu < 0.2\ \mathrm{m}$, where these scattered muon coordinates are measured at $X = 4$ m, and $\theta_{\mathrm{scat}} < 20$ mrad . The motivation for these cuts is discussed in Sec. IV, where it is shown that at large distances from the center of the CCM, there is a loss of scattered muon rate in the data which is not reproduced by the Monte Carlo simulation. Since the reasons for this are not yet fully understood, we do not use the data from these outer regions of the detector in the structure function analysis.

C. Estimation of systematic uncertainties

The Monte Carlo sample of events is subjected to the same selection criteria as the data, in order to derive the corrections due to the detector response. The quality of the Monte Carlo data has been discussed extensively in the preceding sections. The studies mentioned therein are used to estimate the uncertainties in various aspects pertaining to this measurement. The systematic uncertainties that depend on the scattering kinematics are grouped in six categories: trigger efficiency, reconstruction efficiency, absolute energy scale, relative energy scale between the beam and forward spectrometers, radiative correction, and variation in R. There is also an overall normalization uncertainty which does not depend on the scattering kinematics. These sources of uncertainty will be discussed in turn.

1. Trigger efficiency

The kinematics-dependent systematic uncertainty in the SAT efficiency comes from three sources: incomplete knowledge of hodoscope geometry, SMS veto probability, and SSA veto probability.

a. Geometry. There is some uncertainty in the position of the various hodoscope elements that participate in the SAT. This limits the accuracy with which the Monte Carlo model simulates the geometrical acceptance of the SAT. To evaluate the sensitivity to the hodoscope positions, the SSA veto window is enlarged by 1 mm on each edge, and the SMS veto window is enlarged by 2 mm on each edge using the reconstructed muon track, both in the data and the Monte Carlo simulation. The acceptance correction is reevaluated from the Monte Carlo simulation and applied to the data. The fractional change in the measured F_2 $[(F_2^{\mathrm{new}} - F_2^{\mathrm{standard}})/F_2^{\mathrm{standard}}]$ is given in the column marked G in Tables A.1–A.3 of [48]. The absolute magnitude of the change (which is usually less than 2% except at the lowest Q^2) is used as the systematic error estimate.

b. SMS veto probability. Even if the muon were to fall outside the geometrical acceptance of the SMS veto, the trigger may still be vetoed by shower particles accompanying the muon as it passes through the hadron absorber. The probability of this sort of veto has been measured, and the uncertainty on the probability is estimated at 15% of itself. In order to estimate the effect of this uncertainty on each bin, the Monte Carlo parametrizations of this probability are varied in both directions by 15%. The acceptance correction is reevaluated in both cases and applied to the data. The resulting change in the measured F_2 is quoted in the columns marked M+ and M− (for an increase and decrease in the SMS veto probability) in Tables A.1–A.3 of [48]. Half of the difference between the upward and downward variation is used as the systematic uncertainty in each bin (which is typically less than 3%).

c. SSA veto probability. Even if the muon were to fall outside the geometrical acceptance of the SSA veto, the trigger may still be vetoed by hadrons or other particles produced by the muon interaction in the forward spectrometer. The probability of this sort of veto has been measured, and the uncertainty on the probability is estimated at 10% of itself. In order to estimate the effect of this uncertainty on each bin, the Monte Carlo parametrizations of this probability are varied in both directions by 10%. The acceptance correction is reevaluated in both cases and applied to the data. The resulting change in the measured F_2 is quoted in the columns marked A+ and A− (for an increase and decrease in the SSA veto probability) in Tables A.1–A.3 of [48]. Half of the difference between the upward and downward variation is used as the systematic uncertainty in each bin (which is usually less than 2%).

d. Combined uncertainty in trigger efficiency. Since the three sources of uncertainty mentioned above are independent, they are combined in quadrature to arrive at the uncertainty in F_2. This is quoted in the column marked TR in Tables I–IV.

2. Reconstruction efficiency

We include in this category the efficiency of reconstructing the scattered muon vertex (which depends on the multiplicity and the scattering angle) and the DC-PSA efficiency. These three effects are kinematics dependent.

a. Multiplicity dependence. The uncertainty in the inefficiency is estimated at 10% of the inefficiency itself, when considered a function of event multiplicity. The inefficiency is adjusted as a function of multiplicity in the Monte Carlo simulation by 10% of itself in both directions, and the data are corrected with the adjusted Monte Carlo simulation. The percent change in the measured F_2 is given in the columns marked N+ and N− respectively, in Tables A.4–A.6 of [48]. Half of the difference between the upward and downward variation is assigned as the systematic uncertainty in F_2 due to the uncertainty (which is typically less than 1.5%) in the multiplicity dependence of the efficiency.

b. Scattering angle dependence. The reconstruction efficiency can depend on scattering angle, but the Monte Carlo simulation cannot be validated by comparing with the data directly, because the scattering angle cannot be measured unless the muon is already reconstructed. We use the different triggers to obtain event distributions biased towards small and large angles, respectively. An adjustment is made to the Monte Carlo simulation to match the data by interpolating in the scattering angle. This procedure uses all available information; hence, it is used in quoting the measured F_2. The uncertainty in this procedure is estimated by ignoring the angular dependence of the Monte Carlo adjustment and redoing the F_2 measurement. The fractional change in F_2 is quoted in the column marked A in Tables A.4–A.6 of [48]. It is assigned as the systematic uncertainty due to the possibility that the angular dependence of the efficiency is not completely understood. The magnitude of this uncertainty is typically less than 2%.

c. DC-PSA efficiency. While the DC and PSA chambers are not essential for reconstructing the event, they are re-

TABLE I. Kinematics-dependent systematic uncertainty in F_2 due to various sources. Numbers are in %. TR = trigger efficiency, RE = reconstruction efficiency, EA = absolute energy scale, ER = relative energy scale between beam and forward spectrometers, RC = radiative correction, RS = variation in R_{SLAC}, and BN = bin centering and bin edge effects.

Bin center		Proton						
$\log_{10}x$	$\log_{10}Q^2$	TR	RE	EA	ER	RC	RS	BN
-3.049	-0.641	2.6	9.3	-4.3	-0.4	1.6	0.7	0.7
-3.049	-0.505	3.5	1.7	-2.2	1.4	2.1	1.4	0.6
-3.049	-0.369	4.2	7.1	0.0	-0.9	2.4	2.1	0.2
-3.049	-0.233	3.1	5.0	0.8	-1.1	3.4	2.9	1.5
-2.907	-0.641	40.2	9.6	-2.8	0.4	1.6	0.4	0.8
-2.907	-0.505	2.8	3.3	-2.4	0.0	1.7	0.8	0.5
-2.907	-0.369	4.7	1.3	-0.2	0.2	1.7	1.1	0.4
-2.907	-0.233	2.6	2.4	0.8	-0.8	2.2	1.5	0.0
-2.907	-0.097	2.8	1.9	0.9	-0.9	3.0	2.5	1.5
-2.756	-0.641	60.8	0.0	-3.6	1.9	1.5	0.2	0.7
-2.756	-0.505	8.1	1.6	-3.2	0.0	1.4	0.3	0.5
-2.756	-0.369	2.4	1.9	-2.1	-0.4	1.4	0.4	0.4
-2.756	-0.233	1.7	4.5	0.4	-0.4	1.6	0.6	0.0
-2.756	-0.097	2.4	3.4	-0.2	-0.3	1.9	1.5	0.2
-2.609	-0.505	10.0	2.1	-1.7	-0.3	1.5	0.0	0.0
-2.609	-0.369	2.5	1.2	-2.9	-0.5	1.3	0.2	0.5
-2.609	-0.233	2.2	1.4	0.2	-0.6	1.5	0.2	0.0
-2.609	-0.097	1.7	2.2	0.0	-0.3	1.5	0.7	0.3
-2.609	0.039	1.8	1.3	-0.1	-1.1	1.7	1.3	0.1
-2.609	0.175	2.1	1.4	1.8	-1.6	2.4	2.1	0.9
-2.432	-0.369	2.4	2.1	-2.3	-2.8	1.1	0.3	0.3
-2.432	-0.233	2.4	1.0	-0.2	-1.8	1.1	0.0	0.0
-2.432	-0.097	1.7	1.8	0.2	-1.7	1.1	0.2	0.0
-2.432	0.039	1.4	1.5	1.4	-0.6	1.2	0.5	0.0
-2.432	0.175	1.5	1.1	1.0	-0.4	1.5	0.9	0.1
-2.432	0.311	1.7	1.3	-1.2	-1.2	2.1	1.5	0.3
-2.284	-0.369	2.9	5.1	-3.6	-2.8	1.4	0.0	3.4
-2.284	-0.233	3.9	1.7	-0.6	-2.3	1.1	0.2	0.0
-2.284	-0.097	2.3	0.6	0.6	-2.6	1.1	0.2	0.0
-2.284	0.039	1.6	2.1	-0.7	-2.3	1.0	0.3	0.0
-2.284	0.175	1.2	1.0	-0.7	-0.6	1.2	0.4	0.0
-2.284	0.311	1.0	1.1	1.6	0.0	1.3	0.7	0.0
-2.284	0.447	2.3	2.2	-0.9	-1.4	1.3	1.2	0.6
-2.159	-0.097	2.3	1.7	-0.4	-1.3	1.2	0.2	0.0
-2.159	0.039	2.1	1.8	2.0	-1.7	1.1	0.0	0.0
-2.159	0.175	1.8	1.6	0.9	-2.7	1.0	0.2	0.0
-2.159	0.311	1.1	2.2	-1.2	-2.2	1.0	0.4	0.0
-2.159	0.447	0.9	2.7	-0.5	0.4	0.8	0.6	0.2
-2.159	0.583	1.1	3.4	0.1	-0.3	2.2	1.6	0.6
-2.049	-0.097	1.8	1.0	-1.1	-4.2	1.0	0.2	1.9
-2.049	0.039	1.5	1.3	1.6	-2.1	1.0	0.0	0.0
-2.049	0.175	0.9	2.5	1.2	0.0	1.0	0.2	0.0
-2.049	0.311	0.7	1.6	1.8	0.2	1.0	0.2	0.0
-2.049	0.447	1.0	3.2	0.5	-3.4	0.6	0.4	0.0
-2.049	0.583	1.0	2.6	-0.7	-0.6	1.7	1.0	0.0

TABLE II. Systematic uncertainty in F_2 due to various sources (continued). Numbers are in %. TR = trigger efficiency, RE = reconstruction efficiency, EA = absolute energy scale, ER = relative energy scale between beam and forward spectrometers, RC = radiative correction, RS = variation in R_{SLAC}, and BN = bin centering and bin edge effects.

Bin center		Proton						
$\log_{10}x$	$\log_{10}Q^2$	TR	RE	EA	ER	RC	RS	BN
-1.912	0.175	1.1	2.4	-0.6	-4.6	0.9	0.0	0.0
-1.912	0.311	0.9	0.6	0.9	-2.3	0.9	0.1	0.0
-1.912	0.447	0.8	0.9	0.7	1.6	0.6	0.1	0.0
-1.912	0.583	0.8	1.5	0.4	-1.5	1.2	0.5	0.0
-1.912	0.719	0.9	1.7	2.1	-1.1	1.4	1.3	0.1
-1.912	0.855	1.2	1.6	-1.2	-0.8	1.9	2.0	0.6
-1.762	0.175	1.2	0.7	2.4	-1.2	1.0	0.0	0.3
-1.762	0.311	0.9	1.5	1.5	-1.3	1.0	0.0	0.0
-1.762	0.447	0.6	0.6	-0.3	-5.0	0.6	0.0	0.3
-1.762	0.583	0.7	1.6	-0.5	-1.0	0.7	0.3	0.0
-1.762	0.719	0.4	1.0	0.5	-0.5	1.0	0.6	0.0
-1.762	0.855	1.0	2.6	1.3	-0.2	1.1	0.9	0.1
-1.762	0.991	1.3	2.6	2.4	0.0	1.6	1.8	0.5
-1.611	0.447	0.5	1.3	-2.6	-2.7	0.6	0.0	0.3
-1.611	0.583	0.6	0.9	1.6	0.2	0.7	0.2	0.0
-1.611	0.719	0.4	1.2	-0.6	-0.3	0.7	0.3	0.3
-1.611	0.855	0.9	1.3	0.8	-2.3	0.8	0.4	0.0
-1.611	0.991	0.6	2.0	-2.1	-1.6	0.9	0.8	0.1
-1.611	1.127	0.8	2.9	4.4	-0.7	1.2	1.6	1.5
-1.461	0.583	0.5	2.7	0.7	-5.1	0.7	0.0	0.1
-1.461	0.719	0.5	2.1	-0.3	-3.9	0.7	0.0	0.0
-1.461	0.855	0.4	1.5	0.7	1.5	0.6	0.1	0.0
-1.461	0.991	0.5	2.1	-0.1	-0.8	0.6	0.4	0.0
-1.461	1.127	0.8	2.1	-0.1	0.1	0.7	0.8	0.0
-1.310	0.719	0.3	1.9	0.3	-0.8	0.6	0.0	0.1
-1.310	0.855	0.4	0.7	0.0	-1.7	0.6	0.1	0.0
-1.310	0.991	0.4	1.6	1.4	-2.6	0.4	0.2	0.0
-1.310	1.127	0.1	1.3	0.1	-1.6	0.5	0.3	0.0
-1.310	1.263	0.5	2.3	1.5	-0.9	0.6	0.8	0.2
-1.310	1.399	0.8	5.7	-0.1	-0.4	0.9	1.8	1.3
-1.160	0.991	0.4	1.0	1.0	-0.7	0.5	0.1	0.3
-1.160	1.127	0.5	2.3	0.3	-1.8	0.4	0.1	0.3
-1.160	1.263	0.3	3.7	-1.0	-1.2	0.4	0.4	0.3
-1.160	1.399	0.4	2.2	-0.8	0.8	0.6	0.8	0.2
-1.160	1.535	0.7	1.9	5.2	1.0	0.8	1.5	2.7
-1.009	0.991	0.2	1.6	1.2	-3.4	0.4	0.0	2.2
-1.009	1.127	0.5	0.5	1.2	-1.5	0.4	0.0	0.2
-1.009	1.263	0.2	2.4	-0.5	-3.1	0.4	0.2	0.3
-1.009	1.399	0.3	2.5	-0.1	-3.4	0.5	0.3	0.0
-1.009	1.535	0.2	2.5	-0.8	-1.4	0.6	0.8	1.9
-0.762	1.263	0.5	0.7	3.0	-1.3	0.4	0.2	1.3
-0.762	1.399	0.2	2.3	0.8	1.2	0.2	0.0	0.8
-0.762	1.535	0.2	2.3	1.2	-1.0	0.3	0.2	0.7
-0.762	1.671	0.3	2.7	-0.8	-0.7	0.4	0.4	5.5
-0.412	1.671	0.6	1.1	2.2	-0.8	0.0	0.0	2.9
-0.412	1.808	0.3	2.4	1.1	-0.6	0.0	0.3	11.2

TABLE III. Systematic uncertainty in F_2 due to various sources (continued). Numbers are in %. TR = trigger efficiency, RE = reconstruction efficiency, EA = absolute energy scale, ER = relative energy scale between beam and forward spectrometers, RC = radiative correction, RS = variation in R_{SLAC}, and BN = bin centering and bin edge effects.

Bin center		Deuteron						
$\log_{10}x$	$\log_{10}Q^2$	TR	RE	EA	ER	RC	RS	BN
-3.049	-0.641	2.5	9.0	-7.5	0.4	1.0	0.9	0.9
-3.049	-0.505	3.1	1.5	-0.6	-0.3	1.3	1.5	0.6
-3.049	-0.369	2.7	7.3	-0.6	-0.6	1.5	2.1	0.2
-3.049	-0.233	3.0	5.3	3.3	0.0	1.9	2.9	2.3
-2.907	-0.641	32.8	10.0	-3.2	1.8	1.0	0.5	0.9
-2.907	-0.505	5.9	3.7	-3.6	0.0	1.3	0.9	0.6
-2.907	-0.369	3.0	1.3	-0.8	-0.6	1.3	1.1	0.0
-2.907	-0.233	2.3	2.5	-0.2	-0.9	1.6	1.6	0.0
-2.907	-0.097	2.7	1.8	2.8	-0.7	1.8	2.5	2.0
-2.756	-0.641	58.2	0.0	-5.4	-6.5	1.2	0.2	1.2
-2.756	-0.505	5.2	1.8	-3.4	-0.6	1.3	0.3	0.6
-2.756	-0.369	2.6	2.1	-1.4	0.7	1.3	0.5	0.5
-2.756	-0.233	1.9	4.4	-0.2	-1.5	1.1	0.6	0.0
-2.756	-0.097	2.0	3.6	0.5	-0.6	1.4	1.4	0.5
-2.609	-0.505	2.2	2.2	-2.4	0.3	1.3	0.0	0.7
-2.609	-0.369	3.6	1.3	-2.3	-1.0	1.0	0.3	0.5
-2.609	-0.233	2.4	1.8	0.6	-0.2	1.2	0.4	0.0
-2.609	-0.097	2.0	2.1	0.2	-1.0	1.1	0.5	0.0
-2.609	0.039	1.8	1.3	0.3	-0.3	1.3	1.4	0.3
-2.609	0.175	2.1	1.3	1.4	-1.1	1.7	2.2	0.5
-2.432	-0.369	4.1	1.7	-2.9	-1.8	1.2	0.0	0.5
-2.432	-0.233	1.9	1.0	-1.0	-2.0	1.1	0.2	0.4
-2.432	-0.097	1.5	1.5	0.0	-2.1	1.0	0.4	0.0
-2.432	0.039	1.6	1.5	0.5	-1.1	1.1	0.5	0.3
-2.432	0.175	1.5	1.3	0.3	-0.5	1.2	0.8	0.3
-2.432	0.311	1.8	1.1	0.5	-0.3	1.6	1.4	0.9
-2.284	-0.369	3.2	5.2	-3.7	0.3	1.3	0.3	0.6
-2.284	-0.233	2.9	1.3	-0.4	-2.5	1.1	0.0	0.0
-2.284	-0.097	3.2	0.7	1.3	-0.7	1.0	0.2	0.0
-2.284	0.039	1.8	2.0	0.0	-1.6	0.9	0.2	0.0
-2.284	0.175	1.1	1.0	0.7	-1.7	1.0	0.4	0.0
-2.284	0.311	1.1	0.9	1.7	-0.7	1.2	0.7	0.0
-2.284	0.447	2.2	2.0	-0.1	-0.7	1.1	1.4	0.2
-2.159	-0.097	1.8	1.6	0.4	-1.7	1.0	0.0	0.0
-2.159	0.039	2.4	1.7	0.8	-1.8	0.9	0.0	0.0
-2.159	0.175	0.9	1.9	0.1	-1.2	1.0	0.3	0.0
-2.159	0.311	1.0	2.3	-1.1	-1.6	0.9	0.4	0.0
-2.159	0.447	1.0	2.8	0.7	-0.5	0.8	0.8	0.0
-2.159	0.583	1.2	3.4	0.1	-1.3	1.9	1.7	0.7
-2.049	-0.097	1.7	1.2	1.2	-3.9	1.0	0.0	2.7
-2.049	0.039	1.4	1.5	0.5	-2.3	1.0	0.0	0.3
-2.049	0.175	0.9	2.4	0.9	-1.5	0.8	0.1	0.0
-2.049	0.311	1.0	1.5	0.2	-0.8	0.8	0.1	0.0
-2.049	0.447	1.1	3.2	0.9	-2.2	0.7	0.3	0.0
-2.049	0.583	0.9	2.5	-1.2	0.0	1.5	1.0	0.2

TABLE IV. Systematic uncertainty in F_2 due to various sources (continued). Numbers are in %. TR = trigger efficiency, RE = reconstruction efficiency, EA = absolute energy scale, ER = relative energy scale between beam and forward spectrometers, RC = radiative correction, RS = variation in R_{SLAC}, and BN = bin centering and bin edge effects.

Bin center		Deuteron						
$\log_{10}x$	$\log_{10}Q^2$	TR	RE	EA	ER	RC	RS	BN
-1.912	0.175	1.0	2.3	0.3	-3.7	0.9	0.0	0.0
-1.912	0.311	1.0	0.6	0.0	-1.9	0.8	0.1	0.0
-1.912	0.447	0.7	1.0	0.5	0.4	0.7	0.1	0.0
-1.912	0.583	0.7	1.5	1.2	-1.0	1.0	0.5	0.2
-1.912	0.719	0.9	1.6	0.7	0.2	1.2	1.3	0.2
-1.912	0.855	1.2	1.7	0.4	-1.1	1.6	2.0	0.3
-1.762	0.175	1.1	0.6	1.4	-1.4	0.9	0.0	0.6
-1.762	0.311	0.8	1.4	0.0	-1.3	0.8	0.0	0.3
-1.762	0.447	0.7	0.7	-0.7	-4.9	0.6	0.1	0.0
-1.762	0.583	0.9	1.5	-0.3	-0.9	0.7	0.2	0.0
-1.762	0.719	0.4	1.1	-0.2	-2.0	0.7	0.5	0.0
-1.762	0.855	1.0	2.7	2.6	0.2	0.9	0.9	0.1
-1.762	0.991	1.3	2.7	0.3	-0.4	1.4	1.9	1.1
-1.611	0.447	0.6	1.2	-1.4	-2.1	0.5	0.0	0.4
-1.611	0.583	0.6	0.8	0.4	-1.8	0.5	0.1	0.0
-1.611	0.719	0.4	1.4	-0.5	-0.9	0.7	0.3	0.0
-1.611	0.855	1.0	1.4	1.0	-0.5	0.6	0.4	0.0
-1.611	0.991	0.7	2.1	-0.1	-0.2	0.7	0.7	0.0
-1.611	1.127	0.8	2.9	3.3	-0.8	1.0	1.7	0.2
-1.461	0.583	0.5	2.9	1.3	-2.1	0.6	0.0	0.1
-1.461	0.719	0.4	2.0	1.2	-1.9	0.5	0.0	0.0
-1.461	0.855	0.4	1.2	0.7	-1.2	0.5	0.1	0.0
-1.461	0.991	0.4	1.9	1.5	-0.9	0.6	0.3	0.0
-1.461	1.127	0.7	1.9	-0.6	-0.9	0.8	0.7	0.0
-1.310	0.719	0.5	1.6	-1.1	-2.3	0.6	0.0	1.1
-1.310	0.855	0.4	0.9	1.6	-2.4	0.5	0.1	0.0
-1.310	0.991	0.4	1.7	-0.4	-2.4	0.5	0.1	0.0
-1.310	1.127	0.3	1.4	0.1	-0.4	0.5	0.4	0.0
-1.310	1.263	0.5	2.0	1.2	0.0	0.5	0.8	0.0
-1.310	1.399	0.7	6.0	4.5	1.1	0.7	1.5	8.7
-1.160	0.991	0.3	1.2	-0.7	-2.1	0.4	0.1	0.0
-1.160	1.127	0.5	2.5	0.9	-2.0	0.4	0.1	0.0
-1.160	1.263	0.2	3.5	-0.5	-2.4	0.4	0.3	0.0
-1.160	1.399	0.4	2.2	-1.4	-2.3	0.5	0.7	0.3
-1.160	1.535	0.5	2.1	-2.3	-0.5	0.7	1.7	7.3
-1.009	0.991	0.2	1.7	1.1	-1.5	0.3	0.1	1.0
-1.009	1.127	0.5	0.5	1.8	-1.1	0.2	0.2	0.3
-1.009	1.263	0.3	2.4	1.3	-2.4	0.3	0.1	0.3
-1.009	1.399	0.3	2.3	1.9	-0.3	0.3	0.3	0.0
-1.009	1.535	0.2	2.5	-0.3	-0.5	0.4	0.7	1.2
-0.762	1.263	0.4	0.8	0.2	0.2	0.2	0.0	0.9
-0.762	1.399	0.2	2.1	2.2	-0.9	0.2	0.0	0.4
-0.762	1.535	0.2	2.4	0.5	-0.7	0.4	0.2	0.4
-0.762	1.671	0.4	2.7	0.7	0.0	0.3	0.3	1.2
-0.412	1.671	0.4	0.9	2.3	2.3	0.0	0.4	1.0
-0.412	1.808	0.0	3.1	5.0	5.0	0.0	0.0	8.0

TABLE V. Fitted parameters for F_2 function.

Parameter	Proton	Deuteron
a_1	-0.0604 ± 0.0074	-0.1612 ± 0.0044
a_2	0.1962 ± 0.2497	3.1043 ± 0.2797
a_3	0.0527 ± 0.0074	0.3437 ± 0.0139
a_4	-0.7423 ± 0.0078	-0.5676 ± 0.0100
a_5	6.0061 ± 0.0083	5.9451 ± 0.0051
a_6	-9.9770 ± 0.0087	-10.1843 ± 0.0068
a_7	5.1007 ± 0.0092	4.7367 ± 0.0149
b_1	1.0686 ± 0.0879	0.0100 ± 0.0325
b_2	-8.4920 ± 1.4581	-1.2515 ± 1.8536
b_3	-0.0041 ± 0.0101	0.0296 ± 0.0084
b_4	0.0460 ± 0.0269	0.0146 ± 0.0046
c_1	0.3677 ± 0.0256	0.4118 ± 0.0259
c_2	0.0123 ± 0.0028	0.0112 ± 0.0022

quired to contribute to the scattered muon track to ensure good resolution. The efficiency of this requirement is measured from the data and Monte Carlo simulation independently (see Sec. IV D 3), and a final adjustment is made to make the Monte Carlo simulation match the data in this respect. The change in F_2 when this adjustment is removed is given in the column marked DS in Tables A.4–A.6 of [48]. The uncertainty in the efficiency of the DC-PSA requirement is estimated to be the full size of this change (which is usually less than 3%).

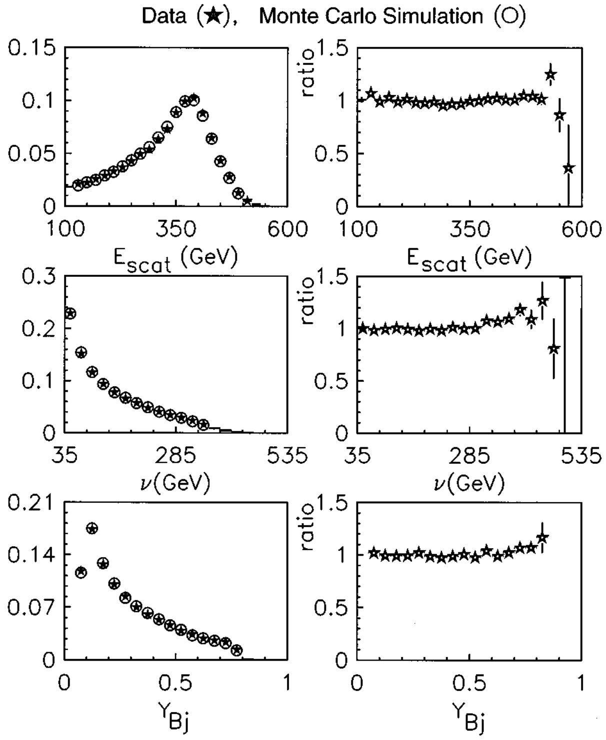

FIG. 33. (left) Final data and Monte Carlo simulation comparisons of inclusive distributions. The distributions are normalized to integrate to unity before the comparison. (right) The ratio (data/MC) of the normalized data and Monte Carlo distributions. E_{scat} is the scattered muon energy; the other variables have their usual meaning.

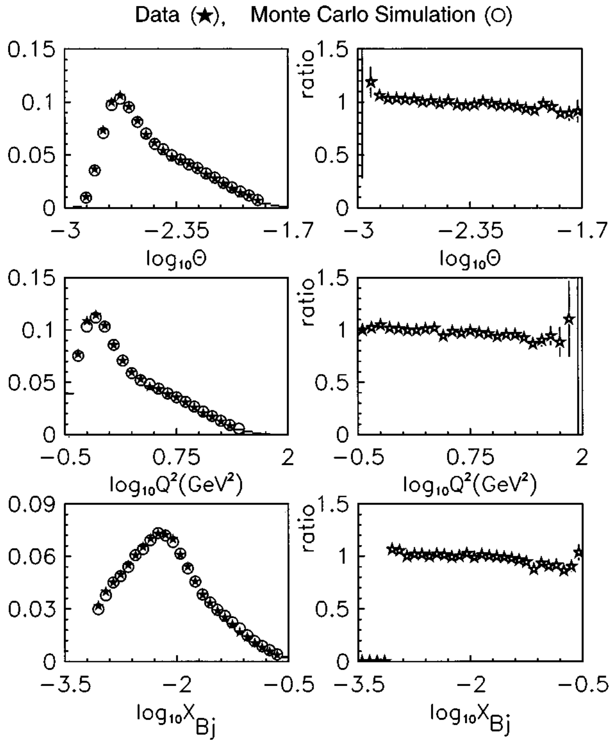

FIG. 34. (left) Final data and Monte Carlo simulation comparisons of inclusive distributions. The distributions are normalized to integrate to unity before the comparison. (right) The ratio (data/MC) of the normalized data and Monte Carlo distributions. θ is the muon scattering angle in radians; the other variables have their usual meaning.

d. Combined uncertainty in reconstruction efficiency. Since the three sources of uncertainty mentioned above are independent, they are combined in quadrature to arrive at the uncertainty in F_2. This is quoted in the column marked RE in Tables I–IV.

3. Absolute energy scale error

The uncertainty in the absolute energy scale is estimated at 0.35%. The kinematics of each event in the data is reevaluated after the beam and scattered muon momenta are scaled up by a factor of 1.0035 while preserving the scattering angle. The events are then subjected to the standard structure function analysis. The procedure is then repeated while all energies are scaled down by the same factor. Half of the difference between the F_2 obtained from these procedures is quoted as the systematic uncertainty due to the energy scale error (Tables I–IV, column EA). The sign gives the direction of the change in F_2 if the true energy scale were higher than what we nominally use.

4. Relative energy scale error

The uncertainty in the relative energy scale between the beam and forward spectrometers is estimated at 0.3%. The kinematics of each event in the data is reevaluated after the beam momentum is increased by a factor of 1.0015 and the scattered muon momentum is decreased by the same factor, while preserving the scattering angle. The events are then subjected to the standard structure function analysis. The

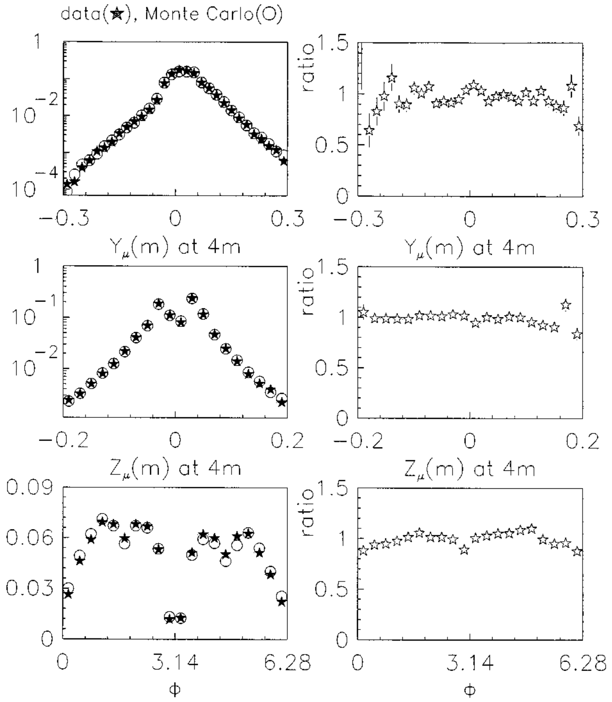

FIG. 35. (left) Final data and Monte Carlo simulation comparisons of inclusive distributions. The distributions are normalized to integrate to unity before the comparison. (right) The ratio (data/MC) of the normalized data and Monte Carlo distributions. Y_μ and Z_μ are the transverse coordinates of the reconstructed scattered muon at the longitudinal position $X=4$ m, which is just downstream of the CCM magnet. ϕ is the azimuthal angle of the muon scatter in radians.

TABLE VI. Table of F_2 with statistical and kinematics-dependent systematic uncertainties (in %).

Bin center			Proton			Deuteron	
$\log_{10}x$	$\log_{10}Q^2$	F_2	δF_2 stat	δF_2 syst	F_2	δF_2 stat	δF_2 syst
-3.049	-0.641	0.140	16.2	10.7	0.112	14.0	12.1
-3.049	-0.505	0.179	7.7	5.3	0.167	6.0	4.1
-3.049	-0.369	0.271	4.9	8.9	0.248	4.1	8.3
-3.049	-0.233	0.367	6.5	7.7	0.369	5.2	8.1
-2.907	-0.641	0.124	17.9	41.5	0.109	14.4	34.6
-2.907	-0.505	0.187	5.2	5.3	0.167	4.6	8.0
-2.907	-0.369	0.228	3.9	5.3	0.239	3.0	3.8
-2.907	-0.233	0.301	3.7	4.6	0.288	3.0	4.2
-2.907	-0.097	0.341	4.9	5.5	0.341	4.0	5.7
-2.756	-0.641	0.088	21.8	61.0	0.083	19.7	58.8
-2.756	-0.505	0.187	8.0	9.0	0.176	7.0	6.6
-2.756	-0.369	0.232	4.9	4.1	0.206	4.2	4.0
-2.756	-0.233	0.245	4.9	5.2	0.272	3.6	5.2
-2.756	-0.097	0.320	4.8	4.8	0.312	4.0	4.6
-2.609	-0.505	0.149	8.1	10.4	0.144	6.9	4.2
-2.609	-0.369	0.204	4.6	4.3	0.197	3.7	4.7
-2.609	-0.233	0.262	3.5	3.1	0.250	2.8	3.3
-2.609	-0.097	0.306	3.9	3.2	0.302	3.0	3.3
-2.609	0.039	0.357	4.5	3.3	0.372	3.4	3.0
-2.609	0.175	0.434	5.5	4.9	0.418	4.5	4.1
-2.432	-0.369	0.194	5.4	5.0	0.191	4.2	5.7
-2.432	-0.233	0.245	3.7	3.4	0.244	2.9	3.4
-2.432	-0.097	0.291	3.3	3.2	0.281	2.8	3.2
-2.432	0.039	0.317	4.4	2.9	0.314	3.4	2.8
-2.432	0.175	0.382	4.7	2.8	0.376	3.8	2.5
-2.432	0.311	0.445	6.2	3.8	0.442	4.7	3.2
-2.284	-0.369	0.178	6.5	8.3	0.175	5.2	7.3
-2.284	-0.233	0.238	4.2	5.0	0.241	3.4	4.2
-2.284	-0.097	0.270	4.0	3.7	0.273	3.2	3.7
-2.284	0.039	0.299	4.6	3.7	0.316	3.6	3.2
-2.284	0.175	0.337	5.7	2.2	0.351	4.4	2.6
-2.284	0.311	0.365	6.7	2.7	0.382	4.9	2.7
-2.284	0.447	0.441	7.4	4.0	0.427	5.7	3.6
-2.159	-0.097	0.272	4.0	3.4	0.259	3.2	3.2
-2.159	0.039	0.301	5.2	4.0	0.300	3.8	3.7
-2.159	0.175	0.329	5.4	3.9	0.344	4.2	2.6
-2.159	0.311	0.390	5.6	3.7	0.374	4.7	3.3
-2.159	0.447	0.412	6.0	3.1	0.425	4.8	3.2
-2.159	0.583	0.482	7.1	4.5	0.410	6.1	4.6
-2.049	-0.097	0.262	4.6	5.3	0.255	3.7	5.5
-2.049	0.039	0.281	5.2	3.5	0.313	3.9	3.3
-2.049	0.175	0.327	6.1	3.1	0.344	4.7	3.2
-2.049	0.311	0.422	6.0	2.7	0.417	5.0	2.2
-2.049	0.447	0.400	7.2	4.9	0.370	5.8	4.2
-2.049	0.583	0.490	6.8	3.5	0.409	6.0	3.5

procedure is then repeated while the directions of the two changes are reversed. Half of the difference between the F_2 obtained from these procedures is quoted as the systematic uncertainty due to the relative energy scale error (Tables I–IV, column ER). The sign gives the direction of the change in F_2 if the true muon energy loss were higher than what we nominally measure.

5. Radiative corrections

The uncertainty in the calculated radiative corrections arises from approximations in the calculational technique itself and the uncertainty in the input F_2. The uncertainty in the calculation is taken as 4% of itself as discussed in Sec. VII. This corresponds to an uncertainty in F_2 of less than 2%.

The kinematic plane in Q^2-W is divided into three regions: the low W region including the elastic region, the high-W–low Q^2 region including photoproduction, and the high-W–high-Q^2 region. The low W region is defined by $W<5$ GeV. For the high W region, the low and high Q^2 regions are demarcated by $Q^2=3$ GeV^2. The input F_2 is varied independently in each of the three kinematic regions by the measurement errors. The elastic cross sections and the low W structure functions are varied together in both directions by 5% and 10%, respectively [38,39,64]. In each case, the high-W–low-Q^2 and the high-W–high-Q^2 structure functions are varied in opposite directions by 10%. It is found that this variation pattern maximizes the change in the calculated radiative corrections. This procedure allows for a change in the overall magnitude of F_2 as well as a change in the slope with respect to Q^2 and W. The uncertainties in the

TABLE VII. Table of F_2 with statistical and systematic errors (in %), continued.

Bin center		Proton			Deuteron		
$\log_{10}x$	$\log_{10}Q^2$	F_2	δF_2 stat	δF_2 syst	F_2	δF_2 stat	δF_2 syst
-1.912	0.175	0.313	4.7	5.4	0.309	3.5	4.6
-1.912	0.311	0.374	4.7	2.8	0.376	3.8	2.4
-1.912	0.447	0.377	6.0	2.2	0.368	4.4	1.5
-1.912	0.583	0.408	5.7	2.6	0.430	4.3	2.6
-1.912	0.719	0.403	6.8	3.6	0.413	5.1	2.6
-1.912	0.855	0.421	10.6	3.8	0.492	6.7	3.5
-1.762	0.175	0.336	5.0	3.2	0.360	3.9	2.5
-1.762	0.311	0.340	5.7	2.8	0.360	4.5	2.2
-1.762	0.447	0.361	7.1	5.1	0.354	5.3	5.1
-1.762	0.583	0.398	6.7	2.2	0.440	5.0	2.2
-1.762	0.719	0.437	6.7	1.7	0.429	5.4	2.5
-1.762	0.855	0.435	8.1	3.3	0.454	6.3	4.1
-1.762	0.991	0.499	9.2	4.5	0.453	7.9	4.0
-1.611	0.447	0.347	5.7	4.1	0.363	4.2	2.9
-1.611	0.583	0.320	7.3	2.0	0.360	4.7	2.2
-1.611	0.719	0.394	6.7	1.7	0.392	4.9	2.0
-1.611	0.855	0.450	5.5	3.1	0.433	4.7	2.1
-1.611	0.991	0.409	8.6	3.5	0.448	6.0	2.4
-1.611	1.127	0.521	9.6	5.9	0.463	8.1	4.9
-1.461	0.583	0.336	7.6	5.9	0.383	5.3	3.9
-1.461	0.719	0.434	6.4	4.6	0.402	5.3	3.0
-1.461	0.855	0.411	7.4	2.3	0.382	6.0	1.9
-1.461	0.991	0.456	8.3	2.4	0.373	7.1	2.7
-1.461	1.127	0.464	9.9	2.4	0.386	8.4	2.5
-1.310	0.719	0.383	6.0	2.2	0.394	4.6	3.3
-1.310	0.855	0.350	6.5	2.0	0.397	4.8	3.1
-1.310	0.991	0.430	6.6	3.4	0.371	5.6	3.0
-1.310	1.127	0.415	7.2	2.2	0.408	6.0	1.6
-1.310	1.263	0.470	9.9	3.1	0.460	7.8	2.6
-1.310	1.399	0.448	18.6	6.2	0.491	13.5	11.6
-1.160	0.991	0.362	10.6	1.7	0.375	7.3	2.6
-1.160	1.127	0.390	8.8	3.1	0.403	7.1	3.4
-1.160	1.263	0.378	12.0	4.0	0.308	10.0	4.3
-1.160	1.399	0.451	13.2	2.7	0.366	12.4	3.6
-1.160	1.535	0.183	76.8	6.5	0.411	26.9	8.2
-1.009	0.991	0.367	7.1	4.6	0.360	5.7	2.7
-1.009	1.127	0.454	6.4	2.1	0.334	6.3	2.2
-1.009	1.263	0.307	12.8	4.0	0.398	7.6	3.7
-1.009	1.399	0.394	10.9	4.3	0.346	9.3	3.0
-1.009	1.535	0.265	30.4	3.6	0.253	20.1	3.0
-0.762	1.263	0.302	8.2	3.6	0.278	6.2	1.3
-0.762	1.399	0.271	10.7	2.8	0.281	7.6	3.2
-0.762	1.535	0.304	13.3	2.9	0.296	9.9	2.6
-0.762	1.671	0.313	21.5	6.3	0.340	15.2	3.1
-0.412	1.671	0.205	23.7	4.0	0.147	20.4	3.6
-0.412	1.808	0.191	34.0	11.5	0.151	31.6	11.1

TABLE VIII. Bin acceptance for total muon cross section, with statistical error (in %).

Bin center			
$\log_{10}x$	$\log_{10}Q^2$	Acceptance	Error (stat)
-3.049	-0.641	0.025	7.6
-3.049	-0.505	0.135	3.1
-3.049	-0.369	0.272	2.2
-3.049	-0.233	0.192	2.8
-2.907	-0.641	0.012	7.6
-2.907	-0.505	0.093	2.6
-2.907	-0.369	0.240	1.6
-2.907	-0.233	0.316	1.4
-2.907	-0.097	0.224	2.0
-2.756	-0.641	0.007	11.4
-2.756	-0.505	0.058	4.1
-2.756	-0.369	0.199	2.2
-2.756	-0.233	0.324	1.8
-2.756	-0.097	0.331	2.0
-2.609	-0.505	0.044	3.8
-2.609	-0.369	0.164	1.9
-2.609	-0.233	0.316	1.3
-2.609	-0.097	0.345	1.4
-2.609	0.039	0.331	1.6
-2.609	0.175	0.251	2.1
-2.432	-0.369	0.136	2.1
-2.432	-0.233	0.295	1.4
-2.432	-0.097	0.373	1.3
-2.432	0.039	0.345	1.5
-2.432	0.175	0.343	1.7
-2.432	0.311	0.322	2.1
-2.284	-0.369	0.122	2.7
-2.284	-0.233	0.281	1.8
-2.284	-0.097	0.387	1.5
-2.284	0.039	0.374	1.7
-2.284	0.175	0.341	1.9
-2.284	0.311	0.384	2.1
-2.284	0.447	0.394	2.4
-2.159	-0.097	0.382	1.5
-2.159	0.039	0.374	1.7
-2.159	0.175	0.343	1.9
-2.159	0.311	0.365	2.1
-2.159	0.447	0.448	2.2
-2.159	0.583	0.470	2.6
-2.049	-0.097	0.386	1.8
-2.049	0.039	0.382	1.9
-2.049	0.175	0.349	2.2
-2.049	0.311	0.345	2.4
-2.049	0.447	0.426	2.4
-2.049	0.583	0.522	2.6

photoproduction cross section (~5% [21]), the high W inelastic structure functions, and the interpolation between them at very low Q^2 are taken into account.

Following this procedure, four sets of calculated radiative corrections are obtained, each of which is used to reevaluate the measured F_2. The fractional change in each case from the standard measurement is discussed in Sec. 10.3.5 and Tables A.7–A.9 of [48].

The systematic uncertainty in the measured F_2 in each bin is taken as half of the maximum variation between any two of the four measurements. The uncertainty from this source is usually less than 1.5%. It is added in quadrature with the

TABLE IX. Bin acceptance for total muon cross section, with statistical error (in %), continued.

Bin center			
$\log_{10}x$	$\log_{10}Q^2$	Acceptance	Error (stat)
-1.912	0.175	0.361	1.5
-1.912	0.311	0.347	1.7
-1.912	0.447	0.427	1.7
-1.912	0.583	0.503	1.8
-1.912	0.719	0.592	2.0
-1.912	0.855	0.505	2.7
-1.762	0.175	0.351	1.9
-1.762	0.311	0.352	2.1
-1.762	0.447	0.395	2.2
-1.762	0.583	0.482	2.1
-1.762	0.719	0.579	2.3
-1.762	0.855	0.671	2.8
-1.762	0.991	0.581	3.4
-1.611	0.447	0.399	1.8
-1.611	0.583	0.484	1.8
-1.611	0.719	0.566	1.9
-1.611	0.855	0.669	1.9
-1.611	0.991	0.704	2.3
-1.611	1.127	0.561	3.5
-1.461	0.583	0.465	2.3
-1.461	0.719	0.560	2.3
-1.461	0.855	0.661	2.4
-1.461	0.991	0.715	2.6
-1.461	1.127	0.744	3.2
-1.310	0.719	0.565	1.9
-1.310	0.855	0.657	1.9
-1.310	0.991	0.737	2.0
-1.310	1.127	0.818	2.2
-1.310	1.263	0.699	3.1
-1.310	1.399	0.365	6.1
-1.160	0.991	0.705	2.6
-1.160	1.127	0.803	2.7
-1.160	1.263	0.805	3.0
-1.160	1.399	0.580	4.7
-1.160	1.535	0.260	10.9
-1.009	0.991	0.711	2.3
-1.009	1.127	0.775	2.4
-1.009	1.263	0.787	2.5
-1.009	1.399	0.784	3.5
-1.009	1.535	0.462	5.4
-0.762	1.263	0.833	1.9
-0.762	1.399	0.790	2.2
-0.762	1.535	0.641	3.2
-0.762	1.671	0.353	6.2
-0.412	1.671	0.433	6.3
-0.412	1.808	0.237	11.8

uncertainty in the calculational technique, to quote the total systematic uncertainty due to radiative corrections (column RC, Tables I–IV).

6. Variation in R

The extraction of F_2 from $\sigma_{1\gamma}$ requires the knowledge of $R=\sigma_L/\sigma_T$. We have used R_{SLAC}, which is obtained from a global analysis of SLAC data [53]. The given functional form of the fitted R_{SLAC} is used to evaluate R in the entire range of x and Q^2 of this measurement. The details are provided in Appendix C of [48]. The systematic uncertainty in F_2 is quoted by varying R_{SLAC} in both directions by the given error on it. The fractional change in F_2 due to either variation in R_{SLAC} is given in the columns marked R_s+ and R_s- in Tables A.10–A.12 of [48]. Half of the difference is quoted as the systematic uncertainty in F_2 due to variation in R_{SLAC} (under the column marked **RS** in Tables I–IV). In tables A.10-A.12 of [48] we have also quoted the fractional change in F_2 when we assume $R=0$, and $R=R_{\text{QCD}}$. The parametric expression for R_{QCD} that is used is given in Appendix C of [48]. In the column marked R_A of Tables A.10–A.12 of [48], we quote the fractional change in F_2 when we use R calculated using the modified Martin-Roberts-Stirling set A [MRS(A)] set of parton distributions in the modified minimal subtraction ($\overline{\text{MS}}$) scheme [65]. The change in F_2 produced by these alternate choices for R is usually no more than a few percent, except at the lowest x and highest y of the data, where it is up to 10%.

7. Bin edges and bin centering

The kinematic boundaries in ν and E_{scat} cut through the bins in x and Q^2, making the bins at the edges of the kinematic phase space difficult to understand. In order to select the usable bins, the F_2 measurement is performed with the set of cuts $\nu>25$ GeV, $E_{\text{scat}}>80$ GeV and again with the cuts $\nu>50$ GeV, $E_{\text{scat}}>120$ GeV. In each case the acceptance in each bin is recomputed from the Monte Carlo simulation using the same cuts. The measurements are compared bin to bin, and any bin in which the measurement changes by more than 5% is removed. This method only removes the edge bins. The final F_2 measurements are quoted in the remaining bins. To measure the residual uncertainty due to the kinematic cuts, the measurement is repeated using the cuts $\nu>25$ GeV, $E_{\text{scat}}>90$ GeV and $\nu>45$ GeV, $E_{\text{scat}}>110$ GeV. Half of the difference in each bin is included in the systematic uncertainty. A similar procedure is applied for understanding the effect of the cuts on the Y and Z positions of the scattered muon at $X=4$ m and the maximum scattering angle cut. The F_2 measurement is repeated after removing the maximum scattering angle cut, while maintaining the Y and Z position cuts. The measurement changes only at the high-Q^2 edge bins and always less than 10% except in two bins. These two bins are removed. In the remaining bins the change is used as an estimate of the systematic uncertainty due to the combination of bin edge effects and the detector modeling at large scattering angles.

The structure function is defined at kinematic points; however, the measurement is performed in bins (the bin width is about 30% in x_{Bj} and Q^2). This means the measurement produces a bin-integrated average. In order to quote a value at bin center, an estimate of the derivatives of F_2 beyond the first derivative is required (for a linear function, the bin-integrated average is equal to the value at bin center). We have used the parametrization of F_2 described in Appendix XII to estimate the correction due to the derivatives beyond first order. We have chosen to quote F_2 at the center of the bin in $\log_{10}x$ and $\log_{10}Q^2$. The bin-centering correction

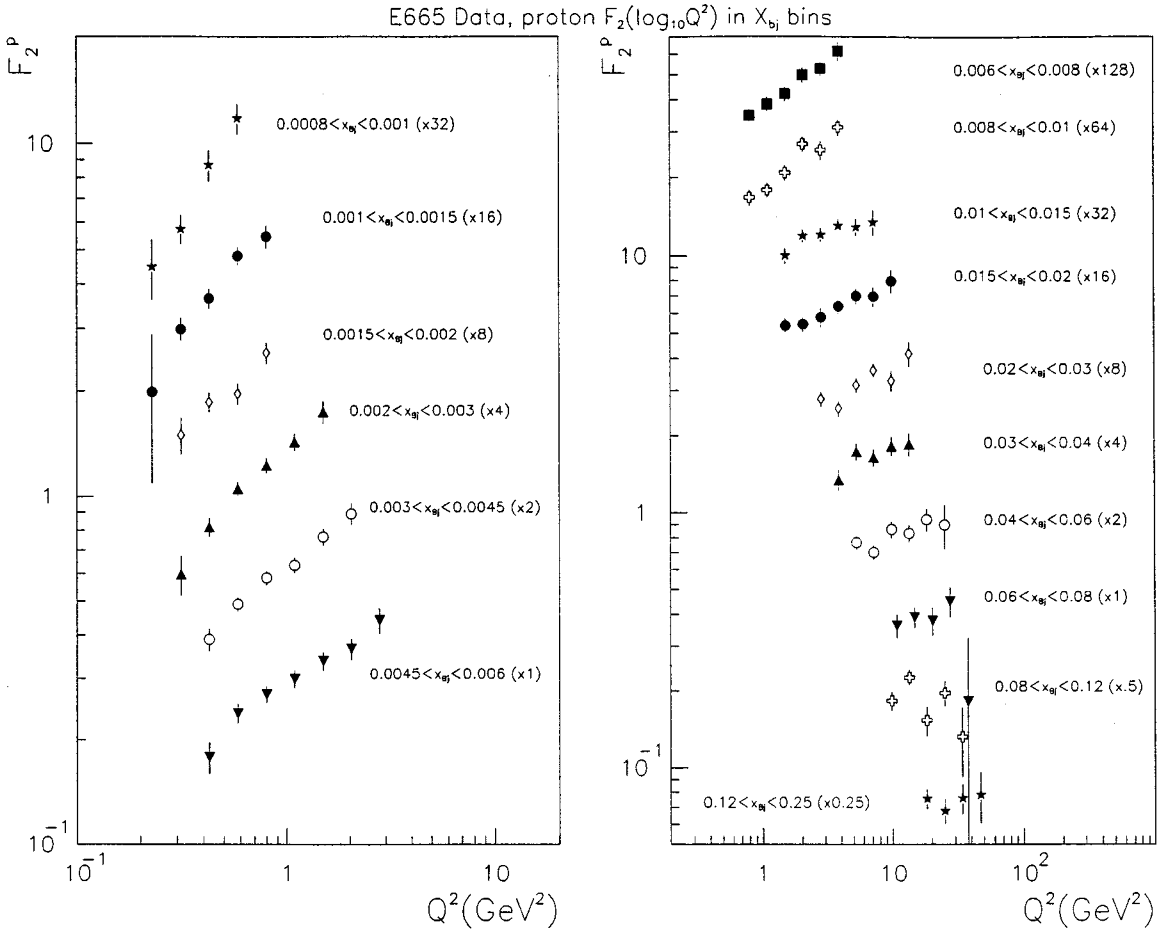

FIG. 36. Proton F_2 vs Q^2 (GeV^2) in x_{Bj} bins. The points have been multiplied by the factors indicated in parentheses for clarity. The error bars indicate the sum in quadrature of the statistical and systematic uncertainties. The normalization uncertainty is not included.

is performed by weighting each event in the data by the ratio $F_2(\log_{10}x_c,\log_{10}Q_c^2)/F_2(\log_{10}x, logQ^2)$, where F_2 is obtained from the parametrization and the subscript c denotes bin center. The bin-centering correction is small except at the lowest x, where it is about 5%, and above x of 0.1 (where the bins are wide), where it is about 10%. The systematic uncertainty is estimated by using instead a parametrization fitted to our data. The difference is negligible except at the highest and lowest x of the data. It is included in quadrature as the systematic uncertainty in the bin-centering correction. The column marked BN in Tables I–IV shows the quadrature-combined uncertainty from all the bin edge and bin-centering effects discussed above.

8. Systematic uncertainty independent of kinematics

Certain sources of error are independent of the scattering kinematics; hence, they lead to an uncertainty in the overall normalization of F_2.

The contributions from the uncertainty in measurements related to the luminosity are as follows: beam spectrometer response 0.2%, random beam prescale factor 0.15%, nominal target length 0.035%, uncertainty in target length due to target wall curvature 0.5%, and effective density for pure targets hydrogen 0.05% and deuterium 0.6%. The statistical uncertainty on the final number of random beam events is 0.34% for hydrogen and 0.53% for deuterium (following empty target subtraction). Adding in quadrature, these amount to a total uncertainty in the luminosity of 0.7% for hydrogen and 1.0% for deuterium.

The uncertainty in the trigger logic simulation is 1.3%, and it was shown that this is not sensitive to scattering kinematics. Hence we include it in the overall normalization uncertainty. Finally, the muon-match efficiency was shown to be fairly independent of momentum and position of the muon, within about 1%. We include an uncertainty of 1% from this source. Therefore the total uncertainty in the overall normalization of F_2 is 1.8% for hydrogen and 1.9% for deuterium, obtained by adding the contributions in quadrature.

D. Fitting the measured F_2

In order to fit F_2 over our kinematic range, we use a parametric function that is motivated in part by the function used by NMC [12] and in part by the parametrization of Donnachie and Landshoff [28]. We define the functions

$$A(x)=x^{a_1}(1-x)^{a_2}[a_3+a_4(1-x)+a_5(1-x)^2+a_6(1-x)^3 +a_7(1-x)^4],$$

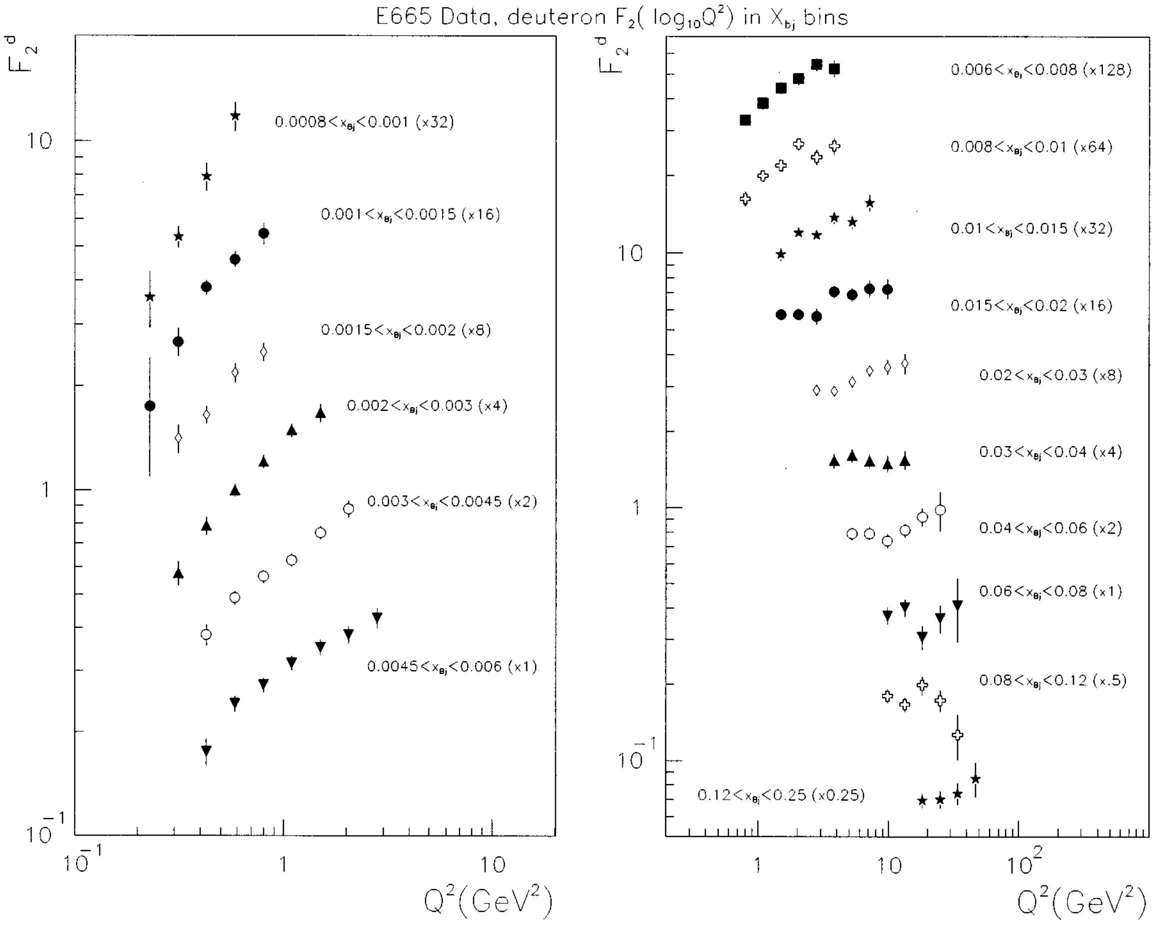

FIG. 37. Deuteron F_2 vs Q^2 (GeV^2) in x_{Bj} bins.

$$B(x)=b_1+b_2x+b_3/(x+b_4),$$

$$f_{\mathrm{hi}Q^2}=A(x)\left[\frac{\ln(Q^2/\Lambda^2)}{\ln(Q_0^2/\Lambda^2)}\right]^{B(x)},$$

$$Q_0^2=20\ \mathrm{GeV}^2,$$

$$\Lambda=250\ \mathrm{MeV},$$

$$f_{\mathrm{lo}Q^2}=c_1x^{-0.0808}\left(\frac{Q^2}{Q^2+(c_1/0.604)^{0.9252}}\right)^{1.0808}$$
$$\times[1+c_2(W-20)],$$

$$g=\frac{1}{1+e^{(Q^2-3)/1.5}},$$

$$F_2^{\mathrm{fit}}=f_{\mathrm{lo}Q^2}\times g+f_{\mathrm{hi}Q^2}\times(1-g), \tag{9.1}$$

where Q^2 is in GeV^2 and W is in GeV. The function $f_{\mathrm{hi}Q^2}$ is motivated by QCD evolution, while $f_{\mathrm{lo}Q^2}$ follows a form approaching the photoproduction limit. The function g is used to make a smooth transition with Q^2 between the two functions. Except for the c_2 term, $f_{\mathrm{lo}Q^2}$ is constrained to match the real photoproduction cross section. The c_2 term is introduced to fit the observed departure of the W dependence of the virtual photoproduction cross section from the real photoproduction cross section.

As we showed in Sec. III, the acceptance and the radiative corrections made to the raw event count to extract F_2 in fact depend on the structure function. Hence we use the results of the fit in an iterative process to force consistency between the input and the output structure function. However, we have to be careful not to extend the fit beyond the range of the data. We find that the strength of the E665 data lies at low x and low Q^2, while the high-x–high-Q^2 regime has been measured extensively by NMC and BCDMS, connecting smoothly with the high-x–low-Q^2 data from SLAC. Hence we use the parametrization of those data described in Appendix XII for $x>0.05$ and the fit to the E665 data described above for $x<0.05$. In addition, we do not measure the structure function at very low Q^2, i.e., $Q^2<0.2$ GeV^2. Hence we connect our fit smoothly with the Donnachie-Landshoff parametrization at lower Q^2 which matches the real photoproduction cross section at $Q^2=0$. Denoting the global F_2 function of Appendix XII as F_2^{global} (which includes the Donnachie-Landshoff parametrization at low Q^2 and the SLAC-NMC-BCDMS fit at high x), we use the following function in the range $x<0.05$, $W>8$ GeV to iterate the extraction of the corrections:

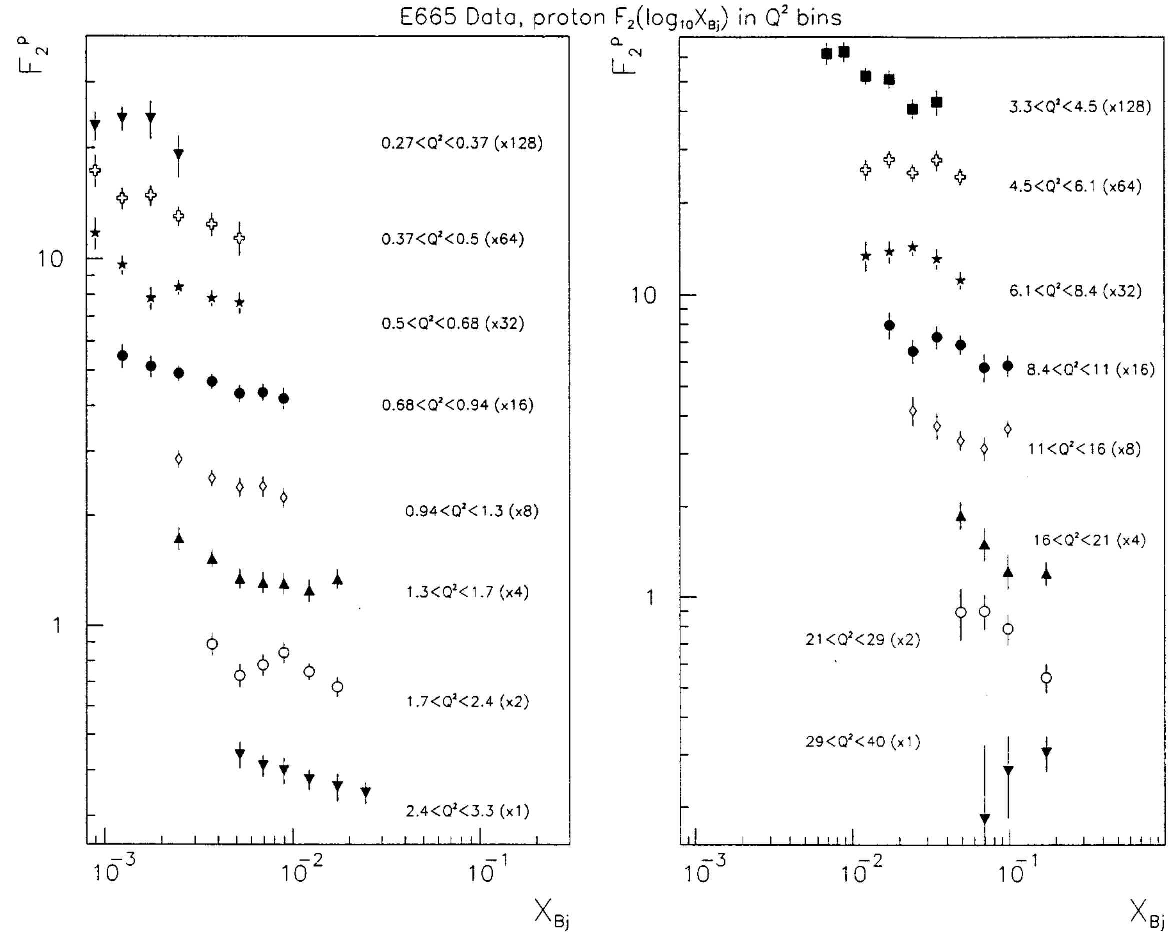

FIG. 38. Proton F_2 vs x_{Bj} in Q^2 (GeV^2) bins.

$$F_2^{\text{iterate}} = F_2^{\text{fit}}\Theta(\log_{10}Q^2+1.0)+[1-\Theta(\log_{10}Q^2+1.0)] \times\left[F_2^{\text{global}}+\frac{F_2^{\text{fit}}-F_2^{\text{global}}}{(\log_{10}Q^2)^2}\right], \tag{9.2}$$

where Θ is the step function which is unity when the argument is positive and zero when it is negative. Outside the range $x<0.05$, $W>8$ GeV, we maintain the use of F_2^{global}. This new F_2 is used to recalculate the radiative corrections and reweight the events in the Monte Carlo simulation used to calculate the acceptance corrections. Since the F_2^{global} function roughly describes our data, the typical change in the measured F_2 after the first iteration is only about 1%. After four iterations the change in F_2 is less than 0.05%, and we stop iterating. It should be mentioned that the variables used in this context for the Monte Carlo reweighting are the hadronic variables; i.e., they describe the kinematics of the true single virtual photon that interacts with the nucleon. They do not agree with the kinematics at the muon vertex in the case that a real radiative photon is emitted.

The fit is performed after all systematic effects have been investigated. The error on each point used in the fit is the quadrature sum of the statistical error from the data, the statistical error on the Monte Carlo correction, and the kinematics-dependent systematic uncertainty. The uncertainty in the overall normalization is not included. The fitted parameters and their respective errors are given below in Table V. It should be noted that the errors on some of these parameters are correlated. For each target there are 91 data points. The fit to the proton F_2 gives $\chi^2/N_{\text{DF}}=0.88$, while the fit to the deuteron F_2 gives $\chi^2/N_{\text{DF}}=0.93$.

E. Final data and Monte Carlo simulation comparisons

The Monte Carlo simulation obtained after the final iteration is used to make comparisons of inclusive distributions with the data. All the analysis cuts made for the F_2 measurement are made both on the data and the Monte Carlo simulation. The inclusive distributions are self-normalized (i.e., integrate to unity) before the comparison. The distributions from the data and the Monte Carlo simulation are superposed on the left side in Figs. 33, 34, and 35, and the corresponding data/MC ratio is shown on the right side. The distributions agree to within 10% or better over most of the kinematic range.

F. Results

The results on the structure function F_2 are given in Tables VI and VII for the proton and the deuteron. The statistical and kinematics-dependent systematic uncertainties are quoted in percent of F_2. The systematic uncertainty is the quadrature sum of the seven different uncertainties quoted in

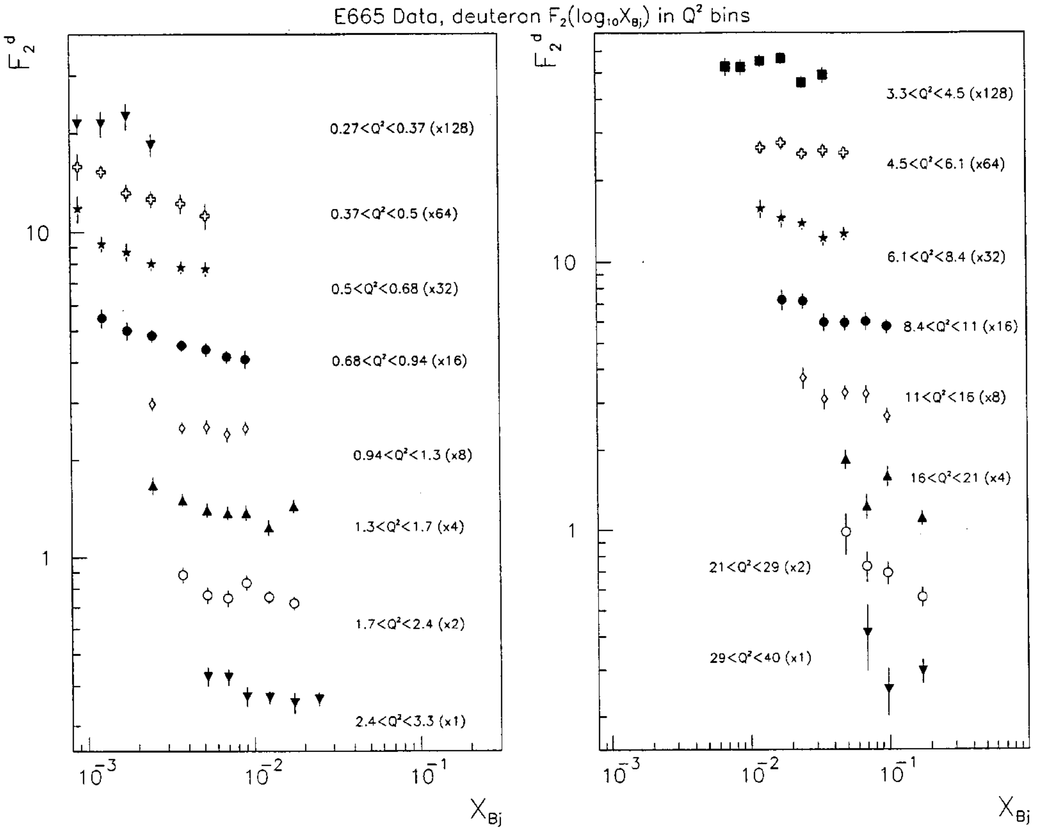

FIG. 39. Deuteron F_2 vs $x_{\rm Bj}$ in Q^2 (GeV^2) bins.

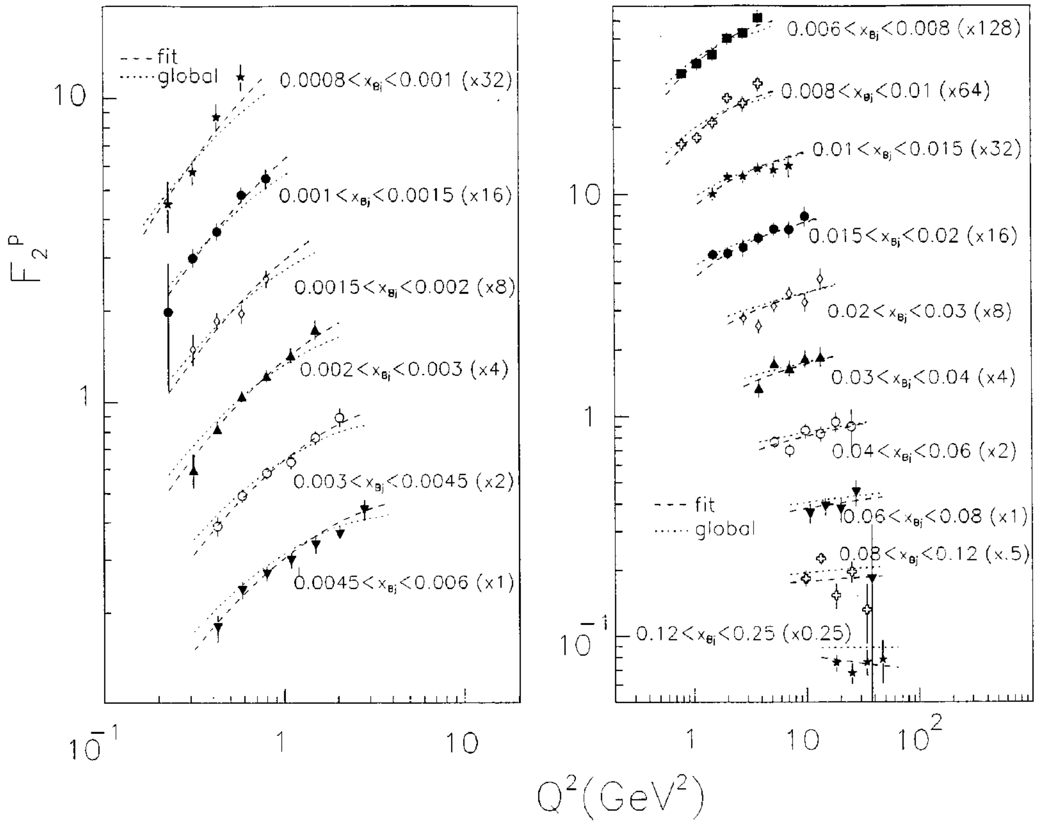

FIG. 40. Proton F_2 vs Q^2 (GeV^2) in $x_{\rm Bj}$ bins, with curves showing the fit to the data and the global F_2 parametrization (Appendix XII).

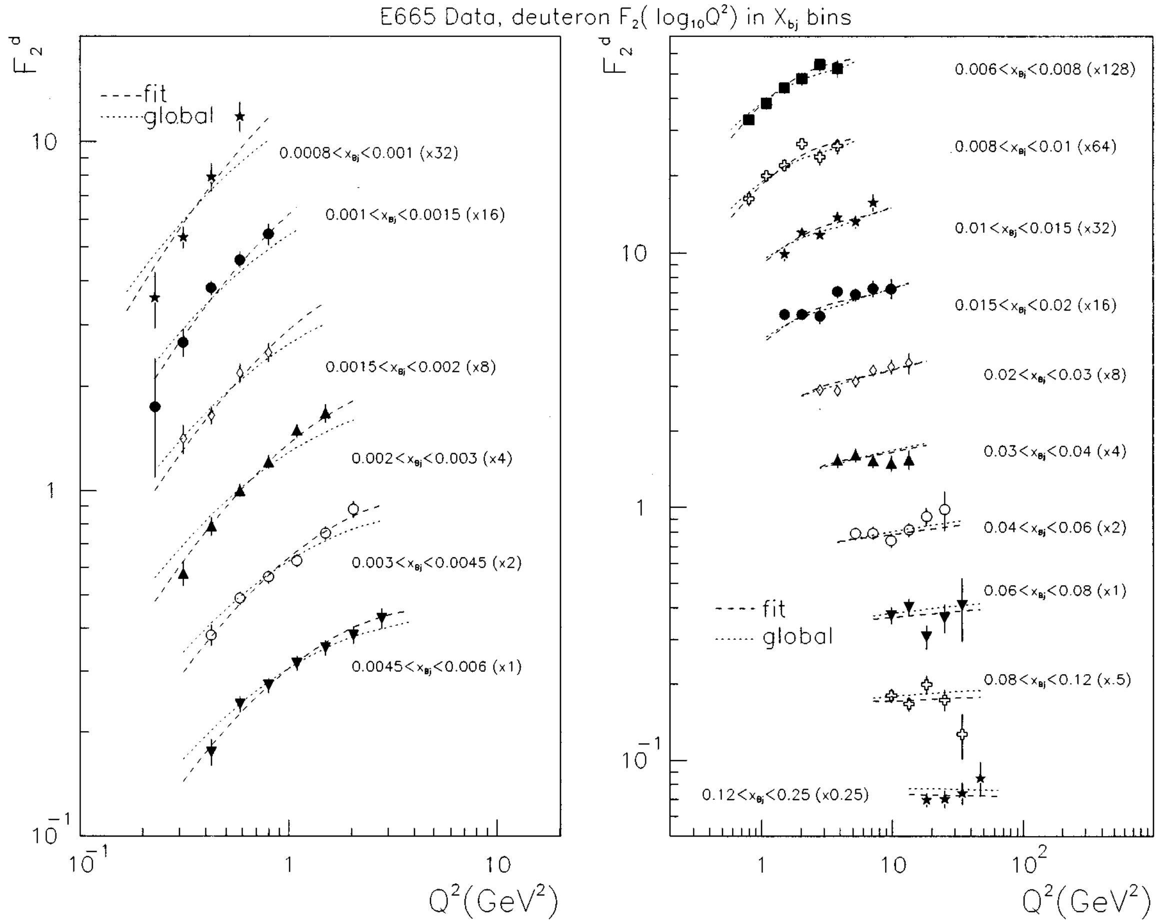

FIG. 41. Deuteron F_2 vs Q^2 (GeV^2) in $x_{\rm Bj}$ bins, with curves showing the fit to the data and the global F_2 parametrization.

Tables I–IV for each bin. The overall normalization uncertainty discussed in Sec. IX C 8 is not included in the quoted systematic uncertainty.

Tables VIII and IX show the total acceptance for the muon cross section computed for each bin from the Monte Carlo simulation. The statistical uncertainty in the computed acceptance, due to the Monte Carlo statistics, is also given in percent of the acceptance. The statistical uncertainty in the acceptance correction is included in quadrature with the statistical uncertainty in the data, in the quoted statistical error on F_2. The bin acceptance, denoted by ϵ in Eq. (3.5), includes all the detector-related effects affecting the measurement of the total muon cross section. These include the trigger and reconstruction efficiencies as well as the multiple scattering and resolution smearing effects indicated in Fig. 3.

The structure function F_2 is plotted against Q^2 in x bins in Figs. 36 and 37. In these and all subsequent plots of E665 and other data, the error bars represent the quadrature sum of the statistical and systematic uncertainties. However, the overall normalization uncertainty will not be included in any of the errors shown. Figures 38 and 39 show F_2 plotted against x in Q^2 bins. In Figs. 40–43, the data are compared with the global F_2 parametrization (dotted lines), as well as with the fit described in Sec. IX D (dashed lines). While the F_2 parametrization gives a good qualitative description of the data at low x and Q^2, the fit gives a better description of the slope of F_2 with respect to Q^2 at fixed x and the slope of F_2 with respect to x at fixed Q^2.

The logarithmic derivative of F_2 with respect to Q^2 at fixed x ($\partial \ln F_2/\partial \ln Q^2$) is plotted vs x in Fig. 44. Also shown in Fig. 44 is the value of the slope of 1.0808 in the photoproduction limit, extracted from the high energy behavior of the real photoproduction cross section (see discussion in [28]).

The logarithmic derivative $\partial \ln F_2/\partial \ln x$ at fixed Q^2 is shown in Fig. 45. The high energy photoproduction limit derived from the Donnachie-Landshoff model is shown, as is the typical slope of ~ -0.3 derived [65] from the high Q^2 HERA data ($F_2 \sim x^{-0.3}$).

In this analysis the proton and deuteron structure functions are measured separately. We use linear fits similar to those shown in Figs. 10.12–12.17 of [48] to extract the value of the proton and deuteron F_2 at the central Q^2 in each x bin. The deuteron-to-proton structure function ratio extracted in this way is shown as a function of x by the stars in Fig. 46. An independent analysis of the E665 data has been performed [53,66] with the goal of measuring the deuteron-to-proton structure function ratio directly, by exploiting the cancellation of acceptance corrections. The results on the ratio from the ''direct'' analysis [53,66] are also shown in Fig. 46 (circles). Within the uncertainties, the results on F_2^d/F_2^p from

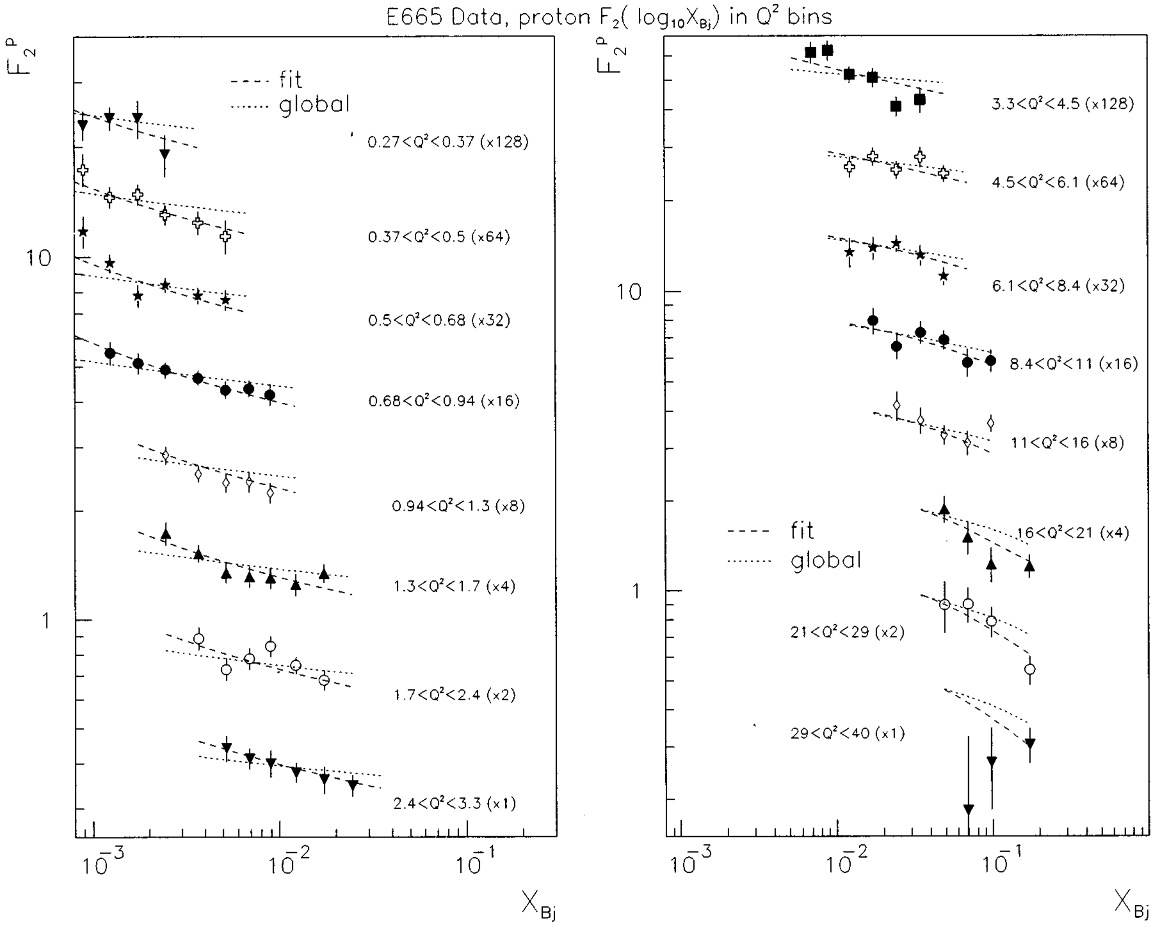

FIG. 42. Proton F_2 vs x_{Bj} in Q^2 (GeV^2) bins, with curves showing the fit to the data and the global F_2 parametrization.

the two analyses are in good agreement. The ''direct'' analysis uses the data from the calorimeter trigger in addition to the SAT to extend the range of the F_2^d/F_2^p measurement to lower x.

X. COMPARISONS AND CONCLUSIONS

In this section we compare our structure function results with measurements from other experiments and with theoretical models. The structure function F_2 can be analyzed using the perturbative QCD formalism at high Q^2 or in terms of the nonperturbative hadronic photon picture which is usually applied at low Q^2. We will briefly review some of the current models that use these techniques and compare them with the data. We will also compare the data with the F_2 results from NMC and HERA.

A. Comparisons with other experiments

The high Q^2, large x range of the E665 data overlaps with the NMC structure function measurements [67]. The comparison between the two measurements is shown in Figs. 47 and 48. The two measurements are in good agreement. Note that this region of overlap is the x range where there is currently a disagreement between the NMC values of F_2 and the nuclear-effect-corrected values from the CCFR neutrino experiment. The E665 data also overlap significantly with the HERA data in x, though the HERA data are at higher Q^2. In Figs. 49 and 50 we show the E665 data with the ZEUS data [68] and the H1 data [69], respectively, as a function of Q^2 in bins of x. Not all the E665 data are shown; only those E665 x bins which contain the corresponding x value of the HERA data are shown. In one plot the different x bins are scaled by powers of 10 for clarity; in the other plot the data in the different x bins are shown without any scale factors. The same symbols are used for the different x bins in the two plots. We see that the two experiments together cover a very large dynamic range in x and Q^2. In each x bin we expect a smooth connection in Q^2 between the two data sets. We have superimposed F_2 model calculations from Badełek and Kwieciński (discussed below) to guide the eye in this regard. We see that the two data sets do indeed connect with each other quite smoothly as a function of Q^2.

The comparison with the HERA data shows the pattern of F_2 scaling and scaling violations over a very large range of x and Q^2. It also shows that the x dependence of F_2 is different at low and high Q^2. The rise in F_2 with decreasing x is weaker in the lower Q^2 E665 data than it is in the higher Q^2 HERA data. This difference is quantified in Fig. 45 which shows the logarithmic derivative of F_2 with respect to x. The transition in the x dependence (i.e., W dependence) at fixed Q^2 appears to start near $Q^2=10$ GeV^2, in the E665 data.

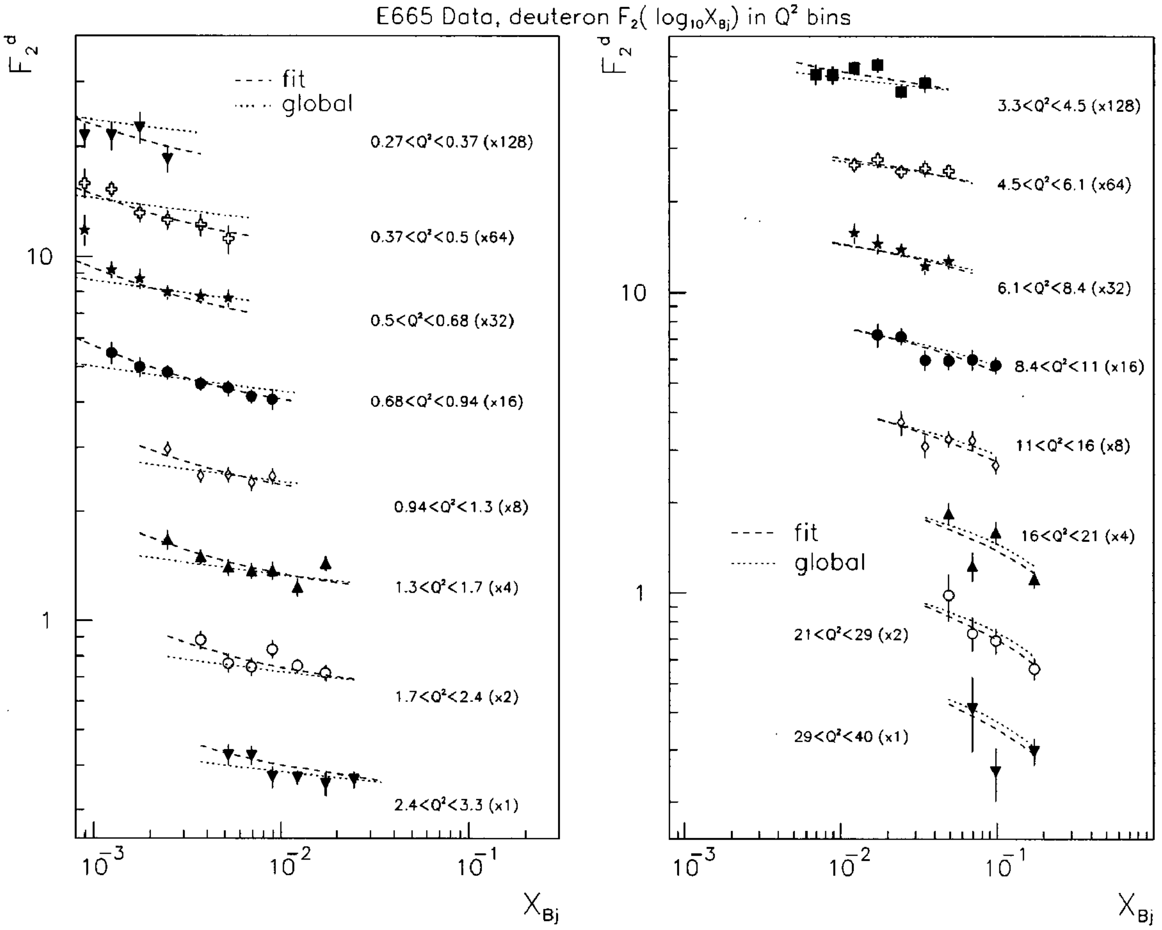

FIG. 43. Deuteron F_2 vs x_{Bj} in Q^2 (GeV^2) bins, with curves showing the fit to the data and the global F_2 parametrization.

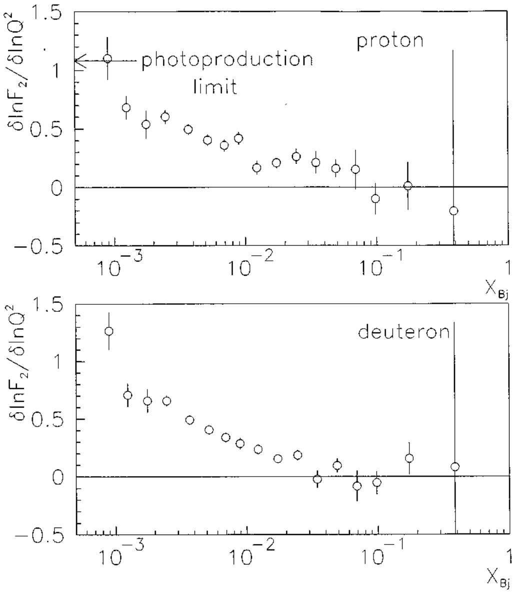

FIG. 44. Logarithmic derivative of F_2 with respect to Q^2 ($\partial \ln F_2 / \partial \ln Q^2$) at fixed x, shown vs x for protons and deuterons. The photoproduction limit [28] derived from real photon-proton cross-section measurements is also shown.

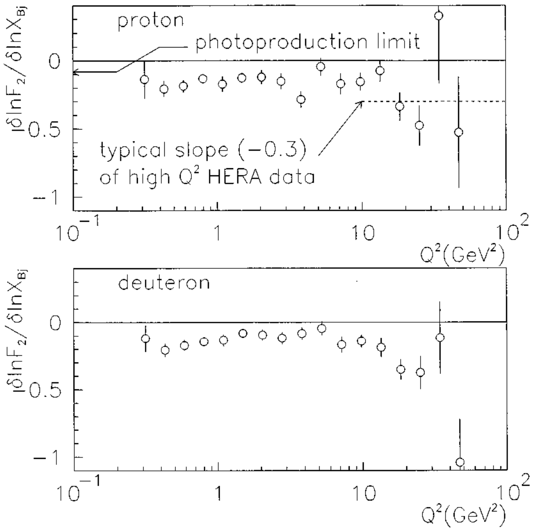

FIG. 45. Logarithmic derivative of F_2 with respect to x ($\partial \ln F_2 / \partial \ln x$) at fixed Q^2, shown vs Q^2 for protons and deuterons. The photoproduction limit [28] derived from real photon-proton cross-section measurements is also shown, and the typical slope [65] measured with the high Q^2 HERA data is indicated.

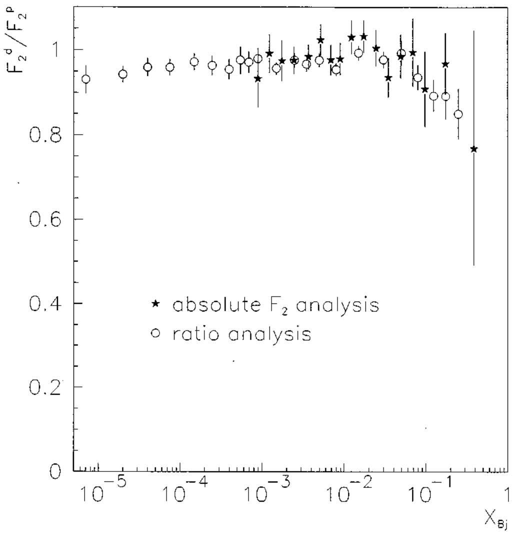

FIG. 46. The deuteron-to-proton structure function ratio, measured by taking the ratio of the absolute structure functions in this analysis (stars) and by an independent ‘‘direct’’ analysis [66] of the ratio (circles).

B. QCD-evolved leading twist structure functions

The QCD radiation from quarks and gluons causes the apparent quark and gluon density, and hence the structure functions, to change with the momentum scale of the photon. At high Q^2, where the ‘‘higher twist’’ effects are expected to be small, the photon dominantly is absorbed by individual partons. The accompanying QCD radiative effects can be calculated in field theory. Hence an analysis of the structure function data based on QCD evolution can be used to obtain a set of universal parton distributions. The usefulness of these universal parton distributions is that they can then be used to calculate any hard scattering cross section.

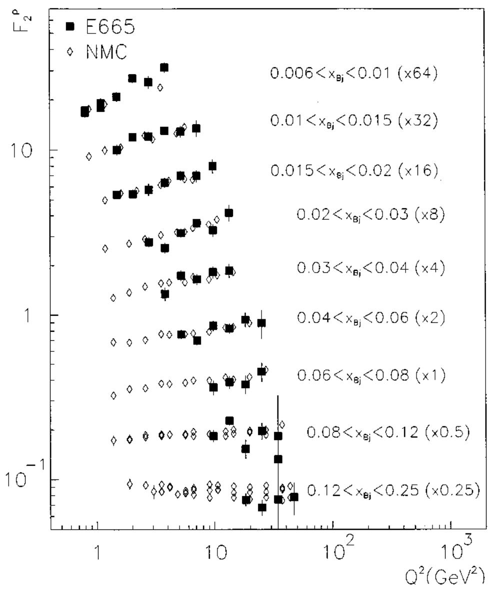

FIG. 47. Proton F_2 from E665 and NMC [67] overplotted vs Q^2 in x bins. In certain x bins one of the two experiments has multiple data points because the actual binning in x is narrower. In these cases all the data points falling in those bins are shown. The points have been multiplied by the factors indicated in parentheses for clarity.

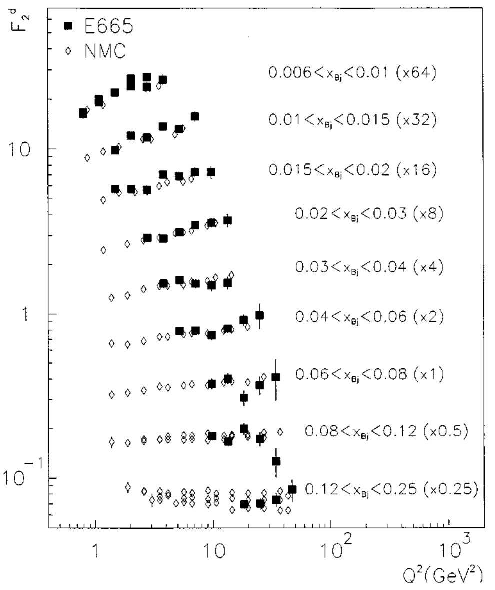

FIG. 48. Deuteron F_2 from E665 and NMC [67] overplotted vs Q^2 in x bins. In certain x bins one of the two experiments has multiple data points because the actual binning in x is narrower. In these cases all the data points falling in those bins are shown.

We compare the data with the F_2 model of Glück, Reya, and Vogt (GRV) which performs QCD evolution up from a low momentum scale ($\mu_0^2=0.3$ GeV^2). This model uses an *ansatz* that the parton distributions have valencelike behavior (approach zero as $x\rightarrow 0$) at the low momentum scale. It is based on next-to-leading order (NLO) QCD calculations with no higher twist contributions (leading twist, i.e., twist 2 only). In the Figs. 51, 52, 53, and 54, the measured F_2 is compared with the F_2 calculated from the GRV model [70]. The GRV calculation breaks down below $Q^2=0.3$ GeV^2; hence, we do not show the calculation below this scale.

The comparison shows that the shape of the structure function at high Q^2 can be explained through the QCD evolution of the leading twist (twist-2) component alone. The GRV F_2 has been able to reproduce the rise in the structure function with reducing x as seen in the high Q^2 HERA data. It is in fair agreement with the high Q^2 E665 data. What is perhaps more surprising is that the GRV F_2 is able to describe the E665 data for Q^2 as low as 0.7 GeV^2 and x as low as 0.003, before the agreement breaks down.

C. Low Q^2 structure functions

We will now discuss two models or fits that explicitly attempt to describe the structure function at low Q^2. These models typically combine information from the high Q^2 perturbative region and low Q^2 phenomenology to describe the transition to low Q^2. They are the Donnachie-Landshoff model and the Badełek-Kwieciński model.

The Donnachie-Landshoff model [28] is a phenomenological interpolation between the real photoproduction data and the data in the perturbative region of Q^2. This F_2 model is incorporated in the form

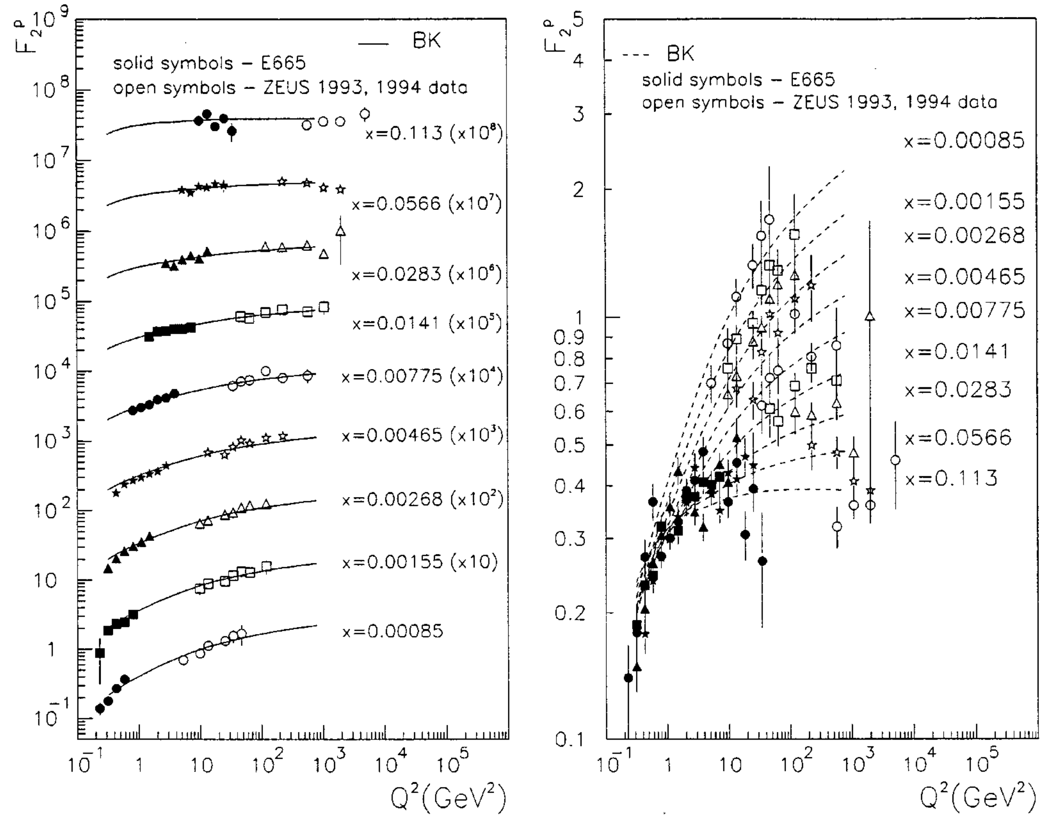

FIG. 49. Proton F_2 vs Q^2 (GeV^2) in $x_{\rm Bj}$ bins, from E665 and ZEUS [68]. The Badełek-Kwieciński (BK) model is also shown. (left) The data points and the model curves have been multiplied by the factors indicated in parentheses for clarity. (right) The points and curves are plotted with no scale factors, to show the trends.

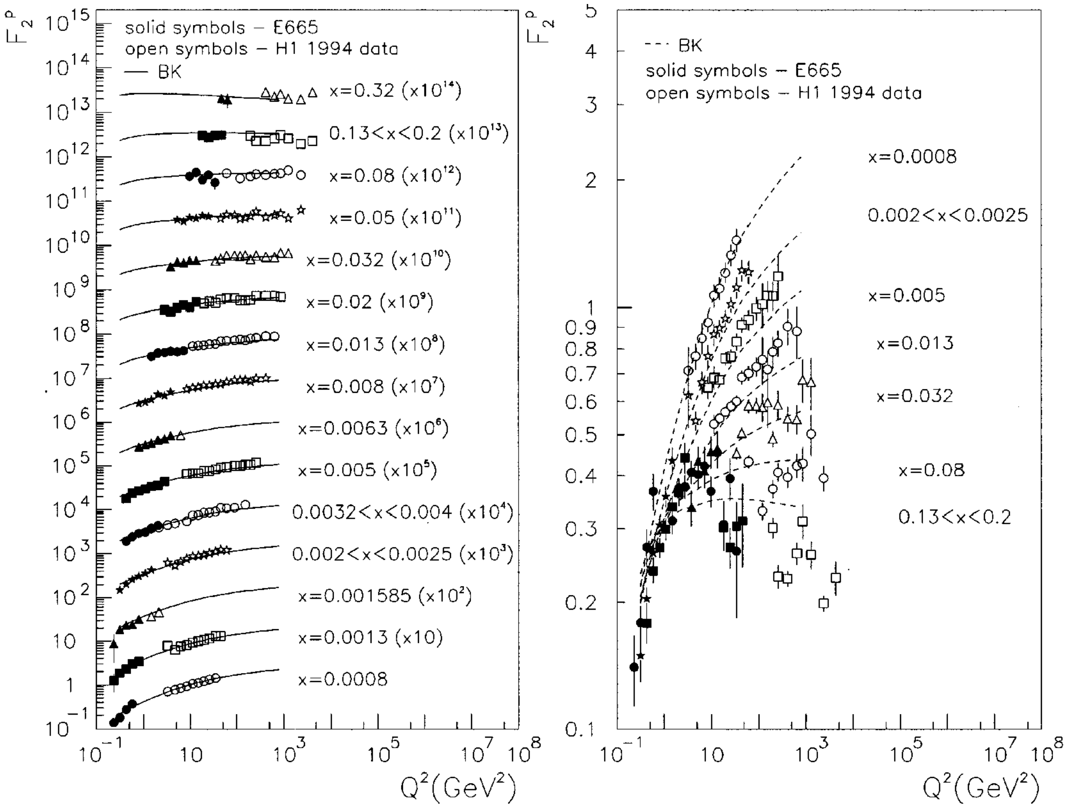

FIG. 50. Proton F_2 vs Q^2 (GeV^2) in $x_{\rm Bj}$ bins, from E665 and H1 [69]. The Badełek-Kwieciński (BK) model is also shown. (left) The data points and the model curves have been multiplied by the factors indicated in parentheses for clarity. (right) The points and curves are plotted with no scale factors, to show the trends.

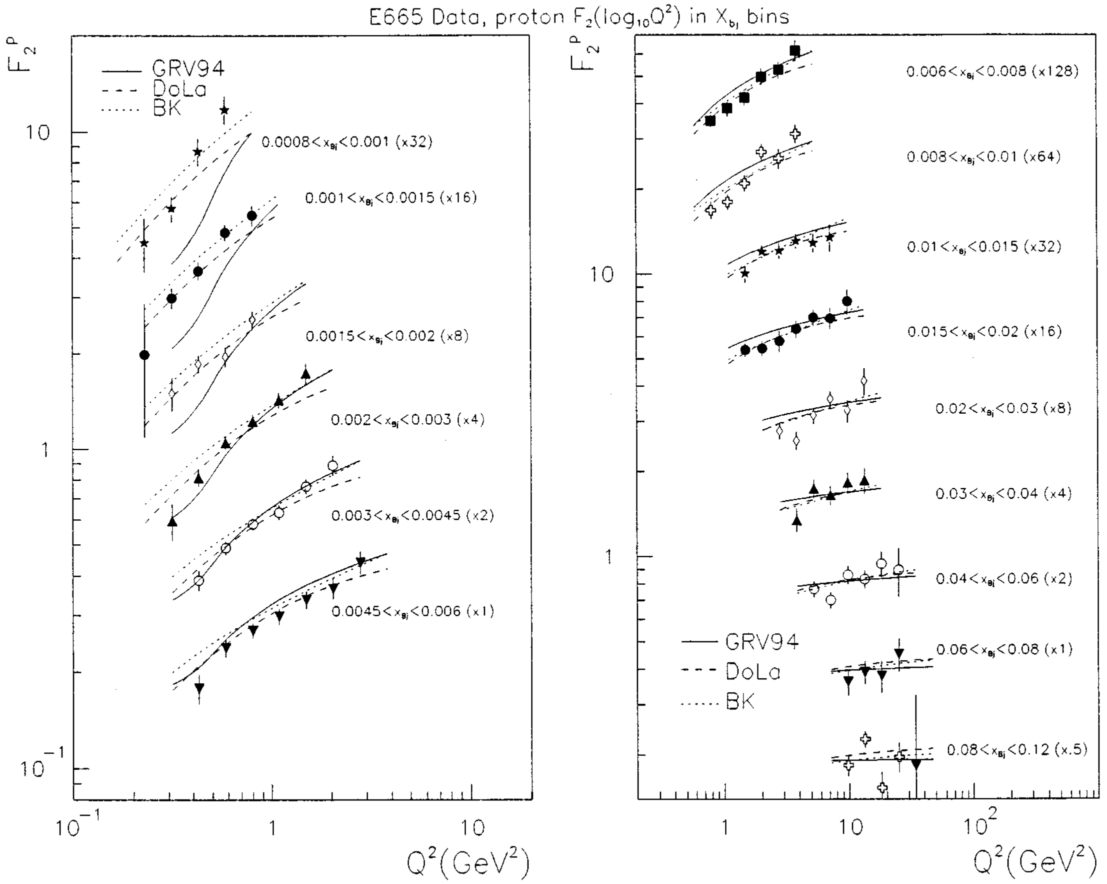

FIG. 51. Proton F_2 vs Q^2 (GeV^2) in x_{Bj} bins, with curves showing the calculation of Glück, Reya, and Vogt (1994), Donnachie and Landshoff, and Badełek and Kwieciński.

$$F_2 = 0.324x^{-0.0808}\left(\frac{Q^2}{Q^2+a}\right)^{1.0808} + 0.098x^{0.4525}\left(\frac{Q^2}{Q^2+b}\right)^{0.5475}. \tag{10.1}$$

The authors have also incorporated the additional contribution of heavy flavors and invoking counting-rule arguments to describe the large x behavior. In the following comparisons with our data we compute the Donnachie-Landshoff F_2 in its full form with the FORTRAN code obtained from [28]. This model has the correct photoproduction limit because the real photoproduction data are included in the fit.

The Badełek-Kwieciński model [71] is based on the idea of generalized vector meson dominance (GVMD). In the Badełek-Kwieciński model, the sum over all the hadronic fluctuations of the photon is split into two pieces:

$$F_2 = F_2^{(v)} + F_2^{(p)}. \tag{10.2}$$

$F_2^{(v)}$ denotes the contribution from the low mass vector mesons ρ, ω, and ϕ. Since this contribution vanishes at high Q^2, the measured structure function at high Q^2 must be due to the contribution of the high mass states beyond the ϕ. The contribution of the high mass states is represented by $F_2^{(p)}$ and is obtained from the conventional QCD-evolved parton distributions by using dispersion relations. The authors have simplified the dispersion relations to obtain a simple expression for $F_2^{(p)}$ in terms of the high Q^2 asymptotic structure function F_2^{as}:

$$F_2^{(p)}(s,Q^2) = \frac{Q^2}{Q^2+Q_0^2} F_2^{\mathrm{as}}(s,Q^2+Q_0^2). \tag{10.3}$$

$F_2^{(p)}$ represents the contribution of vector meson states heavier than Q_0. By choosing Q_0 to be greater than the mass of the heaviest vector meson included in $F_2^{(v)}$, double counting is avoided.

It is evident that $F_2 \rightarrow F_2^{\mathrm{as}}$ for large Q^2. As Q^2 reduces the model makes a smooth transition by combining the nonperturbative contribution of the low mass vector mesons and the residual contribution of the high mass states. The singularities in F_2 at low Q^2 are removed by the shift of the variable $Q^2 \rightarrow Q^2 + Q_0^2$. At very low Q^2 the model approaches the photoproduction limit, describing the shape of $\sigma_{\gamma p}(s)$ but overestimating its magnitude by about 10–15 %.

In the Badełek-Kwieciński model the proton and neutron structure functions are calculated separately. Shadowing in the deuteron is calculated explicitly [72]. The deuteron structure function is defined as the sum of the proton and neutron structure functions, and the shadowing contribution. The calculated shadowing contribution is negative and varies between ~ 0.001 and 0.006 in absolute magnitude.

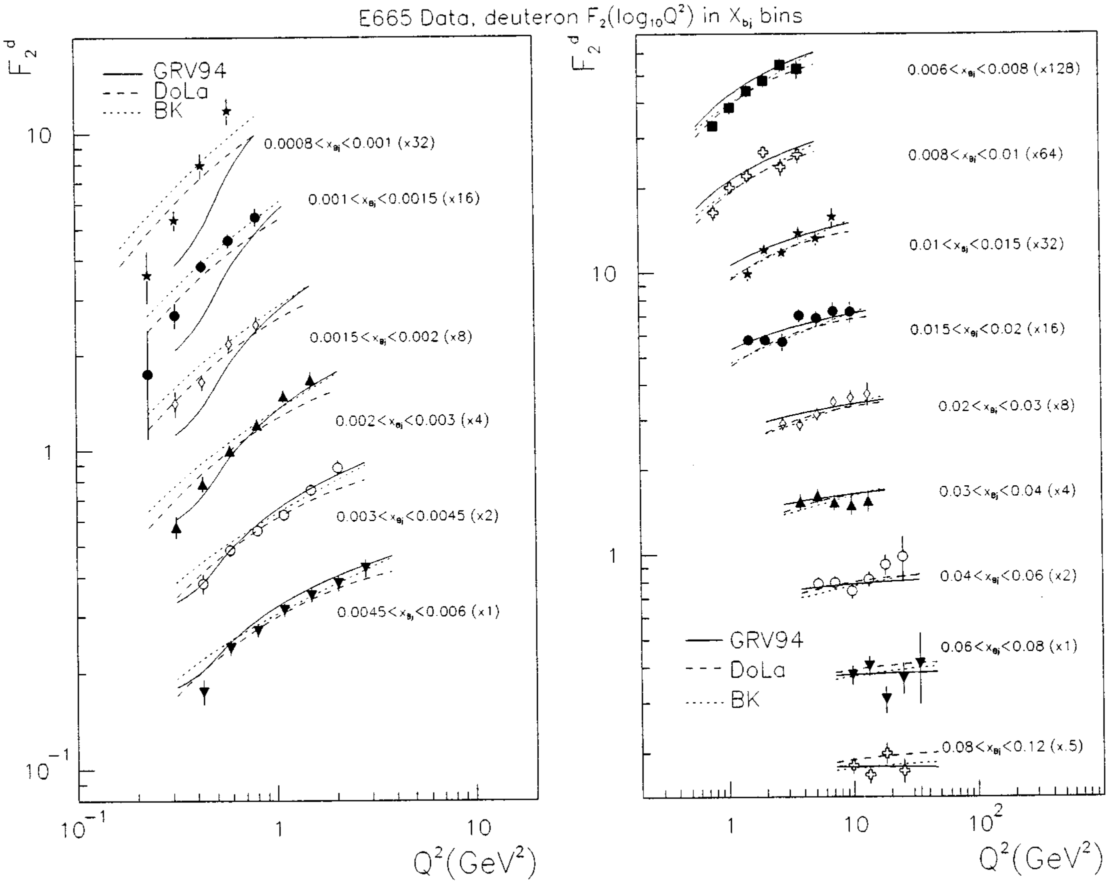

FIG. 52. Deuteron F_2 vs Q^2 (GeV^2) in x_{Bj} bins, with curves showing the calculation of Glück, Reya, and Vogt (1994), Donnachie and Landshoff, and Badełek and Kwieciński.

We calculate the Badełek-Kwieciński model F_2 for the proton and the deuteron using Fortran code obtained from [71] and [72]. In this version the high Q^2 asymptotic structure functions F_2^{as} are obtained from the MRS(A) set of parton distributions.

We compare these low Q^2 models or fits with our F_2 data in Figs. 51, 52, 53, and 54. We find that both models are able to describe the data at high Q^2 and x since the models are constrained by previous data. At low Q^2 and x the models are qualitatively similar to the data, but the data are sufficiently precise that we may note quantitative differences. The Badełek-Kwieciński curves tend to overshoot the data at low Q^2 and x, which may be due to the fact that this model overestimates the real photoproduction cross section by 10–15 % as mentioned above. The Donnachie-Landshoff model is able to describe the average value of F_2 in a bin of x or Q^2. However, the slope of the data with respect to x or Q^2 is steeper than that predicted by either the Donnachie-Landshoff or the Badełek-Kwieciński models. As one can see from the definition of the variables, the slope of F_2 with respect to x at fixed Q^2 and the slope of F_2 with respect to Q^2 at fixed x both reflect the slope of F_2 with respect to W^2. The W^2 dependence of F_2 at low Q^2 is derived in both models from the observed W^2 dependence of the real photon-nucleon and hadron-nucleon cross sections, which are similar (see [28] for a discussion). Thus the data suggest that the W dependence of the virtual photon-nucleon cross section is stronger than the W dependence of the real photon-nucleon cross section.

In Fig. 55 we show the logarithmic derivative of F_2 with respect to Q^2 ($\partial \ln F_2 / \partial \ln Q^2$) vs x, compared with the same quantity from the Donnachie-Landshoff model. While the model qualitatively reproduces the trend that the slope increases as x decreases, the data tend to lie above the model prediction. We have already seen in Fig. 45 that the logarithmic slope of F_2 with x ($\partial \ln F_2 / \partial \ln x$) is more negative in the data than the value expected in the photoproduction limit from the Donnachie-Landshoff model. These comparisons show more clearly the tendency that the W dependence at low Q^2 in our data is stronger than the W dependence expected in the photoproduction limit. The significance of the c_2 term in the fit to our data (see Sec. IX D) shows this effect. At the same time the W dependence at low Q^2 is weaker than at high Q^2 as seen from HERA data.

The Q^2 dependence at fixed W also shows a transition from high to low Q^2. In Figs. 56 and 57, we show the virtual photon-nucleon cross section computed from F_2 [see Eq. (3.16)] using the Hand convention [73] for the virtual photon flux [$K=(W^2-M^2)/2M$]. The same quantity computed from the Donnachie-Landshoff model is overplotted to guide the eye. At each value of W the model has been constructed to approach the real photoproduction cross section as Q^2

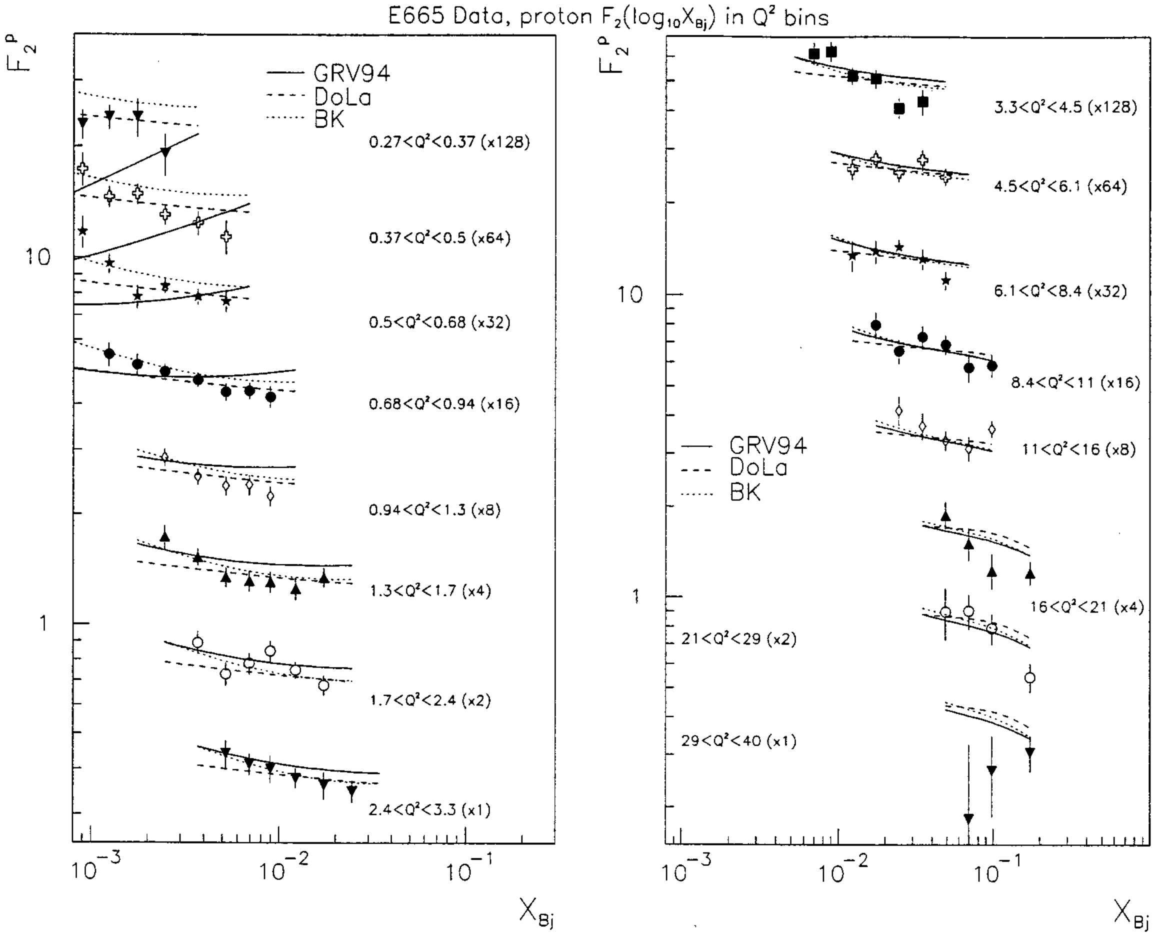

FIG. 53. Proton F_2 vs x_{Bj} in Q^2 (GeV^2) bins, with curves showing the calculation of Glück, Reya, and Vogt (1994), Donnachie and Landshoff, and Badełek and Kwieciński.

approaches zero. The data show a smooth transition in $\sigma_{\gamma^* N}$ as a function of Q^2, showing how the photon varies between a pointlike probe at high Q^2 and a hadronic object at low Q^2. The W dependence at fixed Q^2 is shown in Figs. 58 and 59.

D. Conclusions

We have presented measurements of the proton and deuteron structure functions F_2 in the kinematic range $x > 0.0008$ and $Q^2 > 0.2$ GeV^2. These are the first precise measurements of F_2 at such low x and Q^2. The data were obtained using a muon beam of the average energy 470 GeV and liquid hydrogen and deuterium targets at the experiment E665 during 1991–1992 at Fermilab.

The E665 measurements have a significant overlap in x and Q^2 with the measurements from NMC. In the region of overlap the two measurements are in good agreement. The E665 measurements also overlap in x with the HERA data, the E665 data being at lower Q^2 at fixed x. There is a smooth connection in Q^2 over a very large range between the two data sets.

The E665 data clearly show a transition in the nature of the photon-nucleon interaction when $Q^2 \sim 0.5$ GeV^2. While perturbative QCD evolution-based models give a good description of the data at higher Q^2, they fail to describe the data at lower Q^2. Thus the data can be used to quantify the higher twist effects as a function of x and Q^2. Models that incorporate the hadronic nature of the photon at low Q^2 are able to describe qualitatively the W and Q^2 dependence of the data. We find that at low Q^2, the W dependence of our data is stronger than that of real photoproduction and hadroproduction cross sections, but weaker than the W dependence of the high Q^2 HERA data. Thus the data provide a measurement of the transition between high and low Q^2 in both the W and the Q^2 dependence of the photon-nucleon interaction mechanism.

ACKNOWLEDGMENTS

This work was performed at the Fermi National Accelerator Laboratory, which is operated by Universities Research Association, Inc., under Contract No. DE-AC02-76CHO3000 with the U.S. Department of Energy. The work of the University of California, San Diego was supported in part by the National Science Foundation, Contracts Nos. PHY82-05900, PHY85-11584, and PHY88-10221; the University of Illinois at Chicago by NSF Contract No.PHY88-11164; and the University of Washington by NSF Contracts Nos. PHY83-13347 and PHY86-13003. The University of Washington was also supported by the U.S. Department of Energy. The work of Argonne National Laboratory was sup-

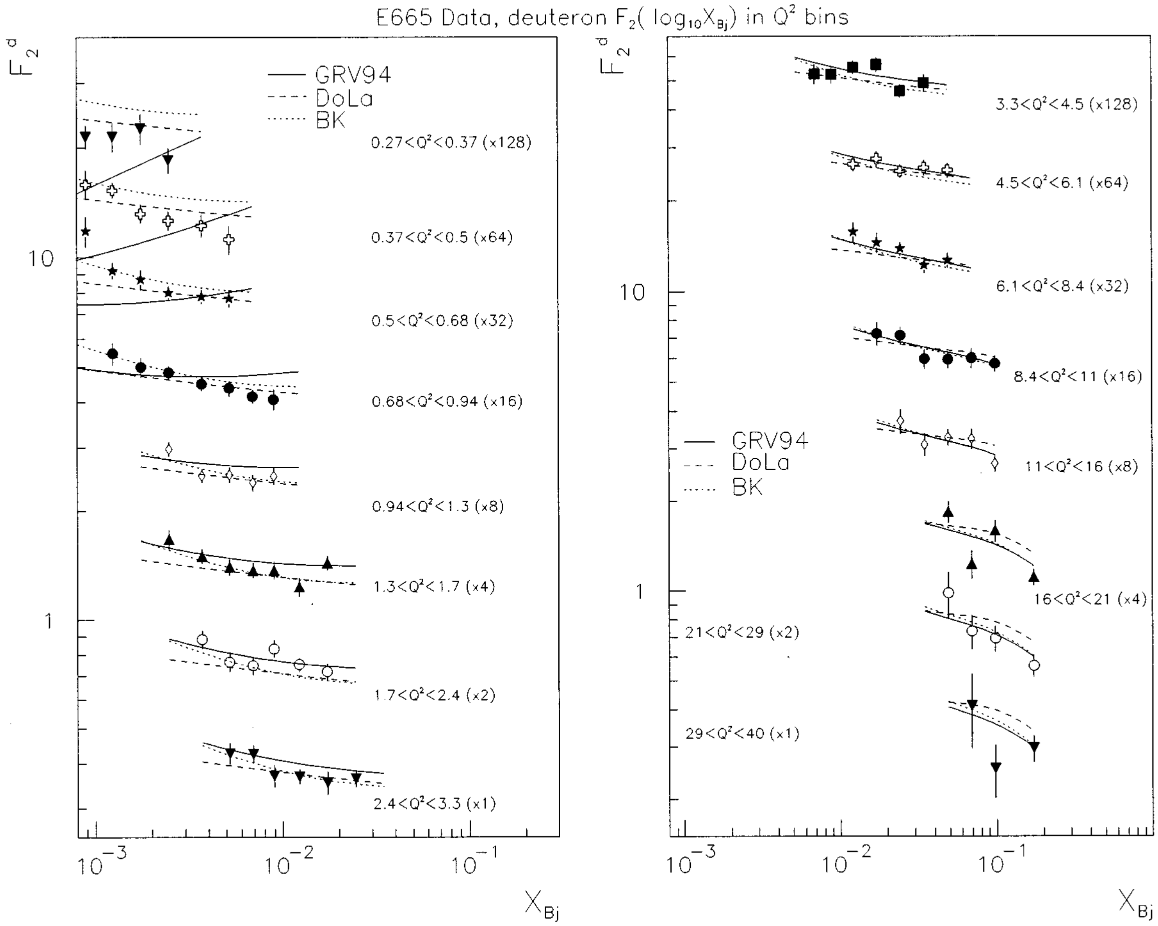

FIG. 54. Deuteron F_2 vs x_{Bj} in Q^2 (GeV^2) bins, with curves showing the calculation of Glück, Reya, and Vogt (1994), Donnachie and Landshoff, and Badełek and Kwieciński.

ported by the Department of Energy, Nuclear Physics Division, under Contract No. W-31-109-ENG-38. The Department of Energy, High Energy Physics Division, supported the work of Harvard University, the University of Maryland, the Massachusetts Institute of Technology under Contract No. DE-AC02-76ER03069, and Northwestern University under Contract No. DE-FG02-91ER40684. Northwestern University also received support from the A.P. Sloan Foundation and AT&T. The Albert-Ludwigs-Universität Freiburg and the University of Wuppertal were supported in part by the Bundesministerium für Forschung und Technologie. The work of the Institute of Nuclear Physics, Krakow, was supported by the Polish KBN Grant No. 2P03B23008.

APPENDIX: CONSTRUCTING A TRIAL F_2 PARAMETRIZATION

In order to make corrections for radiative and resolution smearing effects, it is necessary to have an approximate ‘‘trial’’ parametrization of the structure functions valid for all Q^2 and W in which we are interested. In this appendix we describe the construction of such a parametrization.

In the single-photon-exchange approximation, there are two independent variables describing the four-momentum of the virtual photon. We choose the two combinations Q^2 and

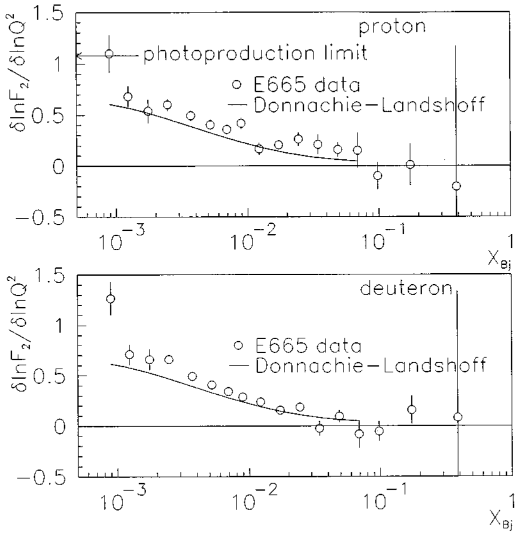

FIG. 55. Logarithmic derivative of F_2 with respect to Q^2 at fixed x, shown vs x for protons and deuterons. The photoproduction limit [28] derived from real photon-proton cross-section measurements is also shown. The data are compared with the Donnachie-Landshoff model.

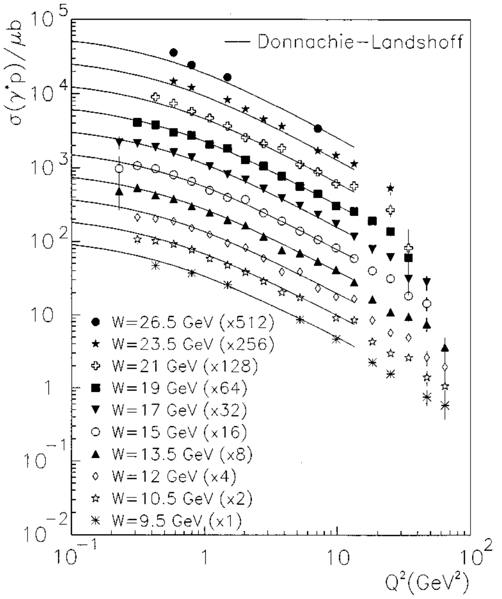

FIG. 56. Q^2 dependence of the virtual photoabsorption cross section for protons in W bins, compared with the Donnachie-Landshoff model.

W. The Q^2-W plane can be divided into the following regions: elastic, resonance, low W inelastic, and high W inelastic regions. We will discuss each of these regions in turn.

A. Elastic scattering

The elastic form factors are built into computer codes such as GAMRAD [31] and FERRAD [25] that calculate the radiative cross section. Therefore we do not need to include the elastic form factors in the parametrization of the structure function.

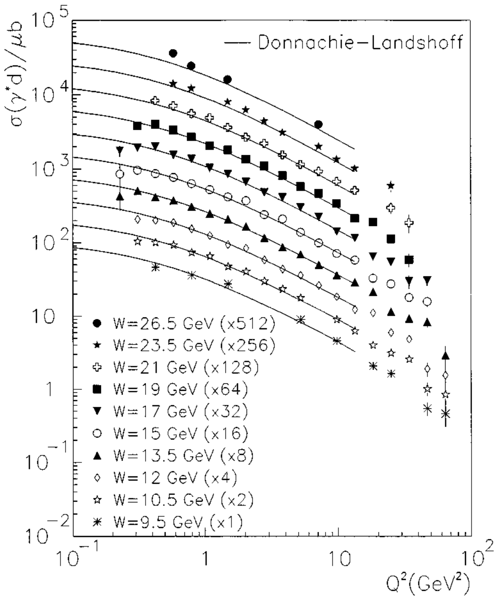

FIG. 57. Q^2 dependence of the virtual photoabsorption cross section for deuterons in W bins, compared with the Donnachie-Landshoff model.

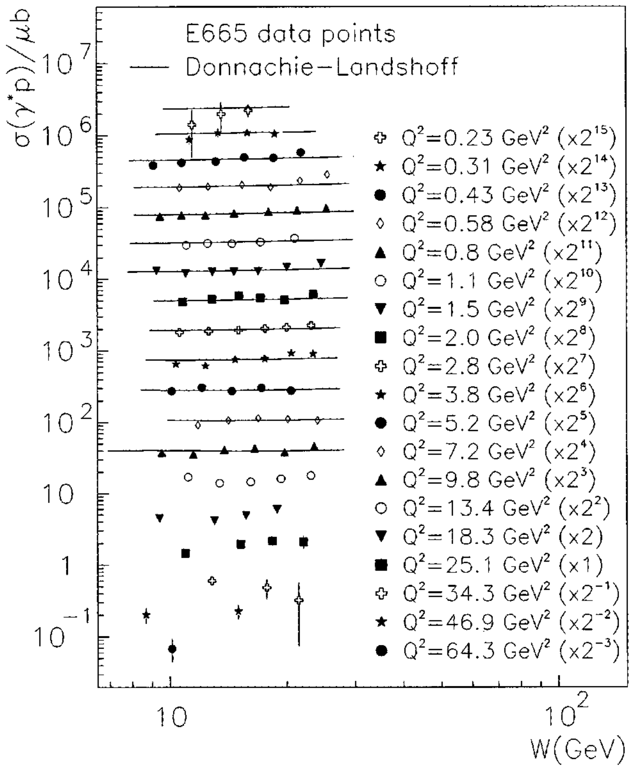

FIG. 58. W dependence of the virtual photoabsorption cross section for protons in Q^2 bins, compared with the Donnachie-Landshoff model.

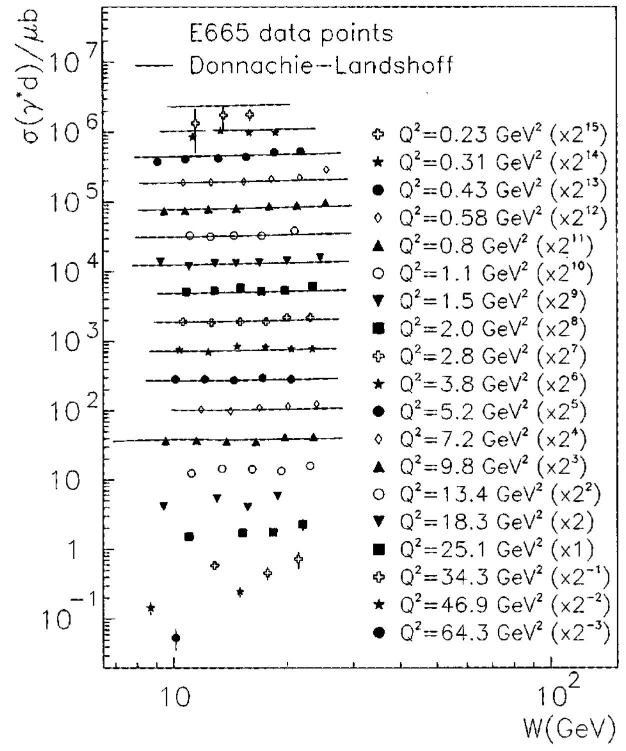

FIG. 59. W dependence of the virtual photoabsorption cross section for deuterons in Q^2 bins, compared with the Donnachie-Landshoff model.

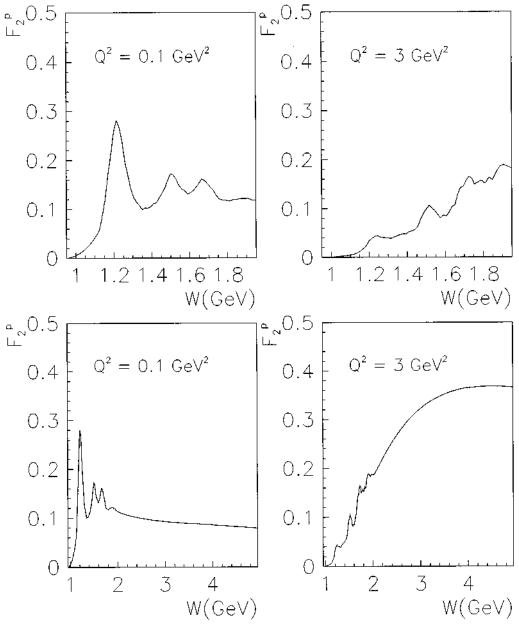

FIG. 60. F_2^p in the low W region for various Q^2.

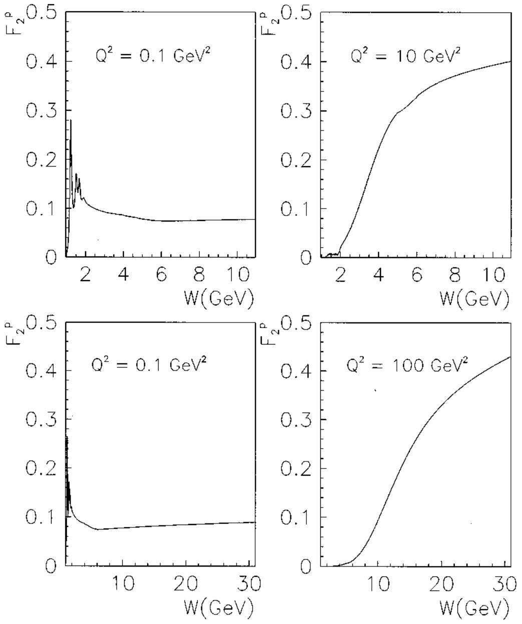

FIG. 61. F_2^p in the high W region for various Q^2.

B. Resonance region

The resonance region is usually identified with the range $M_{\text{nucleon}} < W < 2$ GeV. At low Q^2 the cross section in the resonance region is about a third of the elastic cross section. At higher Q^2 it is a larger fraction since the elastic form factor is more strongly suppressed as a function of Q^2.

A parametrization of the cross section in the resonance region can be obtained from Brasse *et al.* [38]. These authors used all the existing data available in their fit.

Electroproduction data from SLAC and DESY and photoproduction data from Daresbury are included, spanning the range $0 \leqslant Q^2 \leqslant 50$ GeV^2. The quantity parametrized is the virtual photon absorption cross section $\Sigma = \sigma_t + \epsilon\sigma_l$, where ϵ is the degree of polarization of the virtual photons, and σ_t and σ_l are the absorption cross sections for transversely and longitudinally polarized virtual photons, respectively. The flux of virtual photons is chosen using the ''Hand convention'' [73].

The data are fitted in various ranges of ϵ. At E665 the beam energy is very high, and so one expects the resonance excitation to occur for $\epsilon \sim 1$. Hence we take the fit for $\epsilon \geqslant 0.9$ so that the sensitivity to $R \equiv \sigma_l/\sigma_t$ is reduced. We then convert the cross section Σ to F_2 using the average value of ϵ for the data and the parametrization[2] of R from SLAC(1990) from [43]. For $W < 1.12$ GeV, we force F_2 to 0 as a quadratic function of W^2, as $W \rightarrow M$. In the following, we will refer to this parametrization as F2RESO. We suppress the deuteron F_2 in the resonance region by a factor of 0.88 with respect to the proton F_2 (i.e., $F_2^d = 0.88F_2^p$) to approximate the resonance data shown in Franz *et al.* [40]. The functional form of F2RESO can be found in Eq. (3) of [38], and the parameter values can be found in Sec. 3.1 and Table 1 of [38]. In Fig. 60 we show F_2^p computed using this parametrization for two values of Q^2. With increasing Q^2, we see greater suppression of the lower W resonances. At very low Q^2 there is little dependence on Q^2, apart from the fact that F_2^p vanishes linearly with Q^2 at fixed W.

C. Low *W* inelastic region

This is identified with the interval $2 < W < 5$ GeV. A parametrization of F_2 in this region is provided in Brasse *et al.* [39] [Eqs. (3), (7), and (11) and Table 1]. These authors use a compilation of then available world data spanning the resonance and deep inelastic region including photoproduction. They show that $\omega_W = (2M\nu + M_W^2)/(Q^2 + a^2)$ is a good variable to describe the data (where M_W^2 and a^2 are parameters). We will refer to this parametrization as F2LONU. This parametrization is provided for both proton and neutron. We take the deuteron structure function to be the average of the proton and neutron structure functions [i.e., $F_2^d = (F_2^p + F_2^n)/2$].

Both F2RESO and F2LONU have been used by a DESY experiment [40] performed by Franz *et al.* Good agreement is observed between the data from this experiment and the predictions based on the parametrizations. There is some ambiguity due to the choice of R, and so we use the F2LONU as used by [40] [Eqs. (B.3) and (B.4) and Table 3 using $R = 0.18$]. We now attempt to combine F2RESO with F2LONU. F2RESO is used for $W < 1.95$ GeV and F2LONU is used for $W > 1.95$ GeV. For low Q^2, the two functions connect with each other quite smoothly. For $Q^2 > 1$ GeV^2 there is a small discontinuity between them. For our purposes this is not a serious discrepancy, however such discontinuities are troublesome for computer programs that do numerical integrations. We therefore use a Fermi-Dirac function in W to connect these two parametrizations smoothly, using $W = 1.95$ GeV for threshold and 30 MeV for

---

[2] An average over three fits is used, one of which can be found in [43]. The other two are obtained by private communication with L. W. Whitlow.

width. The resulting function is referred to as F2LOWW. Thus, F2LOWW is defined by

$$\mathrm{F2LOWW}=\mathrm{F2RESO}\times f_{\mathrm{FD}}(W,1.95,0.03)+\mathrm{F2LONU}\times[1-f_{\mathrm{FD}}(W,1.95,0.03)], \quad (\mathrm{A1})$$

where W is in GeV and f_{FD} is the Fermi-Dirac function defined by

$$f_{\mathrm{FD}}(x,\mu,\beta)=(1+e^{(x-\mu)/\beta})^{-1} \quad (\mathrm{A2})$$

μ being the threshold in x and β being the width.

D. High *W* inelastic region

We use two parametrizations to describe the high W region. For high Q^2, we use the parametrization provided by the NMC that describes their data (Table 1 of [12]). Since this fit is not constrained by their data for $Q^2<0.7$ GeV^2, we do not trust the parametrization (referred to as F2NMC) in this region. Instead, we use a model by Donnachie and Landshoff [Eq. (4) of [28]], which is based on the ideas that total cross sections may be parametrized as a sum of two Regge powers of s, and that the same powers appear as powers of x_{Bj}^{-1} in the small x_{Bj} behavior of F_2 [see Eq. (10.1)]. The authors fit this form to photoproduction data over a wide energy range and to the NMC data from [12] for $Q^2<10$ GeV^2. This fit, which we call F2DOLA, can then be used for low Q^2. We merge these two parametrizations using the same technique mentioned previously, using Q^2 as the variable and setting the threshold at $Q^2=3$ GeV^2 with a width of 200 MeV. The NMC parametrization is available for both the proton and the deuteron. We use the Donnachie-Landshoff form as it is for the proton, and multiply it by 0.97 to use for the deuteron. This factor is derived from the E665 measurement [66] of the deuteron-to-proton cross-section ratio at low x_{Bj} and Q^2.

We shall call the resulting function F2HIW, which is given by

$$\mathrm{F2HIW}=\mathrm{F2DOLA}\times f_{\mathrm{FD}}(Q^2,3.0,0.2)+\mathrm{F2NMC}\times[1-f_{\mathrm{FD}}(Q^2,3.0,0.2)], \quad (\mathrm{A3})$$

where Q^2 is in GeV^2.

We now attempt to combine F2LOWW and F2HIW. F2HIW is evaluated for $W>5$ GeV, and F2LOWW is evaluated for $W<5$ GeV. At low Q^2 the two functions connect with each other smoothly. This is expected since the photoproduction data are included in both fits. At high Q^2 there is a 5–10 % discrepancy between the two functions at $W=5$ GeV. This is not a serious discrepancy since the functions are being evaluated at the kinematic edges of the respective data sets. At $W=5$ GeV, the data used in the low W fits are limited due to beam energy restrictions, especially at high Q^2. In this range of W the NMC data are limited due to detector resolution.

We attempt to simulate the curve that would be obtained if all the data used so far were fitted simultaneously. We do this by merging F2LOWW and F2HIW with our usual technique, setting the threshold at $W=5$ GeV and the width at 400 MeV. The resulting function is given by

$$F_2^{\mathrm{global}}=\mathrm{F2LOWW}\times f_{\mathrm{FD}}(W,5.0,0.4)+\mathrm{F2HIW}\times[1-f_{\mathrm{FD}}(W,5.0,0.4)], \quad (\mathrm{A4})$$

where W is in GeV. This function is capable of giving a reasonable value for F_2 over the entire Q^2-W space relevant to E665. This is shown in Figs. 60 and 61.

E. Conclusion

Using various parametrizations of data that are available in the literature, we have constructed a reasonable parametrization of F_2 that can be used at E665 as a starting point [74].

---

[1] R. Hofstadter and L. I. Schiff, in *Nucleon Structure*, Proceedings of the International Conference at Stanford, edited by R. Hofstadter and L. I. Schiff (Stanford University Press, Stanford, 1964).

[2] G. Miller *et al.* Phys. Rev. D **5**, 528 (1972).

[3] J. D. Bjorken, Phys. Rev. **179**, 1547 (1969); J. D. Bjorken and E. A. Paschos, *ibid.* **185**, 1976 (1969).

[4] R. P. Feynman, *Photon-Hadron Interactions* (Benjamin, Reading, MA 1972).

[5] J. Kuti and V. F. Weisskopf, Phys. Rev. D **4**, 3418 (1971).

[6] M. Gell-Mann, Phys. Lett. **8**, 214 (1964).

[7] G. Zweig, CERN Report No. 8182/Th401 (unpublished).

[8] Fermilab E26 Collaboration, C. Chang *et al.*, Phys. Rev. Lett. **35**, 901 (1975); Y. Watanabe *et al.*, Phys. Rev. Lett. **35**, 898 (1975).

[9] CHIO Collaboration, B. A. Gordon *et al.*, Phys. Rev. D **20**, 2645 (1979).

[10] EMC, J. J. Aubert *et al.*, Nucl. Phys. **B293**, 740 (1987).

[11] BCDMS Collaboration, A. C. Benvenuti *et al.*, Phys. Lett. B **237**, 592 (1990).

[12] NMC, P. Amaudruz *et al.*, Phys. Lett. B **295**, 159 (1992).

[13] E665 Collaboration, M. R. Adams *et al.*, Nucl. Instrum. Methods A **291**, 533 (1990).

[14] ZEUS Collaboration, M. Derrick *et al.*, Phys. Lett. B **316**, 412 (1993).

[15] H1 Collaboration, I. Abt *et al.*, Nucl. Phys. **B407**, 515 (1993).

[16] J. P. Berge *et al.*, Z. Phys. C **49**, 187 (1991).

[17] G. T. Jones *et al.*, Z. Phys. C **62**, 575 (1994).

[18] M. W. Shaevitz *et al.*, Nucl. Phys. B (Proc. Suppl.) **38**, 183 (1995).

[19] R. D. Kennedy, Ph.D. thesis, University of California, San Diego, 1992.

[20] Rurngsheng Guo, Ph.D. thesis, University of Illinois at Chicago, 1994.

[21] T. J. Carroll, Ph.D. thesis, University of Illinois at Chicago, 1994.

[22] Eric Ramberg, Ph.D. thesis, University of Maryland, College Park, 1989.

[23] Douglas G. Michael, Ph.D. thesis, Harvard University, Cambridge, MA, 1990.

[24] Michael H. Schmitt, Ph.D. thesis, Harvard University, Cambridge, MA, 1991.

[25] NMC, Ch. Scholz, computer program FERRAD version 35.

[26] Ashutosh V. Kotwal, ‘‘Time Dependence of Beam Parameters in Run 91,’’ E665 Report No. AN208, 1994 (unpublished).

[27] R. Brun *et. al.*, ‘‘GEANT: Simulation Program for Particle Physics Experiments, User Guide and Reference Manual,’’ CERN Computing Division Report No. CERN-DD/78/2, 1978 (unpublished).

[28] A. Donnachie and P. V. Landshoff, Z. Phys. C **61**, 139 (1994). The FORTRAN code to calculate the proton and neutron structure functions was kindly provided by Professor A. Donnachie.

[29] M. Gari and W. Kruempelmann, Z. Phys. A **322**, 689 (1985).

[30] M. P. Locher and A. Svarc, Fizika **22**, 549 (1990).

[31] J. Bernabeu, Nucl. Phys. **B49**, 186 (1972).

[32] J. Drees, ‘‘Radiative Corrections and Hadron Distributions in Deep-Inelastic μp Scattering,’’ Report No. EMC/78/24 (unpublished); Wuppertal University Report No. WU-B78-16, 1978 (unpublished); A. Arvidson and B. Badełek, ‘‘The Gamrad program,’’ NMC Internal Report No. NMC/92/5, 1992 (unpublished).

[33] L. W. Mo, Y. S. Tsai, , Rev. Mod. Phys. **41**, 205 (1969).

[34] Yung-Su Tsai, ‘‘Radiative Corrections to Electron Scattering,’’ Report No. SLAC-PUB-848, 1971 (unpublished).

[35] T. Sjöstrand, Comput. Phys. Commun. **39**, 347 (1986).

[36] M. Gluck, E. Reya, and A. Vogt, Z. Phys. C **5**, 127 (1992).

[37] Stephen Wolbers, ‘‘The E665 Second Stage Monte Carlo,’’ E665 Report No. MC010, 1991 (unpublished).

[38] F. W. Brasse *et al.*, Nucl. Phys. **B110**, 413 (1976).

[39] F. W. Brasse *et al.*, Nucl. Phys. **B39**, 421 (1972).

[40] J. Franz *et al.*, Z. Phys. C **10**, 105 (1981).

[41] D. F. Geesaman, ‘‘FERRAD, GAMRAD, AND TERAD — Dueling Radiative Corrections – II,’’ E665 Report No. AN143, 1992 (unpublished); ‘‘Dueling Radiative Corrections IV, Calculations with the same Structure Functions — Detailed Differences,’’ E665 Report No. AN159, 1992 (unpublished).

[42] B. Badełek *et al.*, ‘‘Radiative Correction Schemes in Deep Inelastic Muon Scattering,’’ Report No. TSL-ISV-94-0092, 1994 (unpublished).

[43] L. W. Whitlow *et al.*, Phys. Lett. B **250**, 193 (1990).

[44] Ashutosh V. Kotwal, ‘‘Data-Monte Carlo Comparisons of Uncorrelated Chamber Efficiencies for Run91,’’ E665 Report No. AN217, 1994 (unpublished).

[45] Ashutosh V. Kotwal, ‘‘Data-Monte Carlo Comparisons of Chamber Group Efficiencies for Run91,’’ E665 Report No. AN218, 1994 (unpublished).

[46] Ashutosh V. Kotwal, ‘‘Data-Monte Carlo Comparisons of Uncorrelated Chamber Efficiencies for Run91 in the Beam Region,’’ E665 Report No. AN222, 1994 (unpublished).

[47] Ashutosh V. Kotwal, ‘‘Update on Data-Monte Carlo Comparisons of Uncorrelated Chamber Efficiencies for Run91 in the Beam Region,’’ E665 Report No. AN223, 1994 (unpublished).

[48] Ashutosh V. Kotwal, Ph.D. thesis, Harvard University, Cambridge, MA, 1995.

[49] E665 Collaboration, M. R. Adams *et al.*, Z. Phys. C **61**, 179 (1994); Stephen C. O’Day, Ph.D. thesis, University of Maryland, College Park, 1990; N. Schmitz, Int. J. Mod. Phys. A **3**, 1997 (1988).

[50] R. D. Field and R. P. Feynman, Nucl. Phys. **B136**, 1 (1978); R. P. Feynman, Phys. Rev. Lett. **23**, 1415 (1969).

[51] Mark Adams and Timothy J. Carroll, ‘‘SAT Trigger Processor Users Guide,’’ E665 Report No. SW192, 1992 (unpublished).

[52] Ashutosh V. Kotwal, ‘‘The spill local rate monitor for RUN91,’’ E665 Report No. AN183, 1993 (unpublished).

[53] P. Spentzouris, Ph.D. thesis, Northwestern University, Evanston, 1994.

[54] P. Spentzouris and H. Schellman, ‘‘E665 Proton Calibration Run Part II,’’ E665 Report No. AN153, 1992 (unpublished); H. Schellman, ‘‘The E665 Proton Calibration Run, Part I,’’ E665 Report No. AN152, 1991 (unpublished).

[55] Particle Data Group, L. Montanet *et al.*, Phys. Rev. D **50**, 1173 (1994).

[56] J. Mar *et al.*, Phys. Rev. Lett. **21**, 482-4 (1968); L. S. Rochester *et al.*, *ibid.* **36**, 1284 (1976); **37**, 233E (1976).

[57] R. G. Roberts, *The Structure of the Proton* (Cambridge University Press, Cambridge, England, 1990).

[58] J. Schwinger, Phys. Rev. **76**, 790 (1949); D. R. Yennie, S. Frautschi, and H. Suura, Ann. Phys. (N.Y.) **13**, 379 (1961).

[59] R. P. Mount, Nucl. Instrum. Methods **187**, 401 (1981).

[60] Ashutosh V. Kotwal, ‘‘A Study of Trigger Timing for Run 91,’’ E665 Report No. AN210, 1994 (unpublished).

[61] Ashutosh V. Kotwal, ‘‘A Study of the Sensitivity of Various Latching Efficiencies to Trigger Timing,’’ E665 Report No. AN211, 1994 (unpublished).

[62] Paul Horowitz and Winfield Hill, *The Art of Electronics* (Cambridge University Press, Cambridge, England, 1980) (pseudo-random bit sequences and noise generation, Sec. 9, p. 437).

[63] E665 Report No. AN205, 1994 (unpublished).

[64] Richard G. Milner, in ‘‘Nucleon Form Factors,’’ proceedings of the Fifth Conference on the Intersections of Particle and Nuclear Physics, St. Petersburg, FL, 1994, MIT-LNS Report No. 94/71 (unpublished).

[65] A. D. Martin, R. G. Roberts, and W. J. Stirling, Phys. Rev. D **51**, 4756 (1995). The FORTRAN code to calculate F_2 and R was kindly provided by Professor W. J. Stirling.

[66] E665 Collaboration, M. R. Adams *et al.*, Phys. Rev. Lett. **75**, 1466 (1995).

[67] NMC, M. Arneodo *et al.*, ‘‘ Measurement of the Proton and Deuteron Structure Functions F_2^p and F_2^d,’’ Report No. CERN-PPE-95-138, 1995 (unpublished).

[68] ZEUS Collaboration, W. H. Smith; in the Albuquerque Meeting, Proceedings of the Meeting of the Division of Particles and Fields of the APS, Albuquerque, New Mexico, 1994, edited by S. Seidel (World Scientific, Singapore, 1994); M. Derrick *et al.*, Z. Phys. C **69**, 607 (1996).

[69] H1 Collabration, T. Ahmed *et al.* Nucl. Phys. **B439**, 471 (1995); H1 Collaboration, S. Aid *et al.*, ‘‘A Measurement and QCD Analysis of the Proton Structure Function $F_2(x,Q^2)$ at HERA,’’ Report No. DESY-96-039, (unpublished).

[70] M. Gluck, E. Reya, and A. Vogt, Z. Phys. C **67**, 433 (1995).

[71] B. Badełek and J. Kwieciński, Phys. Lett. B **295**, 263 (1992). The FORTRAN code to calculate the structure functions kindly provided by Professor B. Badełek.

[72] B. Badełek and J. Kwiecinśki, Phys. Rev. D **50**, 4 (1994). The FORTRAN code to calculate the shadowing in the deuteron was kindly provided by Professor B. Badełek.

[73] ‘‘1963 Summer Study Report — part II,’’ L. Hand and R. Wilson, Report No. SLAC-0025, 1963 (unpublished), Pt. 2A-B.

[74] The FORTRAN code for this parametrization may be obtained by writing to H. Schellman, Physics Department, Northwestern University, Evanston, IL 60208 (schellman@fnal.gov).